

ABSTRACT

Title of dissertation: PHYSICS OF LAMINAR PREMIXED $CH_4 - O_2$
FLAMES AT CRYOGENIC CONDITIONS -
A COMPUTATIONAL STUDY

Abishek Gopal
Doctor of Philosophy, 2019

Dissertation directed by: Professor Johan Larsson
Department of Mechanical Engineering

With increased commercial spaceflight activity, methane has found adoption in the next generation of liquid rocket engines (LREs). In a liquid rocket engine with cryogenic propellants, such as methane and oxygen, the propellants are stored in their tanks at low temperatures. As they are injected into the combustion chamber at high pressures, the fluid is close to its thermodynamic critical point where there are drastic changes in fluid properties like density, heat capacity, surface tension, and solubility. The ideal gas law is inapplicable at such extreme conditions, and real gas thermodynamic and transport properties are required to accurately model the combustion physics at supercritical conditions. Much of the previous work applying real gas models in computational simulations of reacting flows have focused on non-premixed flames or cold-flow mixing configurations. In this study, we investigate the effects of real gas property estimation on planar, unstretched, laminar premixed methane-oxygen flames at transcritical conditions.

The computational framework used in this study integrates real gas property

estimation into the steady-state, freely-propagating flame solver available in the Cantera combustion suite. The Peng-Robinson equation of state provides thermodynamic property closure. High-pressure transport properties are modeled by the Chung and Takahashi correlations, respectively. The effects on laminar flame structure are presented. We find that enhanced real gas reactant densities have a significant impact on flame propagation, lowering flame speeds by a factor of ~ 5 near the critical region. Real gas caloric properties lower mass burning rates by 10%. The consequence of using low-pressure transport properties with the Peng-Robinson EOS at variable Lewis numbers is discussed.

PHYSICS OF LAMINAR PREMIXED $CH_4 - O_2$ FLAMES AT
CRYOGENIC CONDITIONS - A COMPUTATIONAL STUDY

by

Abishek Gopal

Dissertation submitted to the Faculty of the Graduate School of the
University of Maryland, College Park in partial fulfillment
of the requirements for the degree of
Doctor of Philosophy
2019

Advisory Committee:

Professor Johan Larsson, Chair/Advisor

Professor Elaine S. Oran

Professor Kenneth Kiger

Professor Christopher Cadou

Professor Arnaud Trouvé

To Heather Heyer
1985–2017

Acknowledgments

I am indebted to all the people who made it possible for me to finish my dissertation.

Firstly, I would like to acknowledge the role of my academic adviser, Dr. Johan Larsson, in giving me the opportunity to pursue a career in scientific computing. Dr. Larsson's emphasis on scientific rigor and critical thinking has been crucial in the development of skills necessary for a career in science. In addition, my analytical writing skills have improved immeasurably as a result of Dr. Larsson's feedback. I am also grateful to my research collaborators for their valuable feedback during the analysis phase. Thank you, Pedro, for proofreading my dissertation.

I would like to thank my research group colleagues, old and new, for livening up the arduous experience of graduate school. Thank you Siavash, Walter, Pedro, John, Ali, Jon, and Nikhil for your support. I appreciated the camaraderie that developed with the influx of the newer members, and I will miss it. I am thankful that I got to sample some of Nikhil's stellar culinary skills, which inspired me to get better at preparing Indian cuisines.

Survival during the ongoing Anthropocene extinction event is no mean feat, let alone complete graduate school. I owe deep gratitude to my closest friends who have provided emotional and material support during all this. Thank you Milica, Nithin, Lena, Jeremy, Moon-Soo, Stephanie. Special thanks to my dear friends, Milica and Lena, for letting me vent my frustration about the rise of neo-fascism

worldwide.

I want to acknowledge the role of Alexandra Elbakyan's Sci-Hub in making science much more accessible to everyone. Hopefully, this will usher in an era of not-for-profit scientific publishing. I want to thank the wonderful staff at University of Maryland's Graduate Writing Center. I also want to thank the administrators of the supercomputing clusters I frequent: University of Maryland's Deepthought2 and Johns Hopkins' MARCC clusters.

Finally, I would like to thank my mom, dad and sister for their support and patience throughout this long journey.

Table of Contents

List of Tables	v
List of Figures	vi
List of Abbreviations	x
1 Introduction	1
1.1 Critical phenomena	2
1.2 Rocket propulsion systems	5
1.3 Motivation for studying premixed flames	8
1.3.1 Ignition in liquid rocket-engines	8
1.4 Previous work	10
1.5 Objectives	13
1.6 Computational considerations	13
2 Physical model	15
2.1 Conservation equations	15
2.2 Thermodynamic equation of state - for ρ, p, T	19
2.2.1 The ideal gas model	21
2.2.2 Brief history of real models	22
2.2.3 Soave-Redlich-Kwong equation of state	26
2.2.4 Peng-Robinson equation of state	28
2.2.5 Computational considerations	29
2.2.6 Properties of unstable species	30
2.3 Caloric equation of state - for e, c_p, h	31
2.3.1 The thermally perfect assumption for an ideal gas	32
2.3.2 Real gas: departure functions	33
2.3.3 Mixing and combination rules	35
2.4 Transport properties	39
2.4.1 Low-pressure transport coefficients	40
2.4.1.1 Coefficient of viscosity	40
2.4.1.2 Mass diffusion model and diffusion coefficients	42
2.4.1.3 Coefficient of thermal conductivity	44
2.4.2 High-pressure transport models	46
2.4.2.1 Chung correlation: for μ and λ	47

2.4.2.2	Takahashi correlation: for D_{AB}	52
2.5	Chemical kinetics model	55
2.5.1	Detailed chemical kinetics	57
2.5.2	Verification of kinetics - Ignition delay test	60
3	Theory of laminar premixed flames and previous studies	62
3.1	Structure of a canonical premixed flame	62
3.2	Simplified analysis	64
3.2.1	Thermal theory of flame propagation	64
3.2.2	Theory of Zeldovich, Frank-Kamenetskii, and Semenov	66
3.3	Previous numerical studies of premixed flames using real gas EOS	68
3.3.1	Hydrogen flames	68
3.3.2	Methane flames	71
4	Cantera-RealGas: steady-state solver	75
4.1	Shortcomings of the transient reacting flow solver	75
4.2	Solver architecture	77
4.3	Governing equations	78
4.4	Numerical method	79
4.4.1	Damped Newton method	79
4.4.2	Pseudo time-stepping	81
4.5	Spatial discretization	82
4.6	Boundary and initial conditions	83
4.7	Computational grids	84
4.7.1	Adaptive refinement	84
4.8	Data input and pre-processing	86
4.9	Validation of premixed flames at low pressures	87
4.10	Verification of grid convergence	89
4.11	Validation of premixed flames at elevated pressures	91
4.11.1	Validation with experiment	91
4.11.2	Validation with computations	93
5	Real gas effects in high-pressure laminar $CH_4 - O_2$ premixed flames	96
5.1	Effect of Real gas thermodynamic models	96
5.1.1	Structure of a transcritical flame at $Le = 1$	96
5.1.2	Energy production and transport	98
5.1.3	Effect on mass burning rate and flame thickness	100
5.1.4	Effect on laminar flame speeds	102
5.1.5	Effect on flame temperatures	103
5.1.6	Effect of thermodynamic departure functions	104
5.1.7	Equivalence ratio ϕ effects	106
5.1.8	Differential diffusion effects ($Le_k \neq 1$)	107
5.2	Effect of Real gas transport models	112
5.2.1	Flame structure	112
5.2.2	Flame speed trends	114

5.3	Effect of high-pressure chemical mechanisms	114
6	Conclusions and future directions	117
6.1	Publications and presentations	118
6.2	Future directions	119
	Appendices	121
A	UnsteadyFlame: transient solver	122
A.1	Governing equations	122
A.2	Finite volume formulation	123
A.3	Computational grids	124
A.4	Time advancement	126
A.5	Boundary conditions	127
	A.5.1 Characteristic non-reflecting boundary conditions	127
	A.5.2 Boundary controllers	129
B	Real-gas thermodynamics – partial molar properties	132
C	Assessment of Chung correlation for transport property estimation	136

List of Tables

1.1	Operating conditions of common rocket engines	6
1.2	Critical points of select bi-propellants	7
1.3	List of previous computational studies of laminar premixed flames	12
2.1	Computational costs to estimate density of several fluids	30
2.2	Verification of mixing rules (partial molar volume) for a mixture of $CH_4 - C_2H_6 - C_3H - 8$	38
2.3	Verification of mixing rules (density) for a mixture of $CH_4 - C_2H_6 -$ $C_3H - 8$	38
A.1	Grid stretching parameters	125
C.1	Low- and high-temperature intervals for evaluated species	137
C.2	AADs in viscosities computed in the low- and high-temperature inter- vals with respect to reference properties from Coolprop [1].	138
C.3	AADs in thermal conductivities computed in the low- and high- temperature intervals with respect to reference properties from Cool- prop [1].	138

List of Figures

1.1	$p - T$ chart for O_2	3
1.2	Generalized compressibility chart	4
1.3	Compressibility factors of common liquid rocket engines	7
1.4	Sketch of the four ignition phases in a $LOX - GH_2$ rocket	9
2.1	Plot of the Lennard-Jones potential well.	20
2.2	Validation of density for pure- CH_4	26
2.3	Validation of compressibility factor for CO_2 and density for O_2	29
2.4	Validation of specific heat capacity and speed of sound	34
2.5	Densities of a mixture containing 0.095039 moles of CH_4 , 0.03961 moles of C_2H_6 , and 0.01000 of C_3H_8 at $T = 300, 350, 400$ Kelvins using the present implementation (Solid lines), reference numerical data [39] (Dashed) and experimental data [9] (Symbols).	39
2.6	Illustration of mass diffusion process	42
2.7	H_2O viscosity and thermal conductivity using different approaches	48
2.8	O_2 viscosity and thermal conductivity using different approaches	52
2.9	CH_4 viscosity and thermal conductivity using different approaches	53
2.10	High-pressure binary mass diffusivity of $CO_2 - C_2H_4$ mixtures	55
2.11	Hierarchy of chemical kinetics models	56
2.12	Ignition delays of a $CH_4 - O_2 - N_2$ mixture	60
3.1	Structure of a laminar premixed flame	63
3.2	Flame speeds and thicknesses of premixed $H_2 - air$ flames at $T_u = 298K$	69
3.3	Relative importance of individual Real gas modifications in El-Gamal et al. [10]	70
3.4	Effects of EOS and thermal diffusivity on a laminar premixed $H_2 - air$ flame at for $T_u = 100K$ and $p = 100bar$ (Giovangigli et al. [11])	71
3.5	Effects of high-pressure transport properties on a laminar premixed $H_2 - air$ flame at for $T_u = 100K$ and $p = 100bar$ (Giovangigli et al. [11])	72
3.6	Validation of $CH_4 - O_2 - He$ flame speeds with experiment ([38])	73

3.7	Computed laminar flame speeds S_L and flame temperatures T_b for premixed $CH_4 - O_2$ flames at 67 bar (Ribert et al. [53])	74
4.1	Illustration of the hybrid approach to computing laminar premixed flames. Figure by Goodwin [13].	77
4.2	Schematic of Cantera integration.	78
4.3	Sample stretched grid with ratio=2.0, slope=0.01, curve=0.01, prune=-0.1.	86
4.4	Laminar flame speeds for $H_2 - O_2 - Ar$ mixtures at a range of a) Fresh-gas temperatures b) Ambient pressures and c) Equivalence ratios using Ideal gas (Blue Crosses), Peng-Robinson (Red solid line), and CHEMKIN Ideal gas reference (Triangles). Computations default to $p = 1 \text{ bar}$, $T_u = 300K$ and $\phi = 1.0$, unless otherwise specified.	88
4.5	Computed laminar flame speeds with uniform grids (—●—) and stretched grid (▲), non-linear least squares fit of Eqn. 4.18 (⋯⋯), and the estimated true flame speed (---) for a premixed $CH_4 - O_2$ flame at 75 bar, $T_u = 170K$, $Le_k = 1$ using Peng-Robinson EOS.	90
4.6	Estimated error norms for temperature T , and CO mass fraction with uniform grids (—●—) and stretched grid (▲) for a premixed $CH_4 - O_2$ flame at 75 bar, $T_u = 170K$, $Le_k = 1$ using Peng-Robinson EOS. Dashed line (---) represents first-order convergence.	91
4.7	Experimentally observed (▲ - Rozenchan et al. [54]) and computed (—- Present Study, --- [38]) laminar flame speeds for $CH_4 - O_2 - He$ mixtures at a) (17% $O_2 - 83\%He$) at 40 atm and b) (15% $O_2 - 85\%He$) at 60 atm for a range of equivalence ratios.	92
4.8	Laminar flame speeds of stoichiometric premixed $CH_4 - O_2$ mixtures using the Ideal gas law with the present work (—), Ribert [53] (---) and Chemkin reference [26](⋯⋯) at unity-Lewis number (Blue) and variable-Lewis numbers (Red). Fresh-gas temperature is 300K, and the mechanism used is due to Lindstedt [32].	93
4.9	Comparison of a) laminar flame speeds b) flame temperatures of stoichiometric premixed $CH_4 - O_2$ mixtures at 67 bar using the Ideal gas (Blue) and Real gas (Red) equations of state with the present work (IG,PR —, SRK ---), Ribert [53] (---). Assumes low-pressure transport and $Le_k = 1$. Mechanism from Lindstedt [32].	95
5.1	Profiles of mixture density ρ , temperature T , species mass fractions Y_k , specific heat capacity c_p , and thermal diffusivity α_{th} for a transcritical premixed $CH_4 - O_2$ flame at 75 bar, $T_u = 170K$, $Le_k = 1$ with Peng-Robinson (—) and Ideal gas (---) EOS.	97
5.2	Fluxes of heat release rates through convection \dot{Q}_{conv} , the conduction \dot{Q}_{cond} , species mass diffusion \dot{Q}_{diff} , and chemical reaction \dot{Q}_{src} for a transcritical premixed $CH_4 - O_2$ flame at 75 bar, $T_u = 170K$, $Le_k = 1$ with Peng-Robinson (—) and ideal gas (---) EOS.	99

5.3	Variation of a) laminar mass burning rates and b) reaction zone thickness for stoichiometric premixed $CH_4 - O_2$ flames at a range of temperatures and pressures using Peng-Robinson EOS (—) and Ideal gas law (- - -). Assumes low-pressure transport and $Le_k = 1$	100
5.4	Variation of a) laminar flame speeds and b) flame temperatures for stoichiometric premixed $CH_4 - O_2$ flames at a range of temperatures and pressures using Peng-Robinson EOS (—) and Ideal gas law (- - -, \circ). Assumes low-pressure transport and $Le_k = 1$. Mechanism from Lindstedt [32].	102
5.5	Scaling of a) laminar flame speeds with reactant density and b) flame temperatures with reactant enthalpy for stoichiometric premixed $CH_4 - O_2$ flames at a range of temperatures and pressures using Peng-Robinson EOS (—) and Ideal gas law (- - -). Assumes low-pressure transport and $Le_k = 1$. Mechanism from Lindstedt [32].	104
5.6	a) Laminar flame speeds and b) mass burning rates for stoichiometric premixed $CH_4 - O_2$ flames using Peng-Robinson EOS for ρ and departure functions (—), Peng-Robinson EOS only for ρ without departure functions (- - -) and Ideal gas (\circ) . Assumes low-pressure transport and $Le_k = 1$	105
5.7	Variation of laminar flame speeds with equivalence ratio ϕ for stoichiometric premixed $CH_4 - O_2$ flames at fresh-gas temperatures of a) 175 K and b) 300 K. Both computations use Peng-Robinson EOS with $Le_k = 1$ and low-pressure transport.	108
5.8	Variation of laminar mass burning rates with equivalence ratio ϕ for stoichiometric premixed $CH_4 - O_2$ flames at fresh-gas temperatures of a) 175 K and b) 300 K. Both computations use Peng-Robinson EOS with $Le_k = 1$ and low-pressure transport.	108
5.9	Densities and heat capacities of pure methane and oxygen and several intermediate mixture compositions at 175 K	109
5.10	Profiles of mixture density ρ , temperature T , species mass fractions Y_k , thermal diffusivity α , and species mass diffusivity D_k for a transcritical premixed $CH_4 - O_2$ flame at 75 bar, $T_u = 170K$, with $Le_k \neq 1$ Peng-Robinson (—) and $Le_k = 1$ (- - -). Low-pressure transport assumed.	110
5.11	Profiles of species partial molar volumes V_k and mixture density ρ for a transcritical premixed $CH_4 - O_2$ flame at 75 bar, $T_u = 170K$, with $Le_k \neq 1$ (—) and $Le_k = 1$ (- - -). Peng-Robinson EOS is used with low-pressure transport is used.	111
5.12	Profiles of mixture density ρ , temperature T , species mass fractions Y_k , thermal diffusivity α , and species mass diffusivity D_k for a transcritical premixed $CH_4 - O_2$ flame at 75 bar, $T_u = 170K$, with $Le_k \neq 1$ Peng-Robinson (—) and $Le_k \neq 1$, $Le_{H_2O} = 1$ (- - -). Low-pressure transport assumed	112

5.13	Profiles of mixture density ρ , temperature T , species mass fractions Y_k , thermal diffusivity α , and species Lewis number Le_k for a transcritical premixed $CH_4 - O_2$ flame at 75 bar, $T_u = 170K$, with high-pressure transport (—) and low-pressure transport (- - -). The Peng-Robinson EOS is used with differential diffusion effects.	113
5.14	a) Laminar flame speeds and b) Mass burning rates of stoichiometric premixed $CH_4 - O_2$ mixtures with high-pressure transport (—), low-pressure transport (- - -) and ideal gas (⋯⋯⋯).	114
5.15	Profiles of mixture density ρ , temperature T , mass fractions Y_k of major and minor species, and chemical heat release rates \dot{Q}_{src} for a transcritical premixed $CH_4 - O_2$ flame at 75 bar, $T_u = 170K$, using the mechanisms from Lindstedt [32] (—), Huang et al. [21] (⋯⋯⋯) and [48] (- - -). Assumes Peng-Robinson EOS with high-pressure transport and $Le_k \neq 1$	115
5.16	a)laminar flame speeds and b)mass burning rates for stoichiometric premixed $CH_4 - O_2$ flames at 75 bar using the kinetic mechanisms from Lindstedt [32] (—), Huang et al. [21] (⋯⋯⋯) and [48] (- - -). Assumes Peng-Robinson EOS with high-pressure transport and $Le_k \neq 1$	116
A.1	Sample stretched grid with $N = 1024$, $\beta_{fine} = 0.4$, $N_{fine} = 0.8$ and $X_{fine} = 0.45$	126
C.1	Pure-fluid a) viscosities and b) thermal conductivities of Water using the low-pressure correlation (- - -), the original (⋯⋯⋯) and modified (—) Chung correlation and the reference values (⋯⋯⋯).	138
C.2	Pure-fluid a) viscosities and b) thermal conductivities of Methane using the low-pressure correlation (- - -), the original (⋯⋯⋯) and modified (—) Chung correlation and the reference values (⋯⋯⋯).	139
C.3	Pure-fluid a) viscosities and b) thermal conductivities of Oxygen using the low-pressure correlation (- - -), the original (⋯⋯⋯) and modified (—) Chung correlation and the reference values (⋯⋯⋯).	139
C.4	Pure-fluid a) viscosities and b) thermal conductivities of CO_2 using the low-pressure correlation (- - -), the original (⋯⋯⋯) and modified (—) Chung correlation and the reference values (⋯⋯⋯).	140
C.5	Pure-fluid a) viscosities and b) thermal conductivities of Hydrogen using the low-pressure correlation (- - -), the original (⋯⋯⋯) and modified (—) Chung correlation and the reference values (⋯⋯⋯).	140
C.6	Pure-fluid a) viscosities and b) thermal conductivities of n-Dodecane using the low-pressure correlation (- - -), the original (⋯⋯⋯) and modified (—) Chung correlation and the reference values (⋯⋯⋯).	141

List of Abbreviations

AAD	Absolute Averaged Deviation
BWR	Benedict, Webb, and Rubin
CFL	Courant-Friedrichs-Lewy (condition)
CSP	Corresponding States Principle
EOS	Equation of State
HEOS	Helmholtz-energy Equation of State
IG	Ideal Gas
ILDm	Intrinsic Low Dimension Manifold
LES	Large-Eddy Simulations
LODI	Local One-Dimensional Inviscid equations
LRE	Liquid Rocket Engines
mBWR	modified Benedict, Webb, and Rubin
NASA	National Aeronautics and Space Administration
ODE	Ordinary Differential Equation
PDE	Partial Differential Equation
PR	Peng-Robinson
RG	Real Gas
RK	Redlich-Kwong
RK4	Fourth-order Runge-Kutta
ROP	Rate of Progress
SRK	Soave-Redlich-Kwong
vdW	van der Waals
vdW1f	van der Waals one-fluid theory

Chapter 1: Introduction

Combustion research is crucial in addressing the ever-increasing energy requirements across the world. Past research in combustion has typically centered on developing a detailed understanding of the physics underlying combustion, advancing the safety and efficiency of propulsion and energy-generation processes, and efforts to reduce the emissions of harmful by-products of combustion. With the rapid increase in the capabilities of high-performance computing architectures, computational simulations are widely used to investigate many problems in combustion. Applying a numerical simulation framework to analyze combustion in propulsion devices like liquid rocket engines offer many advantages like drastically reducing the number of prototypes that need to be tested. Numerical simulations also offer ways to isolate flow physics from combustion chemistry, which can be used to solve potential problems that arise during the development phase. Liquid rocket engines are especially susceptible to dangerously high pressure levels which arise as a result of combustion instabilities. Simulations can be very helpful in improving our understanding of combustion instabilities.

One of the biggest challenges in computational simulations of reacting flows is the wide range of length and time scales present in the physical process. Resolving the entire range of time and length scales present in three-dimensional turbulent flames is not feasible, even with the most powerful computing platforms. Canonical

one-dimensional reacting flow simulations offer a powerful tool to understand the combustion chemistry and transport processes occurring in more physically realistic simulations. Computations of simple one-dimensional flames can be used to construct models representative of the small length and time scales involved in combustion. Such models can then be used as closure terms in more realistic large-eddy simulations (LES).

Numerical simulations of reacting flows often make use of simple thermodynamic models, like the ideal gas model, which are sufficiently accurate in the vicinity of low pressures and high temperatures. However, some combustion devices operate at conditions close to the thermodynamic critical point, and computational simulations for such regimes require higher-accuracy thermodynamic models.

1.1 Critical phenomena

The critical point of a substance is the thermodynamic state (for example: a specific temperature and pressure) beyond which the vapor-liquid phase separation ceases to exist, and the fluid is characterized by a single dense phase where the fluid properties change continuously. Substances existing at a state above their critical point are said to be supercritical fluids.

Figure 1.1 plots the pressure-temperature ($p - T$) chart for pure oxygen. The critical point (p_c, T_c) is the upper extreme of the vapor-liquid equilibrium curve. Below the critical point (and above the triple point), gases that condense to a liquid do so with an abrupt change in temperature and pressure. Beyond the critical point, there is a smooth and continuous change in the primary thermodynamic state variables like temperature, pressure and density. As the fluid state moves from gas phase to supercritical, there are sudden and abrupt changes in the other fluid

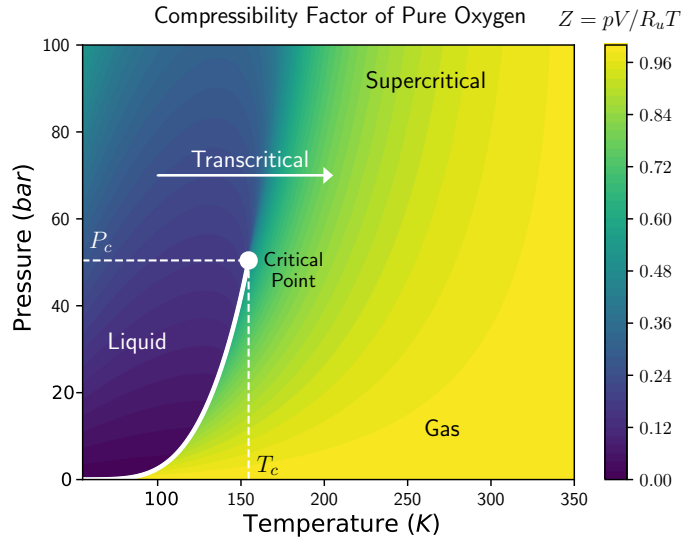


Figure 1.1: Pressure-temperature ($p - T$) chart for O_2 , displaying the contours of compressibility factor Z , and vapor-liquid equilibrium curve. Data from [1].

properties. The heat capacity at constant pressure approaches infinity, the latent heat of vaporization and the surface tension also disappears. The supercritical fluid exhibits enhanced solubility and mixing properties as well.

Classically, the thermodynamic closure for the governing equations in fluid mechanics is specified by the ideal gas law. The ideal gas model is applicable only to gas molecules, and assumes that the gas molecules behave like point particles undergoing random elastic collisions. Furthermore, it also assumes that the density of the gas is low enough to neglect any intermolecular forces of attraction or repulsion between the molecules. Given these limitations, the ideal gas law is insufficient for liquids and supercritical fluids. Gases at high pressures also exhibit non-ideal behavior. To quantify the deviation from ideal gas behavior, the compressibility factor Z is defined as

$$Z = \frac{pV}{R_u T}, \quad (1.1)$$

where p is the pressure in Pascals (Pa), T is the temperature in Kelvins (K), V is the molar volume (m^3/mol), and R_u is the universal gas constant ($Jmol^{-1}K^{-1}$). By

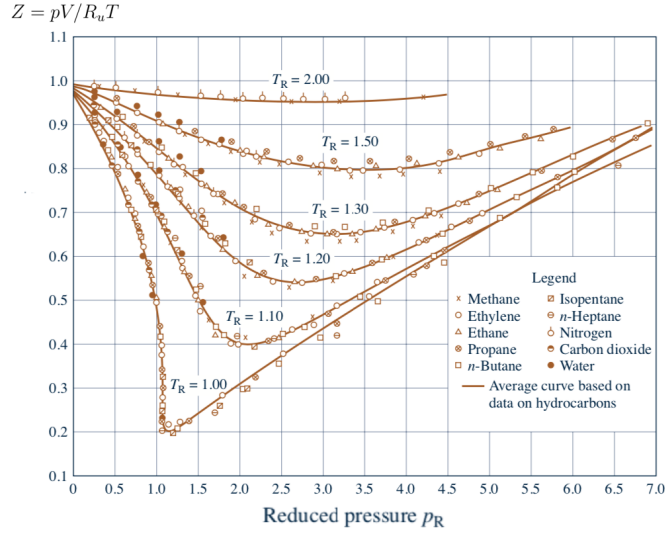


Figure 1.2: Generalized compressibility chart. Figure from [44], with data from [67].

definition, the compressibility factor Z is unity for an ideal gas. Any deviation from unity quantifies the non-ideal behavior.

If the compressibility factor Z is plotted against the substance's reduced state, which is the thermodynamic state normalized with respect to its critical point, then a universal behavior for Z is observed. Figure 1.2 plots the observed values of the compressibility factor Z for several fluids against their reduced pressure ($p_r = p/p_c$), for different values of the reduced temperature ($T_r = T/T_c$). We see that the respective isotherms collapse on top of each other, regardless of the fluid in question. van der Waals was the first to realize this universal scaling law for thermodynamic properties. This is known as the principle of corresponding states, and forms the basis of many thermodynamic and transport property estimation correlations.

From the compressibility chart in Figure 1.2, it is evident that Z is approximately unity at low pressures, and the ideal gas model is sufficient. At low pressures, the attractive and repulsive forces between the colliding molecules are minimal and any addition or removal of energy affects only the kinetic-energy budget of

the gas molecules. At moderate to high pressures, the attractive forces between the molecules reduce the effective pressure of the system. At such conditions, the volume occupied by the molecules can no longer be neglected. The point particle assumption must be removed, leading to a reduction of the effective volume. As a result, the compressibility factor drops to less than unity ($Z < 1$). At extremely high pressures, however, the molecules experience strong repulsive forces and the reduction in the effective pressure is counteracted by an increase in the effective volume. In such cases, Z returns to unity and eventually $Z > 1$.

Supercritical phenomena are present in many naturally-occurring fluid dynamic regimes. The lower atmosphere of Venus is composed of a mixture of predominantly $CO_2 - N_2$, with average pressures and temperatures of 92 *bar* and 735 *K* on the surface [3]. Given such extreme surface temperatures and pressures, it is expected that CO_2 exists in its supercritical phase at certain sections in the Venus atmosphere, and has a significant influence on the structure and rotation of the atmosphere.

Supercritical phenomena occur in many engineering applications as well. In the pursuit of higher efficiency, the propulsion systems of aircrafts and rocket launch vehicles have progressed towards operating conditions characterized by higher pressures. At such conditions, the reactants can exist in their supercritical states.

1.2 Rocket propulsion systems

Liquid rocket engines (LRE) remain the primary mode of propulsion in space launch vehicle configurations. LREs offer larger specific impulse (ratio of total thrust to weight of propellant) compared to solid rocket motors [68]. The higher

Class	$p_{chamber}$	Fuel/Ox	T_{inj}^{Ox} (K)	T_{inj}^{Fuel} (K)	$\sim Z_{reac}$
Vulcain	115 bar	$LH_2 - LOx$	95 K	34 K	0.71
Merlin 2	100 bar	RP-1 - LOx	55 K	302 K	0.53
Raptor	300 bar	$CH_4 - LOx$	90 K	90 K	1.17

Table 1.1: Operating conditions of common rocket engines. Data from [61].

attainable exhaust velocity in LREs is preferred for space launch applications. Solid rocket motors find application as a set of boosters for a primary liquid rocket engine. In a typical hybrid rocket configuration, the main LREs are supplemented by solid booster rockets during the initial part of the ascent, when a larger amount thrust is needed to escape the Earth’s gravitational influence. In the final stages of ascent, fine tuning of thrust becomes necessary to achieve target orbits with precision. In addition, rocket motors must have the ability to be restarted at will to correct orbits or move to different orbits. LREs can also be throttled, turned off, or restarted arbitrarily, unlike solid rocket motors, where they have to be specifically pre-programmed to do so [68].

Liquid propellants can be classified into mono-propellants, like hydrazine, and bi-propellants, which involves a fuel and oxidizer combination. Unlike hydrazine or heavier hydrocarbon fuels like RP-1 (refined Kerosene), that are liquids at room temperatures, cryogenic propellants such as O_2 , H_2 and CH_4 require liquification, under low temperatures and high pressures, to keep the propellant tank sizes small.

In a liquid rocket engine with cryogenic bi-propellants, fuel and oxidizer are stored as cryogenic liquids in their respective tanks. During ignition, the propellant valves are opened and the fuel and oxidizer are injected into the combustion chamber at low temperatures and high pressures. Table 1.1 lists the typical injection conditions in some common rocket engines. Table 1.2 lists the critical points of commonly used bi-propellants. At injection, the thermodynamic state of the pro-

Species	Critical Temperature T_c	Critical Pressure P_c
H_2	33.18 K	13.0 bar
CH_4	190.6 K	46.1 bar
RP-1	658.2 K	18.3 bar
O_2	154.6 K	50.4 bar

Table 1.2: Critical points of select bi-propellants. RP-1 is approximated by n-dodecane ($C_{12}H_{26}$). Data from Linstrom and Mallard [33].

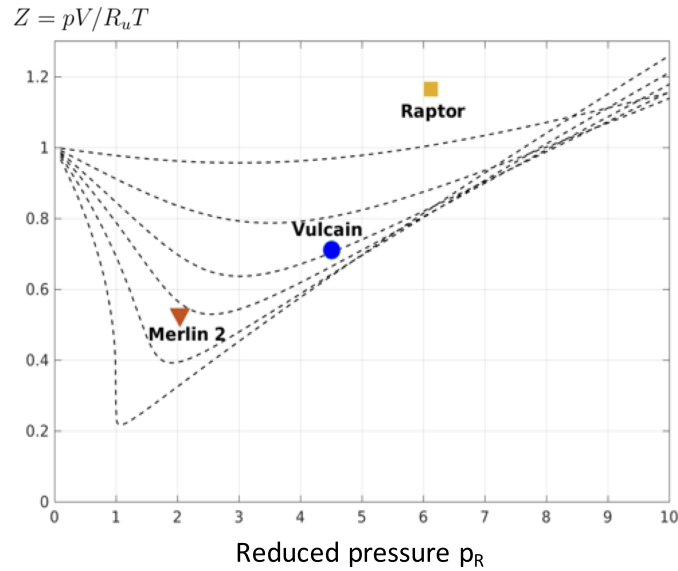


Figure 1.3: Generalized compressibility chart showing the operating points of liquid rocket engines (symbols). The dashed black lines represent isotherms of compressibility factor Z .

propellants is close to their respective critical points, and the ideal gas assumptions are no longer valid at such high pressures. Figure 1.3 shows the generalized compressibility chart along with estimated compressibility factor for several rocket configurations, assuming the respective propellants at injection conditions and present in stoichiometric proportions. The large deviations of Z from unity indicate that real gas effects can be important at the conditions typical of cryogenic liquid propellants. To accurately model the physical processes occurring in liquid rocket engines, it is necessary to replace the ideal gas model with high-fidelity thermodynamic and transport models.

1.3 Motivation for studying premixed flames

In non-premixed combustion, the fuel and oxidizer are injected via separate streams, and the burning rate is determined by how fast the reactants mix with each other. In premixed combustion, fuel and oxidizer are mixed at a molecular level before being ignited, and hence the burning rate is controlled by a balance between the chemical reaction rates and the diffusion timescale. In a liquid rocket engine, the predominant mode of burning at steady-state is non-premixed combustion, and most studies into transcritical combustion in rocket engines focus on this configuration [7, 39, 46]. However, as we will discuss shortly, the ignition phase exhibits considerable regions of premixed flames. The premixed flame dynamics during the ignition phase can sometimes lead to explosive pressure levels, potentially damaging the combustion chamber. Hence the premixed regime is important to study.

Apart from potential relevance to the ignition processes in liquid rocket engines, we intend for this study to be a fundamental investigation into the physics of premixed combustion at supercritical conditions. Furthermore, modern combustion devices increasingly favor higher-pressure regimes and premixed burning for reasons of combustion efficiency.

1.3.1 Ignition in liquid rocket-engines

Laser-ignition tests of liquid oxygen - gaseous hydrogen ($LOX - GH_2$) flames in LRE-like configurations performed using the M3 micro-combustor at DLR Lampoldshausen [57, 16, 47] show that the ignition process is composed of several phases, as illustrated in Figure 1.4. The primary ignition phase begins with the firing of the laser pulse and the formation of the flame kernel, followed by the

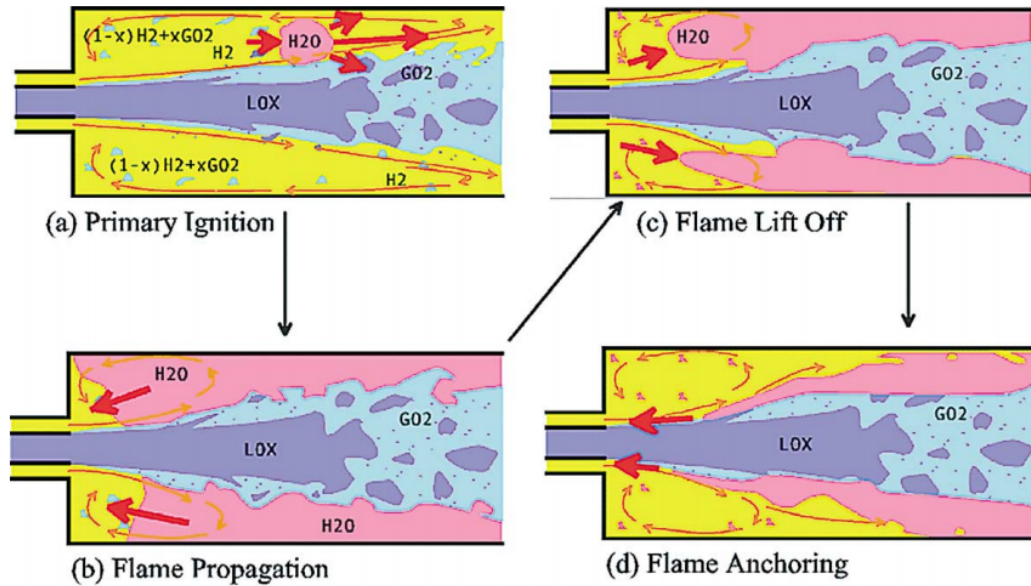


Figure 1.4: Sketch of the four phases during the ignition in a $LOX - GH_2$ rocket. Figure from Gurliat et al. [16]

flame kernel propagating downstream due to convection by the shear layer, and ends when the flame kernel reaches the edge of the shear layer. In this phase, the flame speed is largely determined by the degree of premixedness of the shear layer. In the second phase, termed the flame propagation phase, the flame expands into the recirculation zone consuming all the propellants that have already been premixed. The end of this phase is characterized by a rapid rise in the chamber pressure. The pressure rise could be smooth or strong, depending on the availability of premixed propellants. When the premixed propellants in the recirculation zone have been consumed, the flame moves downstream until the convection velocity and the flame speeds are balanced. This is termed the flame lift-off phase. In the final phase, the flame anchoring phase, the flame slowly moves upstream until steady-state conditions have been attained.

The important parameter determining the nature of the ignition is the duration of time elapsed between the opening of the propellant valves and the firing of the igniter [47]. This determines how much time the fuel and oxidizer have

to mix. If the mixing time is too short, the reactants are insufficiently mixed and the flame consumption/ propagation speed is smaller than the convective speed in the chamber. As a result, the ignited flame kernel is blown downstream and extinguishes [28]. In the standard ignition scenario, a 'smooth ignition', the mixing time is just sufficient for the flame front to anchor itself close to the injectors. For excessive mixing times, the flame speed is considerable compared to the convective speeds. This leads to a 'strong ignition' characterized by a rapid upstream expansion of the flame kernel and rapid consumption of the propellants. This causes a sudden rise of the chamber pressure and the nozzle getting choked, causing a backflow of hot gases into the injector dome [47] and damage to the combustor. The sharp rise in pressure during the ignition is an important factor determining the safety of the rocket motor. Understanding the dynamics of premixed flames at engine-relevant conditions can help with the prediction of such hazardous conditions.

1.4 Previous work

Most of the efforts in the modeling of supercritical effects in rocket engines have gone towards studying non-premixed flames and cold-flow mixing processes. Since the focus of the present study is in premixed flames, we offer only a brief introduction into the studies in high-pressure mixing processes and non-premixed flames. For a comprehensive survey on this topic, the reader is referred to works by Candel et al. [7] and Masquelet [39].

The key difference in cold flow studies of transcritical coaxial injection from the subcritical case is the absence of liquid-gas interface due to non-existent surface tension and a zero latent heat of vaporization. It is characterized by an absence of droplet formation and a smooth dissolution into the ambient fluid. There have been a number of studies on the mixing characteristics in non-reacting coaxial jets, with

operating conditions resembling those found in liquid rocket engines. The injection into the ambient fluid occurs at supercritical pressures. The main effort has been towards relating the potential core length with a characteristic non-dimensional parameter like the momentum flux ratio between the outer stream and the inner stream. Further details can be found in [7].

Oefelein and Yang [46] were among the first to model the real gas effects in the mixing and combustion mechanisms occurring in rocket engines. They investigated high-pressure spray dynamics at ambient pressures of up to 400 atm. Hickey and Ihme [20] also developed a numerical framework to study high-pressure mixing and combustion processes typical of rocket propulsion. The study computed flamelets from high-pressure $H_2 - O_2$ mechanisms and used them to study the real gas effects in a high-pressure reacting $GO_2 - GH_2$ single-injector configuration.

In contrast to the number of studies on high-pressure mixing and non-premixed reacting flows, the effects of critical phenomena on laminar premixed flames have been studied much less widely. To our knowledge, there have been only five studies on this topic.

El-Gamal et al. [10] were the first to investigate the structure of laminar premixed $H_2 - air$ flames at high pressures (up to 100 MPa). This study used high-pressure models for thermodynamics, transport, and chemical kinetics. This study found that real gas effects start to become significant at ambient pressures exceeding 10 bar. The study also found that the major contribution to the real gas effects was from the equation of state. High-pressure transport properties were found to be the second biggest contributing factors, while the effect of non-ideal chemical kinetics was found to be considerably less. Giovangigli et al. [11] studied the structure of transcritical laminar premixed $H_2 - air$ flames in much more detail. This study reaffirmed the finding from [10] that the real gas equation of state was

Study	Reactants	Operating Conditions	Focus of Study
El-Gamal et al. [10] (2000)	$H_2 - air$	$p = 10 - 1000 \text{ bar}$, $T_u = 298 K$	Fundamental
Marchionni et al. [38] (2007)	$CH_4 - air$	$p = 1 - 150 \text{ atm}$, $T_u = 298 K$	Fundamental
Giovangigli et al. [11] (2011)	$H_2 - air$	$p = 100 - 1000 \text{ atm}$, $T_u = 100 K$	Fundamental
Ribert et al. [53] (2017)	$CH_4 - O_2$, $CH_4 - air$	$p = 67 \text{ bar}$, $T_u = 140 - 300 K$	Flamelet computation
Güven and Ribert [17] (2018)	$H_2 - O_2$	$p = 100 \text{ bar}$, $T_u = 150 K$	Flamelet computation

Table 1.3: Survey of previous computational studies of laminar premixed flames that model real gas thermodynamics.

the biggest contributing factor, followed by high-pressure transport properties. The study used non-ideal chemical production rates to ensure non-negative entropy production, and found the non-ideal kinetics to be significant only at extremely high pressures (1000 *bar*). Marchionni et al. [38] studied real gas effects in $CH_4 - O_2$ premixed flames at pressures of up to 150 *atm*. While this study explored real gas effects on flames with varying equivalence ratios and pressures up to 140 *atm*, it did not explore the low-temperature cryogenic conditions typical of rocket combustion. The study used an ambient temperature of 298 *K*, where the effects of critical phenomena are expected to be less important. Ribert et al. [53] computed flamelets for a laminar premixed $CH_4 - O_2$ flame using real gas property estimation. The study explored the parameter space in more detail compared to [38]. Güven and Ribert [17] assessed the effect of non-ideal binary mass diffusion coefficients on $H_2 - air$ flamelets at transcritical conditions. In Chapter 3, we will discuss the findings from the reference studies for transcritical laminar premixed flames in greater detail.

1.5 Objectives

1. Develop real gas combustion framework

The primary goal of this work is to develop predictive numerical capability for transcritical laminar premixed flames. To this end, we start out with the development and verification of a compressible, reacting-flow solver in 1D. The solver was initially developed with low-pressure thermodynamic and transport models, and has been extended to incorporate real gas property estimation.

2. Study transcritical laminar $CH_4 - O_2$ premixed flames

After sufficiently verifying and validating the reacting flow solver, and the implementation of real gas property estimation, we analyze the effects of high-pressure thermodynamic and transport phenomena on the structure and propagation of laminar premixed $CH_4 - O_2$ flames at rocket-like conditions. We also intend to study the constituent effects of real gas thermodynamic models separately.

1.6 Computational considerations and the development of multiple solvers

To study laminar premixed flames using computational methods, we have two options. The simplest option is to take the set of compressible Navier-Stokes expression and time-advance until the flame has reached steady state. While the most popular option is to assume that flame front is stationary at steady-state, and solve the boundary value problem described by the steady-state, compressible, low-Mach formulation of the Navier-Stokes equations using the Newton root-finding method. Due to the wide range of time scales involved, combustion is a stiff

problem and solving a steady-state problem is far cheaper than a transient solver. Typical software packages for simulating laminar premixed flames, namely Chemkin [26] and Cantera [14] use the steady-state approach. The primary drawback of this method is that the imposed initial condition must lie within the domain of convergence of the steady-state solver. This is expected to be an issue in achieving a solution for flames with real gas effects.

Hence, we started this study by building a transient compressible solver, where the convergence process is less dependent on the choice of initial conditions. This is detailed in Appendix A. However, due to the need for higher computational efficiency, we also implemented real gas property estimation into the steady-state solver available in Cantera. This integrated solver has been widely used in generating most of the results presented in this dissertation and is described in Chapter 4.

Chapter 2: Physical model

This chapter will describe the governing equations and the associated thermodynamic and transport properties required for numerical simulations of reacting flows at transcritical conditions.

2.1 Conservation equations

The physics of compressible reacting flows in one-dimension are governed by the compressible Navier-Stokes equations along the axial direction (x -direction), with the addition of a conservation equation for every species present in the reacting mixture. The terms in the equations are written in the conservative form, except for the chemical source term in the species conservation relations. The form of the equations used here is elaborated in Poinso and Veynante [49]. The conservation of mass along the axial direction can firstly be expressed in an aggregate form as

$$\frac{\partial \rho}{\partial t} + \frac{\partial(\rho u)}{\partial x} = 0, \quad (2.1)$$

and secondly, accounting for individual species product and transport in the reactive mixture, we can write

$$\frac{\partial(\rho Y_k)}{\partial t} + \frac{\partial(\rho u Y_k)}{\partial x} = -\frac{\partial j_k}{\partial x} + \dot{\omega}_k. \quad (2.2)$$

The conservation of momentum takes the familiar form

$$\frac{\partial(\rho u)}{\partial t} + \frac{\partial(\rho u^2)}{\partial x} = \frac{\partial(\sigma_{xx}^S)}{\partial x} = -\frac{\partial p}{\partial x} + \frac{\partial(\tau_{xx}^S)}{\partial x}. \quad (2.3)$$

Lastly, the conservation of total energy accounts for the balance of energy due to heat conduction, mass diffusion, viscous dissipation, and pressure work, written as

$$\frac{\partial(\rho e_t)}{\partial t} + \frac{\partial(\rho u e_t)}{\partial x} = -\frac{\partial q}{\partial x} + \frac{\partial}{\partial x} (\sigma_{xx}^S u). \quad (2.4)$$

The terms appearing in equations 2.1 through 2.4 will be described in the next few paragraphs.

The state variables ρ , u , Y_k and e_t represent the mixture density (kg/m^3), the axial velocity (m/s), the mass fraction of species k , and the total energy per unit mass (J/kg) respectively.

The mass diffusion of species k in Eqn. 2.2 is represented by the divergence of the species mass flux j_k . The species mass flux j_k is simply the product of species mass ρY_k and "diffusion velocity" \mathbb{V}_k

$$j_k = \rho \mathbb{V}_k Y_k. \quad (2.5)$$

With the assumption of mixture-averaged mass transport and negligible thermal diffusion (Soret) effects, the diffusion velocity can be approximated using the Hirschfelder-Curtiss form as

$$\mathbb{V}_k = -D_k \frac{\nabla X_k}{X_k} + \mathbb{V}_c, \quad (2.6)$$

where X_k and D_k are the mole fraction and mixture-averaged mass diffusivity for

species k . The species transport equation (Eqn. 2.2) may not necessarily sum up to the aggregate conservation of mass expression (Eqn. 2.1), necessitating a correction velocity term \mathbb{V}_c in the mass flux term to ensure that mass is conserved. Details about the form of correction velocity in use and transport coefficient estimation are described in Section 2.4.1.2 - Mass diffusion model and diffusion coefficients.

The final term in the species conservation equation (Eqn. 2.2) is the species production rate $\dot{\omega}_k$ ($kg/m^3 - s$). This study uses the detailed chemical kinetic mechanism to model the species production rate, which is detailed in Section 2.5 - Chemical kinetics model.

In the conservation of momentum expression, Eqn. 2.3, the diffusion of momentum is expressed by the divergence of the stress tensor along the axial direction σ_{xx}^S . For an isotropic, Newtonian fluid, the total stress tensor in three-dimensional space, σ_{ij}^S is expressed as the sum of the normal and shear stress components

$$\sigma_{ij}^S = \underbrace{\left(-p + \mu_v \frac{\partial u_k}{\partial x_k}\right)}_{\text{Normal Stress}} \delta_{ij} + \underbrace{\mu \left(\frac{\partial u_i}{\partial x_j} + \frac{\partial u_j}{\partial x_i}\right)}_{\text{Shear Stress}}, \quad (2.7)$$

where p is the thermodynamic pressure, δ_{xx} is the Kronecker delta function, μ is the dynamic viscosity ($N - s/m^2$), and μ_v is the so-called second coefficient of viscosity. In contrast to the thermodynamic pressure p , we can also define a "mechanical pressure" \bar{P} as the mean of the normal stress components

$$\begin{aligned} -\bar{P} &= \frac{1}{3}(\sigma_{xx} + \sigma_{yy} + \sigma_{zz}), \\ &= -p + \underbrace{\left(\mu_v + \frac{2}{3}\mu\right)}_{\kappa} \frac{\partial u_k}{\partial x_k}, \end{aligned} \quad (2.8)$$

where $\kappa = \left(\mu_v + \frac{2}{3}\mu\right)$ is the bulk viscosity of the mixture. The bulk viscosity is negligible for flows where the relaxation time for attaining local equilibrium is much

smaller than the characteristic time scales of the flow. This is true for monoatomic gases which do not have rotational and vibrational modes, and therefore have shorter relaxation times. In such cases, the mechanical and thermodynamic pressures are equivalent, and $\mu_v = -2/3$. This is known as the Stokes' assumption. In compressible reacting flows, however, we typically consider a variety of polyatomic gases, where this assumption does not strictly hold due to the presence of rotational and vibrational modes of energy. However, numerical studies of compressible mixing layers have found the even effects of large bulk viscosities on the flow field to be minimal [39].

Substituting the Stokes' assumption of $\mu_v = -2/3$ in Eqn. 2.7, the expression for the stress tensor along the axial direction is

$$\sigma_{xx} = -p + \frac{4}{3} \left(\mu \frac{\partial u}{\partial x} \right) \quad (2.9)$$

In the total energy balance equation (Eqn. 2.4), the divergence of the heat flux term q accounts for the heat transfer due to heat conduction and the changes to the chemical potential due to mass diffusion. Fourier's law relates the heat conduction flux to the gradient of temperature T as

$$q_c = -\lambda \frac{\partial T}{\partial x} \quad (2.10)$$

where λ represents the mixture-averaged thermal conductivity ($W/(m \cdot K)$). Considering the transport of chemical potential energy due to species mass diffusion, the total heat flux term becomes

$$q = -\lambda \frac{\partial T}{\partial x} + \rho \sum_k h_k Y_k \nabla_k. \quad (2.11)$$

In the above expression, h_k (J/K) is the partial enthalpy of species k in mass units. We neglect the transfer of heat due to radiation. In previous numerical studies of real gas flames (Juanós and Sirignano, 2017), the rate of radiative heat transfer was found to be two orders of magnitude less than the heat transfer rate due to conduction and the energy conversion rate [23].

Having described the details of the diffusion and source terms in the conservation equations 2.1 through 2.4, we still need to describe the thermodynamic relations to close the system of equations. In particular, we need:

- (1) A relation between the primary thermodynamic state variables - pressure, temperature, and density. This is known as the thermodynamic equation of state, and is further described in Section 2.2 - Thermodynamic equation of state - for ρ, p, T .
- (2) Expressions for caloric quantities, such as internal energy, enthalpy and heat capacities, as a function of the primary thermodynamic variables. This is sometimes referred to as the caloric equation of state. This is described in Section 2.3 - Caloric equation of state - for e, c_p, h .

2.2 Thermodynamic equation of state - for ρ, p, T

An equation of state (EOS) provides a semi-empirical relation between the thermodynamic state variables - pressure, temperature, and density. A generalized EOS of a multi-component mixture, explicit in pressure, is a function of temperature T , molar volume V , and mixture composition (mole fraction X_k)

$$p = f(T, V, X_k). \quad (2.12)$$

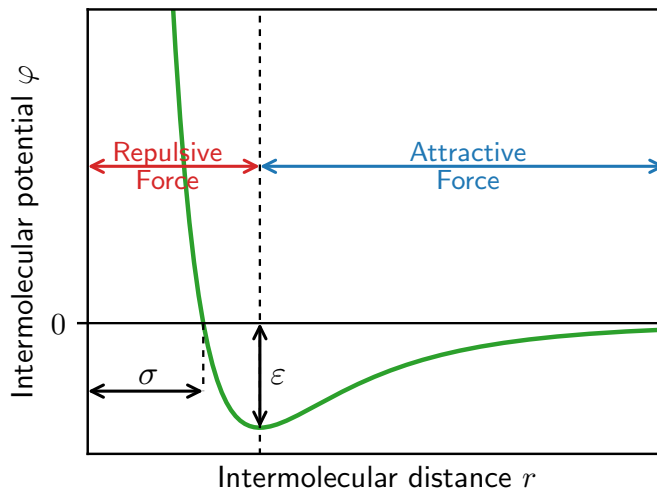


Figure 2.1: Plot of the Lennard-Jones potential well.

The fidelity of equations of state depends on how they model interactions between randomly colliding molecules and the volume occupied by molecules. Before we describe the development of equations of state, it can be helpful to develop a qualitative view of the intermolecular interactions by means of a model formulated by Lennard-Jones in 1924 [22]. Lennard-Jones expressed the intermolecular potential energy $\varphi(r)$ of a pair of non-polar, non-bonding molecules as a function of the distance of separation r between the molecules

$$\varphi(r) = 4\varepsilon \left[\left(\frac{\sigma}{r}\right)^{12} - \left(\frac{\sigma}{r}\right)^6 \right], \quad (2.13)$$

where σ represents the characteristic diameter of the molecules, called the collision diameter. The characteristic energy is represented by potential well-depth ε and it is defined as the maximum energy of attraction between a pair of molecules [2]. The variation of the L-J potential $\varphi(r)$ as a function of intermolecular distance r is illustrated in Figure 2.1. As the intermolecular potential is expressed as a function of distance, the intermolecular force F is simply the negative of the slope, $F(r) = -d\varphi/dr$. At an infinite distance of separation, the molecules do not interact

with each other. At a large, but finite r , the molecules experience attractive forces and approach each other until they reach an equilibrium distance, at which point the force of attraction ceases. In this state, the potential energy is minimum, signifying that this is the stable configuration. If the molecules are brought even closer together (with an expense of energy), they experience a repulsive force.

With this model of intermolecular interactions laid out, we introduce the thermodynamic equations of state applicable to pure fluids in Sections 2.2.1 through 2.2.4. To determine the aggregate thermodynamic properties of a multi-component mixture, a set of mixing rules would need to be applied to pure fluid properties. This is explained in Section 2.3.3 - Mixing and combination rules.

2.2.1 The ideal gas model

The simplest model for describing the thermodynamic properties of a fluid is the ideal gas (IG) law. In an ideal gas, molecules behave like point particles undergoing random elastic collisions, with no intermolecular attractions between the molecules. The pressure-explicit form of the ideal gas law is

$$pV = R_u T, \quad (2.14)$$

where R_u is the universal gas constant. These assumptions hold well for non-polar molecules at low pressures and moderate temperatures. The L-J fluid model described in the previous section is incompatible with the assumptions of an ideal gas. While the ideal gas law is a practical assumption for many combustion applications, it does not capture the drastic variation of thermodynamic quantities close to the critical point, which is characterized by low temperatures and extremely high pressures. At high pressures, the total volume occupied by the molecules is comparable to the total volume, and the point particle assumption is no longer valid.

Moreover, the intermolecular forces can no longer be ignored in such confined spaces.

2.2.2 Brief history of real models

In 1873, van der Waals developed the first major improvement over the ideal gas law. van der Waals took the effects of attractive forces and a finite molecular size into consideration with two fluid-specific parameters a and b . Intermolecular forces represented by a affect the effective pressure of the system. Similarly, the co-volume parameter b serves to reduce the total volume available for collisions. The van der Waals (vdW) equation of state takes the form

$$(p + a/V^2)(V - b) = R_u T. \quad (2.15)$$

The vdW EOS is a cubic equation with respect to the molar volume V , while actual pVT data has been observed to take a fourth-order form [71]. Nevertheless, a cubic equation can be solved directly using the Cardan's formula [45], avoiding the need for expensive iterative methods to solve for V . While the van der Waals EOS is not an accurate model for modern uses in fluid-phase equilibria, it spawned the development of hundreds of cubic equations of state with vastly improved prediction capabilities.

To obtain constitutive relations for parameters a and b , van der Waals applied the conditions of zero slope and inflexion point to the critical isotherm at the critical point

$$\left. \frac{\partial p}{\partial V} \right|_{T=T_c} = \left. \frac{\partial^2 p}{\partial V^2} \right|_{T=T_c} = 0, \quad (2.16)$$

which yielded

$$T_c = \frac{8a}{27R_u b}, \quad p_c = \frac{a}{27b^2}, \quad V_c = 3b. \quad (2.17)$$

The van der Waals parameters a and b can thus be expressed as a universal functions of the critical temperature T_c , critical pressure p_c , and critical volume V_c of a pure fluid

$$a = \frac{27 (R_u T_c)^2}{64 p_c}, \quad b = \frac{R_u T_c}{8 p_c}. \quad (2.18)$$

This implies that the pVT behavior for a wide variety of fluids follow a universal scaling law, if the thermodynamic state of each fluid is scaled with respect to its critical properties. This universality is realized in the compressibility factor Z , defined as

$$Z = \frac{pV}{R_u T}. \quad (2.19)$$

Figure 1.2 shows the plots of compressibility factor Z vs the reduced pressure P_r for different values of the reduced temperature T_r . It is remarkable that the compressibility factor Z of a wide range of substances collapse on to the same set of curves. This universality allows for the estimation of fluid phase equilibrium properties with just the data from a reference fluid. This is known as the *Corresponding States Principle* (CSP), and is regarded as the "most useful byproduct of van der Waals' equation of state" [15].

The realization of universality resulted in the creation of a new category of equations of state based on the CSP. Pitzer (1939) developed an EOS based on the CSP as a function of the two intermolecular potential parameters. The two-parameter CSP formulations were found to hold well for noble gases (Ar , Xe), but had varying levels of success for more complex fluids. Pitzer, in 1955, included a third parameter to account for the effect of molecular structure and orientation on intermolecular potential [30]. Pitzer parameterized the difference in the reduced vapor pressure of normal fluids from the noble gases, at $p_r = 0.1$

and $T_r = 0.7$, as the acentric factor ω

$$\omega = -\log_{10}(p_r)|_{T_r=0.7} - 1.$$

The acentric factor has since found importance in improving the accuracy of cubic equations of state, as well.

Apart from equations of state based on van der Waals EOS and the corresponding state principle, models based on series expansions found popularity. Kamerlingh Onnes (1901) developed the virial equation of state, which expresses the pressure as a power series in terms of density

$$\frac{p(T, \rho)}{\rho R_u T} = Z(T, \rho) = 1 + B(T)\rho + C(T)\rho^2 + D(T)\rho^3 + \dots,$$

where coefficients B, C and D are the second, third and fourth virial coefficients respectively, and are functions of temperature alone. While originally intended for empirical correlations, the virial coefficients were later linked to theoretical understanding of statistical thermodynamics [70]. Parameters B, C and D signify the interactions between a pair of molecules, a triad of molecules, a tetrad of molecules and so on. Empirically-determined virial coefficients of many fluids are widely available. However, virial expansions do not typically work well near the liquid phase.

Among the class of virial-type equations with empirically-determined coefficients, the one proposed by Benedict, Webb, and Rubin (BWR) in 1940, remains important. The BWR equation involves eight parameters, and was subsequently extended to mixtures. Modified forms of the BWR equation of state (mBWR), with up to 32 fluid parameters, have been used as reference equations of state.

The biggest improvements to the multi-parameter reference equations of state in the last several decades came from advancements in optimization methods, improving predictions by a factor of three in many cases [64]. The other important development has been the introduction of equations based on the Helmholtz free energy. Equations of state explicit in pressure $p(T, \rho)$ or the compressibility factor $Z(T, \rho)$ are not considered "fundamental equations of state" as they do not provide information about caloric properties such as heat capacities and ethalpies [64]. However, an EOS explicit in the Helmholtz free energy $a(T, \rho)$ can provide complete information about the thermodynamic state of a substance, including the caloric properties. At the time of writing, Helmholtz energy equations of state are some of the most popular reference equations of state available.

The viability of such methods in computational simulations are limited due to computational complexity. In Section 2.2.5 - Computational considerations, we compare the performance of Helmholtz energy EOS with Peng-Robinson. In addition to computational complexity, it is also challenging to generalize the Helmholtz energy EOS across fluids. Since the Helmholtz energy EOS depends on empirical data, extending them to mixtures would be limited by the availability of experimental data on mixtures. For a multi-component mixture with a large of number of species, this would be a challenge.

In our study, we use the cubic equations of state due to their computational effectiveness. We use the high-accuracy Helmholtz energy equation of state in order to validate our property estimation with the cubic methods. Hence we use the open-source thermodynamic property estimation suite, Coolprop [1], for this purpose. Coolprop implements the Helmholtz energy EOS for many fluids of interest, thereby making the validation process much simpler.

The van der Waals EOS inspired the development of hundreds of cubic equa-

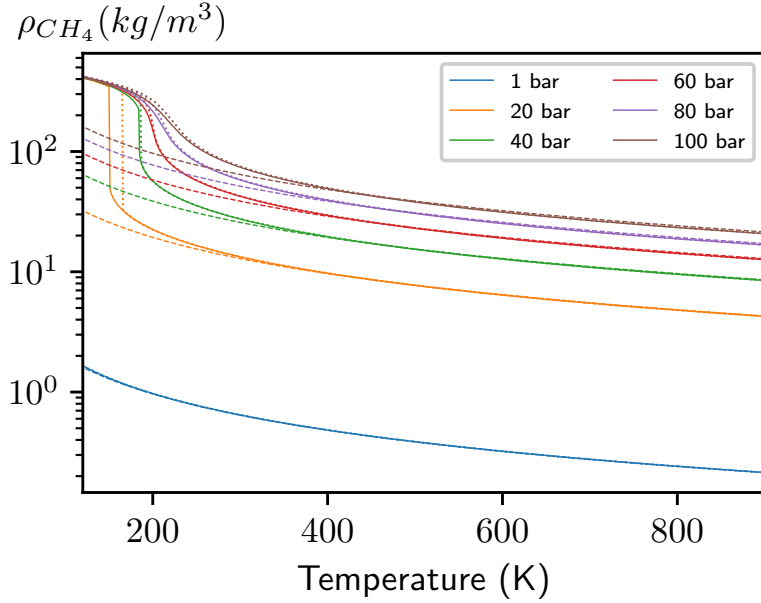


Figure 2.2: Pure-fluid density for CH_4 using Soave-Redlich-Kwong EOS (—), Ideal gas law (---) and Coolprop-HEOS (·····) at different pressures. Coolprop [1] uses the Helmholtz energy form for CH_4 from [59].

tions. The essential among them are the Redlich and Kwong, Soave modification to Redlich and Kwong, and Peng Robinson. Soave-Redlich-Kwong (SRK) and Peng-Robinson (PR) equations of state are the most widely used cubic EOS for computational simulations and optimization [71]. They will be explored further in the next few sections.

2.2.3 Soave-Redlich-Kwong equation of state

Redlich and Kwong (1949) drastically improved the accuracy of the van der Waals EOS for gaseous systems by adding a temperature dependency to the parameter a , with an alpha function.

$$\alpha(T) = \frac{1}{\sqrt{T_r}}. \quad (2.20)$$

While the Redlich-Kwong (RK) EOS provided good results for gases, it was not designed for liquid or supercritical phases. Wilson [75] first proposed including

the acentric factor in the α -function to account for effects of molecular shape and orientation, and tying it with the corresponding states principle. Soave (1972) [63] further modified the α -function based on Wilson's proposal, using the Redlich-Kwong equation of state. This took the form

$$\alpha(T_r, \omega) = (1 + f(\omega)[1 - \sqrt{T_r}])^2 \quad (2.21)$$

where

$$f(\omega) = 0.480 + 1.574\omega - 0.176\omega^2 \quad (2.22)$$

The pressure-explicit form of the Soave-Redlich-Kwong EOS is

$$p = \frac{R_u T}{V - b} - \frac{A' \alpha(T_r, \omega)}{V(V + b)}, \quad (2.23)$$

where the parameters A' and b are functions of the critical properties T_c, P_c

$$A' = 0.42747 \frac{R_u^2 T_c^2}{p_c} \quad b(T_c) = 0.08664 \frac{R_u T_c}{p_c} \quad (2.24)$$

Figure 2.2 compares the density of pure CH_4 obtained from the Soave-Redlich-Kwong EOS with predictions from the Helmholtz energy EOS implemented in Coolprop [1]. The predictions from the Soave-Redlich-Kwong equation are quantitatively very similar to HEOS in the gaseous and supercritical regions, despite slightly under predicting density near the critical point. However, the Soave-Redlich-Kwong EOS, or any cubic equation of state, is not capable of accurately predicting the vapor-liquid transition or the liquid-phase properties.

2.2.4 Peng-Robinson equation of state

The Peng-Robinson EOS was developed as an enhancement to the Soave-Redlich-Kwong EOS to improve the accuracy in the critical region. Peng and Robinson modified the volume dependency of the attractive term, and provided a modified version of the $\alpha(T_r, \omega)$ function. The pressure-explicit form of the Peng-Robinson EOS is

$$p = \frac{R_u T}{V - b} - \frac{A' \alpha(T_r, \omega)}{V^2 + 2bV - b^2}, \quad (2.25)$$

where the parameters A' and b are functions of the critical properties T_c, P_c

$$A' = 0.45724 \frac{R_u^2 T_c^2}{p_c}, \quad b(T_c) = 0.0778 \frac{R_u T_c}{p_c}, \quad (2.26)$$

and $\alpha(T_r, \omega)$ function is based on Soave's modification

$$\alpha(T_r, \omega) = (1 + f(\omega)[1 - \sqrt{T/T_c}])^2. \quad (2.27)$$

For Peng-Robinson, the expression for $f(\omega)$ is

$$f(\omega) = 0.37464 + 1.54226\omega - 0.26992\omega^2. \quad (2.28)$$

Peng-Robinson provides more accurate estimations of density for heavier hydrocarbons near the critical point. Despite the development of higher-accuracy equations of state and correlations, Peng-Robinson still remains a very popular choice for the equation of state [34]. The critical compressibility factor predicted by Peng-Robinson is around 0.301 and is closest to the observed critical compressibility factors around 0.27.

Figure 2.3a) compares the compressibility factor of CO_2 obtained from the

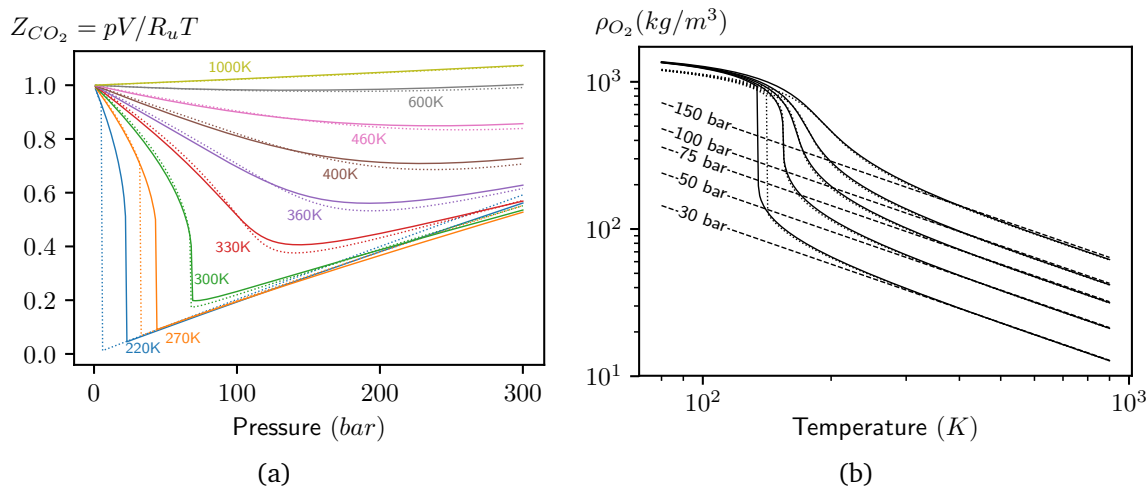


Figure 2.3: Pure-fluid a) compressibility factor for CO_2 b) density for O_2 using Peng-Robinson EOS (—), Ideal gas law (- - -) and Coolprop-HEOS (.....) at different pressures. Coolprop [1] uses the Helmholtz energy form for CO_2 from [65], and O_2 from [56] [66].

Peng-Robinson EOS with the Coolprop reference. Above the vapor-liquid equilibrium envelope, Peng-Robinson captures the qualitative effects near the critical point very well, and the quantitative agreement is also sufficient considering that we are using a generalized two-parameter cubic EOS. Figure 2.3b) compares the density of O_2 obtained from the Peng-Robinson EOS with the Coolprop reference. The Peng-Robinson density diverges from expected at extremely low temperatures, but this is still satisfactory for the cryogenic conditions considered in this study.

2.2.5 Computational considerations

The first consideration in choosing an appropriate EOS to model thermodynamics in a computational study is whether to use pre-computed thermodynamic tables or runtime thermodynamic computations. While pre-computed tables lets us use pVT data from reference equations like the Helmholtz EOS, they require that the thermodynamic tables be loaded in memory. Due to restrictions on program memory, this would only be feasible if the degrees of freedom, such as the number of species, thermodynamic quantities of interest, or the range of temperatures and

Species	CPU time - PREOS (μs)	CPU time - HEOS (μs)	PREOS Speedup
H_2	0.369942	20.2743	55
O_2	0.341154	37.1312	109
CH_4	0.333462	47.8969	144
CO_2	0.330636	93.5946	283

Table 2.1: Computational costs involved in estimating $\rho(T, p)$ for several fluids, using the Peng-Robinson and Helmholtz energy EOS (HEOS). We use the HEOS implemented in Coolprop [1].

pressures, are kept low. In the present study, however, none of these conditions hold true and pre-tabulated thermodynamics is not computationally viable.

Considering only runtime thermodynamic calculations, Cubic EOS are preferable in numerical simulations due to the fewer parameters in use and the on-the-fly computational performance. Table 2.1 shows the computational costs associated with the Peng-Robinson EOS implementation in the present work and HEOS implementation in Coolprop [1] for several pure-fluids. In this test, we measure the mean CPU time associated with each call to $\rho(T, p)$. The same compiler optimization was used in both cases. The speedup associated with using Peng-Robinson (or cubic EOS) varies from a factor of 55 for H_2 to around 283 for CO_2 .

2.2.6 Properties of unstable species

Chemically unstable species like radicals and ions do not have measurable critical point properties due to thermodynamic instability. However, cubic EOS require data on critical points to predict the thermodynamic properties of the fluid. Since the Lennard-Jones parameters of many species are widely available with the help of molecular dynamics simulations, there have been many efforts to relate cubic equations of state to phase equilibrium data from molecular dynamics simu-

lations via L-J parameters. A review of these studies can be found in Harismiadis et al. [18], and Cabral et al. [5]. In this study, we use the critical properties of a L-J fluid from Cañas-Marín [6]

$$\begin{aligned} T_c &= 1.316 \frac{\varepsilon}{k_B}, \\ V_c &= 3.29 \mathcal{N}_A \sigma^3, \end{aligned} \tag{2.29}$$

where \mathcal{N}_A is the Avogadro number in mol^{-1} . This is also the approach followed by [11]. For Peng-Robinson EOS, the parameter b can be expressed in terms of the collision diameter σ as

$$b = 0.8326 \sigma^3. \tag{2.30}$$

It is to be noted, however, that these rules are considered an approximation and so are only used for the chemically unstable species.

2.3 Caloric equation of state - for e , c_p , h

Having investigated different methods to relate the primary thermodynamic variables, $f(p, V, T)$, we now look at methods for estimation of caloric quantities required to close the energy equation (Eqn. 2.4), such as the internal energy e , the enthalpy h , entropy s , and the constant-pressure specific heat capacity c_p . Unlike pVT data and the ideal gas c_p^o , which are measurable in experiments, e , h and s are just conceptual quantities. Conceptual quantities are state quantities, and do not depend on the exact path of the process, just the initial and final states. Such quantities do not have an absolute value, and only the difference in such quantities can be related to the measurable thermodynamic quantities.

2.3.1 The thermally perfect assumption for an ideal gas

If the internal energy is expressed as a function of temperature and volume $e(T, V)$, a differential change in internal energy is given by

$$de = \left(\frac{\partial e}{\partial T} \right)_V dT + \left(\frac{\partial e}{\partial V} \right)_T dV \quad (2.31)$$

However, it can be shown that $\left(\frac{\partial e}{\partial V} \right)_T = 0$ for an ideal gas, and so the internal energy is only a function of temperature in an ideal gas. This is also true for other derived thermodynamic variables like enthalpy and heat capacities. This is also known as the thermally perfect assumption.

To estimate the extended thermodynamic quantities, e , c_p , h , we make use of the NASA thermodynamic database [41]. The NASA thermodynamic database expresses these properties as a polynomial function of temperature. These coefficients are obtained for a range of stable species, radicals, and ions using experiments and regression analysis, and is a well-established dataset. The ideal gas heat capacity at constant pressure c_p^o is expressed as

$$\frac{c_p^o(T)}{R_u} = \sum_{i=0}^4 a_i T^i = a_0 + a_1 T + a_2 T^2 + a_3 T^3 + a_4 T^4, \quad (2.32)$$

where $a_0 \dots a_4$ are the coefficients of the polynomial obtained using regression analysis in McBride et al. [41]. Two sets of polynomial coefficients are available, one for each temperature interval. Knowing c_p^o , the ideal gas enthalpy h^o can be

easily obtained with knowledge of basic thermodynamic relations, as

$$\begin{aligned}
 dh^o(T) &= c_p^o(T)dT, \\
 h^o(T) &= \int_{298}^T c_p^o(T)dT + \Delta_f h_{298}^o, \\
 \frac{h^o(T)}{R_u T} &= \frac{\int c_p^o(T)dT}{R_u T} + \frac{a_5}{T} = a_0 + \frac{a_1}{2}T + \frac{a_2}{3}T^2 + \frac{a_3}{4}T^3 + \frac{a_4}{5}T^4 + \frac{a_5}{T},
 \end{aligned} \tag{2.33}$$

where $\Delta_f h_{298}^o$ is the standard enthalpy of formation, taken to be equal to $h^o(298)$ for convenience. For the reference elements (O_2 , H_2 , C , etc), $\Delta_f h_{298}^o = h^o(298) = 0$. Similarly, the ideal gas entropy s^o can be written in terms of h^o or c_p^o with the assumption that the system is in thermodynamic equilibrium. The expressions are

$$\begin{aligned}
 ds^o(T) &= \frac{dh^o(T)}{T} = \frac{c_p^o(T)dT}{T}, \\
 s^o(T) &= \int_{298}^T \left(\frac{c_p^o(T)}{T} \right) dT + s^o(298), \\
 \frac{s^o(T)}{R_u} &= \int \left(\frac{c_p^o(T)}{R_u T} \right) dT + a_6 = a_0 \ln T + a_1 T + \frac{a_2}{2}T^2 + \frac{a_3}{3}T^3 + \frac{a_4}{4}T^4 + a_6,
 \end{aligned} \tag{2.34}$$

where a_5, a_6 are the constants of integration, also published in the NASA thermodynamic database [41].

2.3.2 Real gas: departure functions

In the previous section, the caloric quantities were shown to be purely functions of only temperature in an ideal gas case with the thermally-perfect assumption. When the deviations from the ideal gas model are significant, the caloric quantities have a drastic pressure dependence which have to be accounted for. This is typically accounted for by the addition of a pressure-dependent component to the

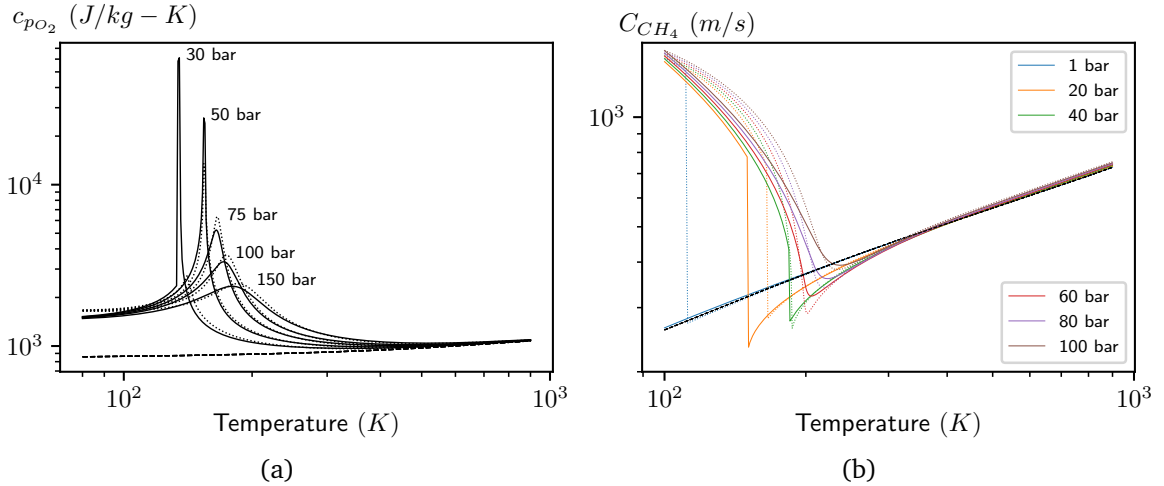


Figure 2.4: Comparison of (a) specific heat capacity for O_2 and (b) speed of sound for CH_4 from Peng-Robinson (—) with the ideal gas model (---) and Coolprop-HEOS (.....).

low-pressure ideal gas component

$$f(T, p) = f^o(T) + f_{dep}(T, p) \quad f \in \{c_p, c_v, e, h, s, \dots\}.$$

The pressure-dependent term $f_{dep}(T, p)$ is commonly known as the departure function. The temperature-dependent term $f^o(T)$ is estimated using NASA polynomials (Eqn. 2.34) as described in the previous section.

Considering the internal energy $e(T, V)$, $\left(\frac{\partial e}{\partial V}\right)_T \neq 0$ for a real gas. The internal energy for a real gas is given by

$$\begin{aligned} e(T, p) &= \int_T^\infty c_v dT + \int_V^\infty \left(\frac{\partial e}{\partial V}\right)_T dV, \\ e(T, p) &= e^o(T) + \left[\int_V^\infty \left(T \left(\frac{\partial p}{\partial T}\right)_V - p\right) dV \right]. \end{aligned} \tag{2.35}$$

The final term is the expression for the departure function of internal energy. Given an analytical expression for $f(p, V, T) = 0$, an exact expression for the departure function can be obtained. For the Peng-Robinson EOS, the exact expressions for

estimating internal energy, enthalpy and heat capacities are of the form

$$\begin{aligned}
 e(T, p) &= e^o(T) + K_1 \left(A_m - T \frac{\partial A_m}{\partial T} \right), \\
 h(T, p) &= h^o(T) + pV - R_u T + K_1 \left(A_m - T \frac{\partial A_m}{\partial T} \right), \\
 c_p(T, p) &= c_p^o(T) - T \frac{(\partial p / \partial T)_{V, X}^2}{(\partial p / \partial V)_{T, X}} - R_u - T \frac{\partial^2 A_m}{\partial T^2} K_1,
 \end{aligned} \tag{2.36}$$

where K_1 is a function of the Peng-Robinson cubic EOS parameters

$$K_1 = \frac{1}{2\sqrt{2}b_m} \ln \left[\frac{V + (1 - \sqrt{2})b_m}{V + (1 + \sqrt{2})b_m} \right].$$

Figure 2.4a compares the specific heat capacity of O_2 obtained from Eqn. 2.36 for Peng-Robinson with the Coolprop reference. Except for the Cp 30 *bar* isobar at low temperature, which is in the liquid region, the derivatives of the Peng-Robinson EOS show excellent agreement in other regions. Figure 2.4b) compares the speeds of sound for CH_4 with reference. The general trends compare reasonably well with the reference values, however the accuracy of Peng-Robinson is very limited at lower temperatures.

2.3.3 Mixing and combination rules

The previous sections have described the details of thermodynamic property estimation for a pure species. To extend the Peng-Robinson EOS (Eqn. 2.25) to predict the properties of a multi-component mixture, we can write

$$p = \frac{R_u T}{V - b_m} - \frac{A_m}{V^2 + 2b_m V - b_m^2}, \tag{2.37}$$

where A_m and b_m are the cubic equation parameters averaged over the entire mixture. To obtain these aggregate EOS parameters, we would need expressions

known as mixing rules. The choice of mixing rules can be a crucial factor in determining the accuracy of the property estimation. The common choice for mixing rules for many cubic equations of state are from the van der Waals one-fluid (vdW1f) theory. We use the vdW1f-type mixing rules from Harstad et al. [19], which is derived from work by Wong and Sandler [76]. With these rules, the mixture EOS parameters are given by

$$\begin{aligned}
 A_m &= \sum_i^{N_s} \sum_j^{N_s} X_i X_j A_{ij} \\
 b_m &= \sum_i^{N_s} X_i b_i
 \end{aligned}
 \tag{2.38}$$

where X_i denotes the mole fraction of the component i in the mixture. Quantities A_{ij} and b_i denote the pure-species parameters corresponding to the binary species pair (i, j) . These can be related to the critical properties of the binary species pair as

$$\begin{aligned}
 A_{ij} &= 0.457236 \frac{(R_u T_{c,ij})^2}{p_{c,ij}} \alpha(T_{r,ij}, \omega_{ij}) \\
 b_i &= 0.077796 \frac{R_u T_{c,ij}}{p_{c,ij}} \\
 \alpha(T_{r,ij}, \omega_{ij}) &= \left(1 + f(\omega_{ij}) \left(1 - \sqrt{\frac{T}{T_{c,ij}}} \right) \right)^2
 \end{aligned}
 \tag{2.39}$$

where $f(\omega_{ij})$ is similar in form to Eqn. 2.28. To relate the binary species-pair properties to pure-fluid properties, the following combination rules are used

$$\begin{aligned}
 T_{c,ij} &= \sqrt{T_{c,i} T_{c,j}} (1 - k_{ij}) \\
 p_{c,ij} &= Z_{c,ij} \frac{R_u T_{c,ij}}{V_{c,ij}} \\
 \omega_{ij} &= \frac{1}{2} (\omega_i + \omega_j)
 \end{aligned}
 \tag{2.40}$$

The binary interaction parameter k_{ij} accounts for the effects of attractive or repulsive forces between molecules of different species. This is an empirical value, specific to the EOS used, and is obtained by fitting experimental observations to the EOS state. Data on binary interaction parameters are scarce. This study assumes k_{ij} to be zero, except in the validation tests described below. The remaining combination rules necessary to close the above system of equations are

$$\begin{aligned} V_{c,ij} &= \frac{1}{8}((V_{c,i})^{1/3} + (V_{c,j})^{1/3})^3 \\ Z_{c,ij} &= \frac{1}{2}(Z_{c,i} + Z_{c,j}) \end{aligned} \tag{2.41}$$

We validate our implementation of the mixing rules with experimental data for a ternary mixture of methane (CH_4), ethane (C_2H_6) and propane (C_3H_8) from Cristancho et al. [9]. Further, we compare our results with computational data from Masquelet [39], which also implements the Peng-Robinson EOS with mixture rules from Harstad et. al [19]. The results presented in the following tests use a mixture containing 0.095039 moles of methane, 0.03961 moles of ethane and 0.01000 moles of propane. The following tests also make use of empirically-determined binary interaction parameters as specified in [9]. The binary interaction parameters for methane–ethane, methane–propane, and ethane–propane pairs are -0.0021 , -0.0029 , and 0.008 respectively.

Both the present work and the Peng-Robinson reference implementation in Masquelet [39] use identical expressions for mixing rules, partial molar volumes, and partial molar enthalpies. In addition, the values of the numerical Peng-Robinson constants, the value of the universal gas constant, and the critical properties of the test species are also identical.

First, we compare the partial molar volumes for the reference mixture at

Molar volume ($\times 10^{-3} \text{ m}^3/\text{mol}$)	PREOS	Reference	Relative Error %
V_{mix}	0.5464	0.5534	-1.26
V_{CH_4}	0.5510	0.5584	-1.33
$V_{C_2H_6}$	0.4703	0.4718	-0.32
$V_{C_3H_8}$	0.4044	0.4072	-0.69

Table 2.2: Partial and mixture molar volumes of a mixture containing 0.095039 moles of CH_4 , 0.03961 moles of C_2H_6 , and 0.01000 of C_3H_8 at $T = 350 \text{ K}$, $p = 4.998 \text{ MPa}$. PREOS - Present study, Reference - Masquelet[39].

T (K)	p (MPa)	ρ_{PREOS} (kg/m^3)	ρ_{ref} (kg/m^3)	Relative Error %
300	4.965	37.7504	37.1883	1.51
300	8.002	64.6633	63.0133	2.62
350	2.002	11.9344	11.8745	0.50
350	4.998	30.893	30.4957	1.30

Table 2.3: Densities of a mixture containing 0.095039 moles of CH_4 , 0.03961 moles of C_2H_6 , and 0.01000 of C_3H_8 at specified p, T . PREOS - Present study, Reference - Masquelet[39]

$T = 350 \text{ K}$, $p = 4.998 \text{ MPa}$ with the numerical implementation in Masquelet [39]. The results are tabulated in Table 2.2, and show very good agreement with the reference values. Our implementation under predicts molar volumes by $\simeq 1\%$. Next, we compare the mixture densities at several different temperatures and pressures, tabulated in Table 2.3. The average deviation remains relatively small. Finally, we compare the mixture densities over a range of pressures for several different temperatures with the experimental data from Cristancho [9] and numerical implementation in Masquelet [39]. Figure 2.5 shows that the Peng-Robinson implementation in the present work appears to slightly over-predict mixture densities compared to the reference. However, we find the margin of error to be acceptable.

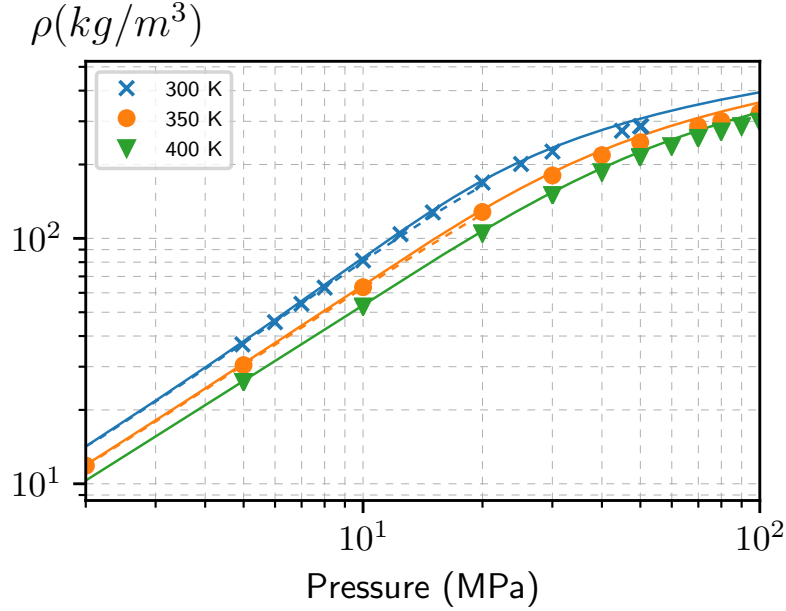


Figure 2.5: Densities of a mixture containing 0.095039 moles of CH_4 , 0.03961 moles of C_2H_6 , and 0.01000 of C_3H_8 at $T = 300, 350, 400$ Kelvins using the present implementation (Solid lines), reference numerical data [39] (Dashed) and experimental data [9] (Symbols).

2.4 Transport properties

In chemically reacting flows with multiple species, there are multiple modes for the diffusion of fluid properties. There is diffusion of momentum due to the viscosity of the fluid. Thermal diffusion or the diffusion of thermal energy is brought about by the fluid's thermal conductivity. In a multi-component mixture, there is also the differential diffusion of individual species based on concentration gradients, pressure gradients, temperature gradients (Soret effect) or electric fields [51]. This study is limited in scope to the species mass diffusion due to concentration gradients.

The following subsections describe the estimation of transport coefficients for the diffusion of mass, momentum and heat, which are required to close the system of equations 2.1 through 2.4. The low-pressure property estimation methods are described first, followed by methods for high-pressure estimation.

2.4.1 Low-pressure transport coefficients

Low-pressure property estimation methods are based on the kinetic theory of gases, and subsequent modifications by Chapman and Enskog. Chapman and Enskog extended formulations for viscosity and thermal conductivity from hard spheres to a model with intermolecular forces. The Lennard-Jones potential well, previously introduced in Section 2.2, is a popular semi-empirical model for the intermolecular potential. The property estimations make use of Lennard-Jones parameters σ is the collision diameter, and ε is the well depth.

The Chapman-Enskog theory provides integral expressions for transport properties at low densities, and monoatomic gases as a function of the intermolecular potential energy $\varphi(r)$.

2.4.1.1 Coefficient of viscosity

Using the kinetic theory of gases and mean free paths, Maxwell (1860) derived a basic expression for the coefficient of viscosity for a monoatomic gas, comprised of rigid spheres of diameter d and mass m , without any intermolecular forces between them, to be

$$\mu^o = \frac{2}{3\pi} \frac{\sqrt{\pi m k_B T}}{\pi d^2} \left[\frac{g}{cm - s} \right], \quad (2.42)$$

where k_B is the Boltzmann constant. The above expression features a square root dependence on temperature, which does not adequately capture the true temperature dependence of viscosity. To develop a more accurate kinetic theory of monoatomic gases, Enskog accounted for the intermolecular forces of attraction between the molecules. The viscosity of a pure monoatomic gas can be expressed

as a function of the Lennard-Jones parameters as

$$\mu^o = \frac{5}{16} \frac{\sqrt{\pi m k_B T}}{\pi \sigma^2 \Omega_v} = 2.6693 \frac{(WT)^{1/2}}{\sigma^2 \Omega_v} \times 10^{-6} \left[\frac{kg}{m-s} \right], \quad (2.43)$$

where W is the molecular mass (g/mol), σ is the collision diameter in Å ($10^{-10} m$), and the temperature T is in K . The collision integral Ω_v is a dimensionless function of the reduced temperature $T^* = k_B T / \varepsilon$, and represents the deviation from a rigid-sphere model. The collision integral is equal to unity for a gas with rigid spheres of diameter σ and without any intermolecular forces. We use the collision integral by Monchick and Mason as found in Poling [51]

$$\Omega_v = A[(T^*)^{-B}] + C[e^{-DT^*}] + E[e^{-FT^*}].$$

Constants A through E are given in [51]. Despite Eqn. 2.43 having been developed from the kinetic theory for monoatomic gases, it has been found to hold well for polyatomic gases as well [2].

To estimate the mixture-averaged viscosity, the Wilke's mixing rule, modified by Bird [2], is employed. It is of the form

$$\mu_{mix}^o = \sum_{k=1}^{N_{sp}} \frac{X_k \mu_k^o}{\sum_{j=1}^{N_{sp}} X_j \Phi_{kj}},$$

where

$$\Phi_{jk} = \frac{1}{\sqrt{8}} \left(1 + \frac{W_j}{W_k}\right)^{-1/2} \left[1 + \left(\frac{\mu_j^o}{\mu_k^o}\right)^{-1/2} \left(\frac{W_k}{W_j}\right)^{1/4}\right]^2,$$

and W_j is the molecular mass of species j .

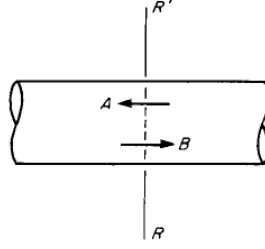


Figure 2.6: Illustration of mass diffusion process. Figure from Poling et al. [51].

2.4.1.2 Mass diffusion model and diffusion coefficients

For a binary mixture, Fick's first law of diffusion relates the diffusive flux \mathbf{j}_k of species k to its concentration gradient ∇X_k by means of the binary mass diffusion coefficient D_{kj} [27]

$$\mathbf{j}_k = -\rho D_{kj} \nabla X_k. \quad (2.44)$$

Consider a binary mixture of species A and B , where A and B are diffusing across the plane RR' , as illustrated in Figure 2.6. If j_A represents the net mass flux of A , then

$$\begin{aligned} j_A &= -\rho D_{AB} \frac{\partial X_A}{\partial z}, \\ j_B &= -\rho D_{BA} \frac{\partial X_B}{\partial z}, \end{aligned} \quad (2.45)$$

and since $j_A + j_B = 0$, we get

$$D_{AB} = D_{BA}.$$

The mass diffusivity for a species j in species k is a function of the temperature T and pressure p . The Chapman-Enskog expression for binary mass diffusivity is of the form

$$D_{jk}^o = \frac{3}{16} \frac{\sqrt{2\pi k_B^3 T^3 / m_{jk}}}{p \sigma_{jk}^2 \Omega_D(T_{jk}^*)} \left[\frac{m^2}{s} \right], \quad (2.46)$$

where \underline{p} is the pressure in *bar*, the temperature T is in K , Ω_D is the non-dimensional collision integral for mass diffusion, and is a function of the reduced temperature $T_{jk}^* = k_B T / \varepsilon_{jk}$. The combination rules for the reduced mass m_{jk} (kg), collision diameter σ_{jk} (m) and well-depth ε_{jk} (J) of the (j, k) species pair are expressed as

$$m_{jk} = \frac{1}{\mathcal{N}_A} \frac{W_j W_k}{W_j + W_k}, \quad \sigma_{jk} = \frac{\sigma_j + \sigma_k}{2}, \quad \varepsilon_{jk} = (\varepsilon_j \varepsilon_k)^{1/2}.$$

This study uses the diffusion collision integral Ω_D from Neufield (1972), which is of the form

$$\Omega_D(T_{jk}^*) = \frac{A}{(T_{jk}^*)^B} + \frac{C}{\exp(DT_{jk}^*)} + \frac{E}{\exp(FT_{jk}^*)} + \frac{G}{\exp(HT_{jk}^*)}.$$

Constants A through H can be found in [51].

Before we describe the averaged mass diffusion coefficients, we introduce the concept of mass diffusion velocities by re-expressing the Fickian mass flux from Eqn. 2.44 as

$$j_k = -\rho X_k \mathbb{V}_k \quad (2.47)$$

where the diffusion velocity V_k is given by the Hirschfelder-Curtiss approximation

$$\mathbb{V}_k = -\frac{1}{X_k} D_k \nabla X_k \quad (2.48)$$

where D_k is the mixture-averaged molecular diffusivity for species k

$$D_k = \frac{1 - Y_k}{\sum_{j \neq k} X_j / D_{jk}} \quad (j, k) \in \mathcal{S} | j \neq k \quad (2.49)$$

Due to local variations in the species mass fractions because of diffusion, a correction velocity is necessary. This also ensures that the species conservation equations correctly add up to give the continuity equation. There are several ways to ensure

mass conservation. In the first approach, we add an artificial correction velocity \mathbb{V}_c to ensure that the species conservation equations essentially reduce the mass continuity equation

$$\mathbb{V}_c = \sum_k D_k \frac{W_k}{W} \frac{\partial X_k}{\partial x}.$$

The diffusion velocity of species k is then given by

$$\mathbb{V}_k = -D_k \frac{\nabla X_k}{X_k} + \mathbb{V}_c.$$

In the second approach, the composition of the diluent species (typically Ar or N_2) is artificially manipulated to ensure that the total mass fraction is equal to 1 after every Runge-Kutta sub-step

$$Y_{diluent} = 1 - \sum_k Y_k \quad k \in \mathcal{S} \setminus \{diluent\}.$$

In this case, V_c is set to zero. We use the second approach for all computations of premixed flames.

2.4.1.3 Coefficient of thermal conductivity

Using the kinetic theory for monoatomic gases, the expression for thermal conductivity of a non-attracting rigid-sphere molecule can be derived as Bird et al. [2],

$$\lambda_{mono} = \frac{2}{3\pi} \frac{\sqrt{\pi m k_B T}}{\pi d^2} c_{v,trans}, \quad (2.50)$$

where the specific heat at constant volume for a monoatomic gas $c_{v,trans} = \frac{3}{2}k_B/m$.

The Chapman-Enskog theory extends this to account for intermolecular forces

of attraction, and expresses the thermal conductivity in terms of the L-J parameters.

$$\lambda_{mono} = \frac{25}{32} \frac{\sqrt{\pi m k_B T}}{\pi \sigma^2 \Omega_v} c_{v,trans} = \frac{5}{2} \mu c_{v,trans}. \quad (2.51)$$

For a polyatomic gas molecule, the thermal conductivity is the sum of the translational, rotational and vibrational components. We use the form given by Warnatz [72] as

$$\lambda^o = \mu^o (f_{trans} c_{v,trans} + f_{rot} c_{v,rot} + f_{vib} c_{v,vib}),$$

where

$$\begin{aligned} f_{trans} &= \frac{5}{2} \left(1 - \frac{2A}{\pi} \frac{c_{v,rot}}{c_{v,trans}} \right), \\ f_{rot} &= f_{vib} \left(1 + \frac{2A}{\pi} \frac{1}{B} \right), \\ f_{vib} &= \frac{\rho D_{kk}^o}{\mu^o}. \end{aligned} \quad (2.52)$$

In the above expressions, D_{kk} is the self-diffusion coefficient, and is estimated by Eqn. 2.46. Parameters A and B are given by the following expressions

$$\begin{aligned} A &= \frac{5}{2} - f_{vib}, \\ B &= Z_{rot} + \frac{2}{\pi} \left(\frac{5}{3} \frac{W c_{v,rot}}{R_u} + f_{vib} \right). \end{aligned}$$

The rotational relaxation number Z_{rot} represents the number of collisions necessary to transfer a quantum of energy from the rotational mode to translational mode. The functional form of Z_{rot} is described in Kee [25].

The total specific heat capacity at constant volume, c_v , is available through experimental data regressed in the form the NASA polynomial coefficients. The vibrational component of c_v can be estimated as

$$c_{v,vib} = c_v - c_{v,trans} - c_{v,rot}. \quad (2.53)$$

To obtain mixture-averaged thermal conductivities, the following mixing rule is used

$$\lambda^o = \frac{1}{2} \left(\sum_{k=1}^{N_s} X_k \lambda_k^o + \frac{1}{\sum_{k=1}^{N_s} X_k / \lambda_k^o} \right).$$

2.4.2 High-pressure transport models

The Chapman-Enskog theory provides theoretical expressions for the transport coefficients of gases as functions of temperatures at low pressures only. At higher pressures characteristic of supercritical combustion, we would need better models to estimate viscosity, thermal conductivity and molecular diffusivities.

A good high-pressure transport model must accurately capture the dense-fluid effects at high pressures and low temperatures, while being able to smoothly transition to the predictions of low-pressure transport models at low pressures and/or high temperatures. Transport models based on the corresponding states model express the high-pressure properties as a factor of the corresponding low-pressure properties, and consequently transition well to the low-pressure model. In addition to the above requirements, it's also important to predict the correct viscosity and thermal conductivity of water at high temperatures. Any property estimation method must be extensible to a multi-component mixture as well.

Among the dense-gas viscosity estimation based on the corresponding states method, the methods due to Reichenberg (1979), Lucas (1984), Chung (1988) are popular. The Reichenberg was designed for organic gases, and does not work for non-organic and polar gases. While the Lucas method converges to low-pressure values at ideal conditions, it does not handle polar molecules including water. However, it can handle quantum fluids like H_2 , He .

The TRAPP method is also a corresponding states method for the estimation of viscosity and thermal conductivity. It gives the properties as a factor of the low-pressure value for propane. While TRAPP gives the correct thermal conductivity of mixtures at low pressures and high temperatures, it does not account for polarity of molecules. As a result, the viscosity of water is poorly predicted.

For this study, we use the high-pressure viscosity and thermal conductivity correlations of Chung et al. (1988) [8]. For the high-pressure molecular diffusivities, we use the Takahashi correlation [69].

2.4.2.1 Chung correlation: for μ and λ

Chung et al. [8] extended the Chapman-Enskog theory to develop semi-empirical correlations for dense-gas viscosity and thermal conductivity as functions of temperature and density. Firstly, Chung et al. [8] extended Eqn. 2.43 to polar and non-polar polyatomic gases by accounting for molecular shapes, electrostatic molecular forces and hydrogen bonding using a correction factor F_c , which is given by the expression $F_c = 1 - 0.2756\omega + 0.059035\mu_r^4 + \kappa$, and is a function of the acentric factor ω accounts for molecular shape, κ is an empirically-determined correction factor for hydrogen-bonding substances such as alcohols, acids and water. μ_r is the dimensionless dipole moment, expressed as $\mu_r = 131.3\mu / \sqrt{V_c T_c}$. With this the corrected expression for viscosity becomes

$$\mu_c^o = \frac{(26.69)(WT)^{1/2}}{V_c^{2/3}\Omega_v} F_c, \quad (2.54)$$

For the low-pressure thermal conductivity, Chung developed the following expression

$$\lambda_c^o = \mu_c^o \frac{3.75R_u}{W} \Psi \quad (2.55)$$

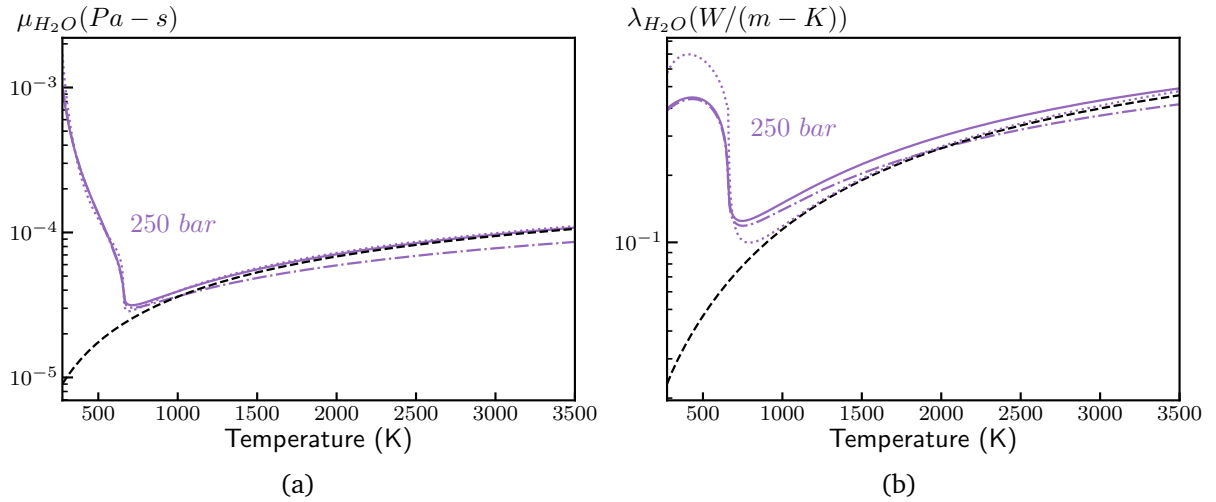


Figure 2.7: Comparison of the a) viscosity and b) thermal conductivity for H_2O using the original Chung correlation [8] (---), modified Chung correlation (—), low-pressure Chapman-Enskog correlations (- - -) and reference data (.....).

where

$$\Psi = 1 + \alpha \left(\frac{0.215 + 0.28288\alpha - 1.061\beta + 0.26665Z_{coll}}{0.6366 + \beta Z_{coll} + 1.061\alpha\beta} \right) \quad (2.56)$$

$$\alpha = \frac{c_v W}{R_u} - \frac{3}{2}$$

where Z_{coll} measures the number of collisions required to convert the internal energy to translational energy. At high temperatures, the internal energy is the dominant mode of energy, and the system requires an extremely large number of collisions to convert it to translational energy. Hence the model for Z_{coll} used here is

$$Z_{coll} = 2.0 + 10.5T_r^2. \quad (2.57)$$

The parameter β is the same as $(f_{vib})^{-1}$, and is empirically correlated with the acentric factor ω for non-polar hydrocarbons.

$$\beta = 0.786231 - 0.710907\omega + 1.31683\omega^2 \quad (2.58)$$

For polar compound, see Chung et al. [8] for experimentally determined values for β . This correction is not extensible to mixtures however.

Chung et al. [8] then extended the low-pressure formulation to account for dense-fluid effects. The real gas viscosity can be written as the sum of the correct low-pressure viscosity μ_c^o (Eqn. 2.54) and a dense-gas contribution μ_p , resulting in

$$\mu_c = \mu_c^o (1/G_2(A_i) + A_6y) + \mu_p \quad (2.59)$$

where μ_p is the dense-gas contribution, given by

$$\mu_p = 36.34 \times 10^{-6} \frac{\sqrt{WT_c}}{V_c^{2/3}} A_7 y^2 G_2(A_i) \exp\left(A_8 + \frac{A_9}{T^*} + \frac{A_{10}}{T^{*2}}\right) \quad (2.60)$$

Similarly, the real gas thermal conductivity λ_c can be expressed as a function of the low-pressure thermal conductivity λ_c^o (Eqn. 2.55) and a dense-gas contribution λ_p , resulting in

$$\lambda_c = \lambda_c^o (1/G_2(B_i) + B_6y) + \lambda_p \quad (2.61)$$

with the dense-gas contribution taking the form λ_p

$$\lambda_p = 3.58 \times 10^{-3} \sqrt{\frac{T_c}{WV_c^3}} B_7 y^2 G_2(B_i) \sqrt{T_r} \quad (2.62)$$

For the above expressions, the reduced density number y is given by

$$y = \frac{\rho V_c}{6}, \quad (2.63)$$

and G_1, G_2 are expressed as

$$G_1 = \frac{1 - 0.5y}{(1 - y)^3}, \quad (2.64)$$

$$G_2(E_i) = \frac{E_1[1 - \exp(-E_4y)]/y + E_2G_1\exp(E_5y) + E_3G_1}{E_1E_4 + E_2 + E_3}.$$

The function G_2 tends to unity at low densities, making μ_p, λ_p negligible and the

effective viscosity and thermal conductivity tending to the corresponding low-pressure values μ_c^o and λ_c^o . At high densities, G_2 sharply increases thereby making μ_p and λ_p dominant. Parameters E_1 through E_{10} are linear functions of the acentric factor ω , reduced dipole moment μ_r , and association factor κ

$$E_i = a_i + b_i\omega + c_i\mu_r^4 + d_i\kappa \quad E_i \in \{A_i, B_i\} \quad (2.65)$$

See Chung et al. [8] for the coefficients tabulated for viscosity and thermal conductivity.

Chung et al. [8] provided mixing and combination rules in order to extend the above pure-fluid property estimation to mixtures. See Chung et al. [8] for the detailed set of rules.

Figures 2.7, 2.8 and 2.9 compare the performance of the Chung correlation with the reference data. A more comprehensive assessment of the Chung correlation for the species prominent in this study (chemistry set) can be found in Appendix C. The Chung correlation is overall sufficiently accurate in the dense-gas region. With the exception of CH_4 viscosity, the transport properties of reactant species O_2 and CH_4 have an average error (AAD) of less than 9% in both the low-temperature and high-temperature ranges. The deviation in CO_2 properties is also acceptably small ($\lesssim 8\%$). While the low-temperature λ deviation of H_2O is 28%, it is the high-temperature μ and λ deviations of 18 and 8 percentages compared to the respective Chapman-Enskog AADs of 5 and 9 than concern us. Since the dynamics of flame is dependent on the thermal conductivity in the pre-flame region and the reaction zone, it is necessary to estimate the correct value of transport properties at moderate to high temperatures. Considering that water vapor is a major product of the reaction, it is important to obtain correct transport properties of water at

moderate to high temperatures.

The second consideration is that to investigate the effect of high-pressure property estimation systematically, it's preferable for the high-pressure correlations to smoothly attain the values of the low-pressure correlations. One option is to use the Chung (1984) correlation for our low-pressure simulations so that the real gas flames will transition smoothly. The issue with this is threefold. First, it is much less accurate than Enskog predictions at high temperatures for Water. Secondly, it is not the standardly used low-pressure transport method for combustion simulations and does not help us validate low-pressure results with widely available low-pressure data. Thirdly, Chung correlation cannot handle property estimation for H_2 at moderate to high temperatures.

Since, Chapman-Enskog provides reasonable values of H_2 and H_2O transport properties at high temperatures, and is the established transport property method at low pressures, we investigate replacing the Chung high-pressure correlation to scale up from the CE low-pressure method. Replacing the low-pressure viscosity in equations 2.59 and 2.61 with equations 2.43 and 2.52, resulting in the expressions

$$\begin{aligned}\mu'_c &= \mu^o (1/G_2(A_i) + A_6y) + \mu_p \\ \lambda'_c &= \lambda^o (1/G_2(B_i) + B_6y) + \lambda_p\end{aligned}\tag{2.66}$$

The results from the above modification are tabulated in Appendix C. We find acceptably low AADs in high-temperature ranges for H_2O and H_2 of $\lesssim 11\%$ and $\lesssim 10\%$, compared to 18% and 23% using Chung. The high-pressure AADs of the species are comparable to the original Chung high-pressure estimation, with the exception of H_2 .

We had also considered a blending function to smoothly transition from

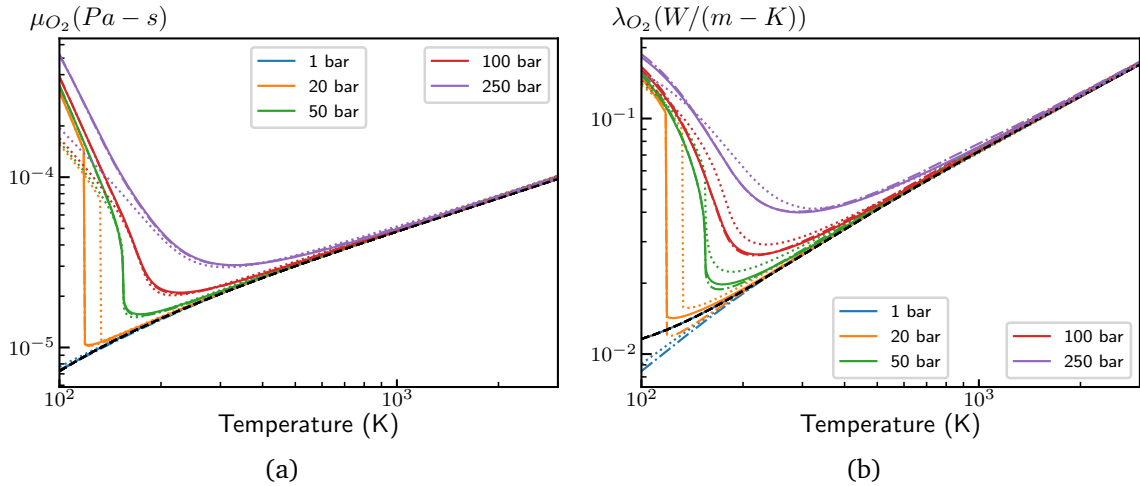


Figure 2.8: Pure-fluid a) viscosities and b) thermal conductivities of Oxygen using the low-pressure correlation (---), the original (-·-·) and modified (—) Chung correlation and the reference values (····).

high-pressure property estimation at low temperatures to the default low-pressure property estimation at high temperatures. This is a less elegant solution, but it also serves to affect the shape of the high-pressure correlations and ultimately we decided against it.

2.4.2.2 Takahashi correlation: for D_{AB}

Binary mass-diffusion coefficients vary inversely with pressure at low pressures. This behavior can also be seen from the models for low-pressure mass diffusivity described in Section 2.4.1.2. However, this behavior is not valid at high pressures and we need a more accurate model for binary diffusion coefficients.

Predictive methods for the binary mass-diffusion coefficients of dense gases can be roughly classified into three categories: methods based on the Stokes-Einstein formula, methods based on Rough-Hard-Sphere model and the corresponding states principle. For a comprehensive treatment of this topic, see Medina [42]. The state of the art in binary diffusion coefficient estimation is the work

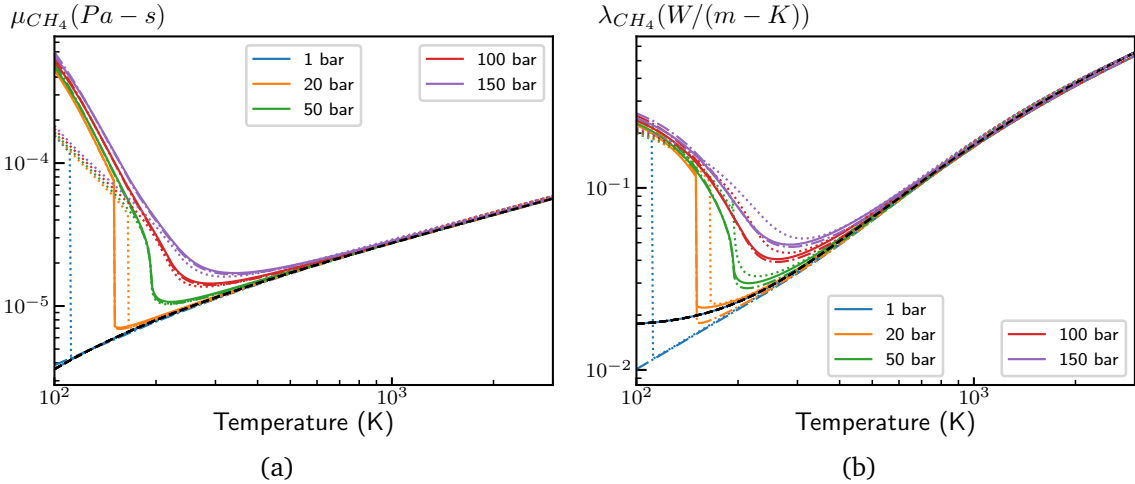


Figure 2.9: Pure-fluid a) viscosities and b) thermal conductivities of Methane using the low-pressure correlation (---), the original (-·-·) and modified (—) Chung correlation and the reference values (····).

from Magalhães [35, 36]. However, this is more computationally involved than is desired for the present study.

A corresponding states approach to estimating the binary diffusivity is preferable for two reasons. Firstly, such methods are simple and computationally efficient, give qualitatively correct values. Secondly, these methods involve a multiplicative factor which tends to the correct low-pressure values.

For the purposes of this study, we model the dense-gas mass diffusivity using the Takahashi method [69]. This work is based on the corresponding states principle, and relates the ratio of the high-pressure and low-pressure diffusivities to the critical properties of the species in the mixture.

$$\frac{D_{jk}p}{(D_{jk}p)^o} = f(T_r, P_r) \quad (2.67)$$

Takahashi published a generalized chart for estimating the correction factor $f(T_r, P_r)$ as a function of reduced temperatures and pressures for self-diffusion and binary-diffusion coefficients. According to Takahashi, the average deviation between the

observed values and the chart for several binary mixtures over 102 isotherms is around 4.1%.

The reduced temperature and pressure are estimated with respect to the pseudo-critical temperature and pressure of the binary species pair (j, k) , as $T_r = T/T'_c$ and $p_r = T/p'_c$, where

$$\begin{aligned} T'_c &= x_j T_{c,j} + x_k T_{c,k} \\ p'_c &= x_j p_{c,j} + x_k p_{c,k} \end{aligned} \tag{2.68}$$

For ease of chart lookup simpler, Takahashi provided curve fits estimated using the method of least squares. In our experience, however, the correction factors estimated using the fitted correlation were not smooth, and had significant jumps at low reduced temperatures. In this study, we were able to obtain smoother functions by digitizing the plot of the correction factor chart in Takahashi. To get the correction factors at intermediate values of T_r, p_r , a bilinear interpolation is performed on the set of two-dimensional digitized data. When the operating states fall outside the bounds of the chart, we enforce a set of rules for the boundary cases. If the reduced binary pressure $P_r < 0.05$, the Takahashi factor f is set to unity. This ensures agreement with low-pressure mass-diffusivities at sufficiently low pressures. At the other extreme, if $P_r \geq 4.8$, the Takahashi factor is set to the last available data point for a given temperature (interpolation, if needed). For intermediate cases of pressure, if the reduced binary temperature $T_r < 0.9$, we use the interpolated value of f on the $T_r = 0.9$ isotherm. If $T_r > 5$, we use the interpolated value on the $T_r = 5$ isotherm. In the interior of the domain, we use a simple bilinear interpolation.

This study's implementation of the Takahashi correlation is validated with

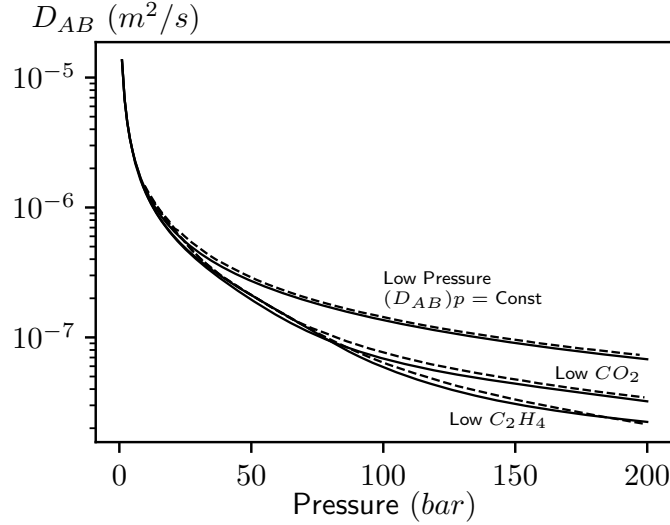


Figure 2.10: Comparison of binary mass diffusivity in a $CO_2 - C_2H_4$ mixture at 323.23K using the Takahashi correlation(—) with the reference Poling[51](---).

Poling[51], for a binary carbon dioxide-ethylene system at 323.23 K (Figure 2.10). Real-gas binary mass-diffusivities have a stronger inverse dependence on pressure (around 25 – 100 bar) compared to the low-pressure expressions from the Chapman-Enskog theory, which have a constant $D_{AB}p$. Note that for real gas mass diffusivities, $D_{AB} \neq D_{BA}$ at higher pressures. We find our implementation to be in good agreement with Poling[51].

2.5 Chemical kinetics model

In this section, we provide a brief survey of the categories of models available to close the chemical production term $\dot{\omega}$ in the species conservation equation (Eqn. 2.2). Chemical kinetics models can be broadly classified into fast chemistry models and finite-rate chemistry models [27]. Fast chemistry models are based on the assumption that the chemical reactions take place instantaneously, or that the chemical time scales are much shorter than the timescales of transport processes. The assumption of infinitely fast timescales allows for faster computation of reacting flows, as the range of timescales that needs to be resolved is drastically reduced

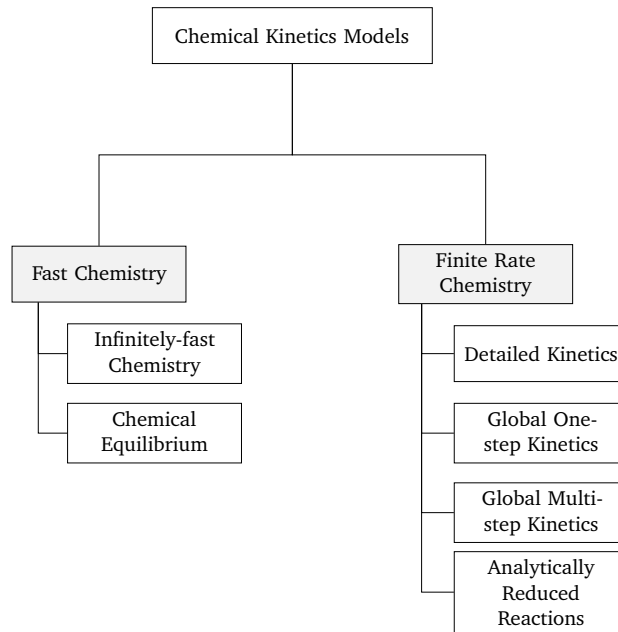


Figure 2.11: Hierarchy of chemical kinetics models. Adapted from Kee et al. [27]

and the problem becomes less stiff. Flamelet models commonly used in numerical simulations of turbulent reacting flows are one subtype of such models, involving an infinitely fast one-step global reaction. Another subtype are models which assume chemical equilibrium at every point in the flow field, and hence the equilibrium mixture composition is determined by minimizing the Gibbs free energy for a given mixture fraction, temperature and pressure. The assumption of fast chemistry in the above models allows for a fast and reasonable estimation of product temperature, major species composition and even flame speeds in some cases. However, such models are unable to predict the composition of minor species like NO_x , and the extinction properties of the flames.

For accurate modeling of the intricacies of reacting flows, the time scales of the reactions must be modeled. Such models are classified as finite-rate chemistry models. Depending the range of time scales and species modeled, there are different types of finite-rate models. Global one-step kinetics consider the whole reaction as proceeding from reactants to products in a single step, in a finite amount of time,

without the formation or destruction intermediate products. Global multi-step kinetics improve upon the accuracy of one-step mechanisms by considering the most significant intermediate reactions. Detailed chemistry models on the other hand are comprised of a number of elementary reactions, with the intention of modeling the reactions as they occur on a molecular level. The complexity of such detailed kinetic models have a logarithmic dependence on the number of carbon atoms in the fuel, ruling out the use of such models for turbulent reacting flow simulations. Analytical methods are a subtype of finite-rate models that deploy algorithms to reduce global reaction kinetics to the most important skeletal chemistry pathways. One such method is the intrinsic low dimension manifold (ILDM) method, which uses concepts from dynamical methods to reduce the state space of a reaction system, allowing for tabulation and later use in a turbulent combustion simulation.

In order to model the flame properties with the greatest accuracy, the present study uses detailed chemical kinetics. To simplify the process of implementation of detailed kinetics in the solver, we integrate the pre-verified kinetics routines from the open-source combustion utility, [14].

2.5.1 Detailed chemical kinetics

Consider the following elementary, bimolecular reaction,



where a, b, c, d are the stoichiometric coefficients of species $\mathbf{A}, \mathbf{B}, \mathbf{C}, \mathbf{D}$ respectively. Reactants \mathbf{A} and \mathbf{B} are in equilibrium with products \mathbf{C} and \mathbf{D} , with the reaction proceeding in both forward and reverse directions. The law of mass action states that the rate of a chemical reaction is directly proportional to the activities or

concentrations of the reactants. The rate of formation of the product **C** is expressed as

$$\frac{d[\mathbf{C}]}{dt} = k_f(T) [\mathbf{A}]^a [\mathbf{B}]^b,$$

where $[\mathbf{A}]$, $[\mathbf{B}]$ indicate the molar concentrations of species **A**, **B**, expressed as

$$[\mathbf{A}] = \rho X_{\mathbf{A}}/W$$

and k_f is the forward rate constant, expressed using the Arrhenius form

$$k_f(T) = \mathcal{A}T^\beta \exp(-E_a/R_u T).$$

Here \mathcal{A} is the pre-exponential factor, β is the temperature exponent, and E_a is the activation energy. Similarly, the rate of change of concentration of **A** is expressed as

$$\frac{d[\mathbf{A}]}{dt} = k_r(T) [\mathbf{C}]^c [\mathbf{D}]^d,$$

where k_r is the reverse rate constant. The forward and reverse rate coefficients are related by the expression

$$k_r = \frac{k_f}{K_c},$$

with K_c being the equilibrium constant based on concentrations

$$K_c = K_p(T) \left(\frac{p_{atm}}{R_u T} \right)^{\sum_{k=1}^K \nu_k}.$$

$K_p(T)$ is the equilibrium constant based on partial pressures

$$K_p(T) = \exp \left(\frac{\Delta s^o}{R_u} - \frac{\Delta h^o}{R_u T} \right),$$

where the quantities Δs^o and Δh^o signify the change in entropy and enthalpy during the process of conversion from reactants to products.

Any arbitrarily detailed chemical mechanism set consisting of I elementary reactions involving S major and minor species, and reaction intermediates can be expressed using a compact notation,

$$\sum_{k \in S} v'_{ki} \chi_k \Leftrightarrow \sum_{k \in S} v''_{ki} \chi_k \quad i \in I$$

where v_{ki} represents the stoichiometric coefficient for species k and reaction i , and the symbol for the k^{th} species is represented by χ_k . The superscripts ' and '' to v_{ki} represent forward and reverse stoichiometric coefficients respectively. The net production rate $\dot{\omega}_k$ for the k^{th} species is expressed as the following sum

$$\dot{\omega}_k = \sum_{i \in I} v_{ki} Q_i \quad k \in S,$$

where $v_{ki} = v''_{ki} - v'_{ki}$, and Q_i is the rate of progress (ROP) variable for the i^{th} reaction, given by

$$Q_i = k_{fi} \prod_{k \in S} [\chi_k]^{v'_{ki}} - k_{ri} \prod_{k \in S} [\chi_k]^{v''_{ki}}$$

where k_{fi} and k_{ri} are forward and reverse rate constants for the i^{th} reaction.

Giovangigli [11] used the non-ideal form of the chemical rate of progress to ensure non-negative entropy production. Giovangigli found that the standard Arrhenius formulation is insufficient at extremely high pressures of 1000 *atm*, but is still applicable at pressures of up to 100 *atm*. Hence, we use the standard ideal gas Arrhenius formulation for the rate of progress Q_i^o for the i th reaction:

$$Q_i^o = k_{fi} \prod_{k=1}^K [\chi_k]^{v'_{ki}} - k_{ri} \prod_{k=1}^K [\chi_k]^{v''_{ki}} \quad (2.69)$$

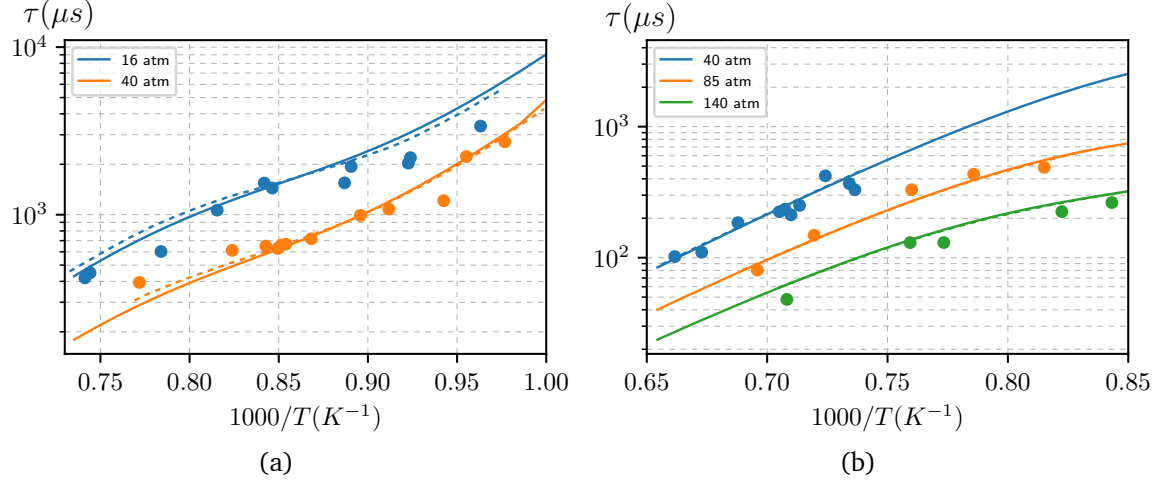


Figure 2.12: Ignition delays of a methane-oxygen-nitrogen mixture with a) stoichiometric conditions ($\phi = 1$) and b) $\phi = 3.0$ (20% CH_4 , 13.3% O_2 , 66.7% N_2) using mechanisms from Huang [21] and Petersen [48] respectively. Solid lines are from present study, dashed lines and symbols are computational and experimental data from the respective references.

With regards to the species molar concentration, $[\chi_k]$, Giovangigli found that using the ideal gas density (or molar volume) for the concentration leads to more accurate results than the real gas densities, when compared to the non-ideal ROP formulation. In this study, we use the ideal gas density in the expression for the species molar concentration

$$[\chi_k] = \frac{\rho X_k}{W} \quad (2.70)$$

2.5.2 Verification of kinetics - Ignition delay test

To verify the correctness of the chemistry routines in use, we use a constant-volume combustor with the ideal gas EOS to measure the ignition delay times. In this work, the ignition delay time (τ) is defined as the time of occurrence of the maximum pressure-rise rate. This is implemented in the code as the time at which the maximum of the normalized time-derivative of pressure occurs

$$\tau = \arg \max_t \left\{ \frac{1}{p} \frac{\partial p}{\partial t} \right\}. \quad (2.71)$$

For the following tests, we use the detailed, high-pressure CH_4 oxidation mechanisms from Huang [21] and Petersen [48]. The Huang [21] mechanism contains 38 species and 192 reactions, and is designed for high-pressure combustion. Figure 2.12 a shows the results from this test, performed at pressures of 16 and 40 atmospheres with a stoichiometric mixture of CH_4, O_2, N_2 with a O_2 in N_2 dilution ratio of 21%. The estimated ignition delays agree fairly well with the computational results in the reference.

The second test, presented in Figure 2.12 b, uses the NG1 CH_4 oxidation mechanism from Petersen [48]. This mechanism contains 118 species and 663 reactions, and is also designed for high-pressure combustion. The test is performed at pressures of 40,85 and 140 atmospheres with a fuel-rich mixture of CH_4, O_2, N_2 at an equivalence ratio $\phi = 3$ (20% CH_4 , 13.3% O_2 , 66.7% N_2). The present work shows excellent agreements with the computed ignition delay times published in the reference.

Chapter 3: Theory of laminar premixed flames and previous studies at elevated pressures

3.1 Structure of a canonical premixed flame

In premixed combustion, fuel and oxidizer are perfectly mixed at a molecular level prior to the process of burning. The region of maximal chemical reaction and heat release is concentrated in a thin region, called the flame region. The flame propagates through the unburnt fuel and oxidizer mixture, with a flame speed s_L , leaving behind the burnt products of combustion. The energy released in the process of conversion of reactants to products shows up in the burnt gas region as the adiabatic flame temperature T_{ad} .

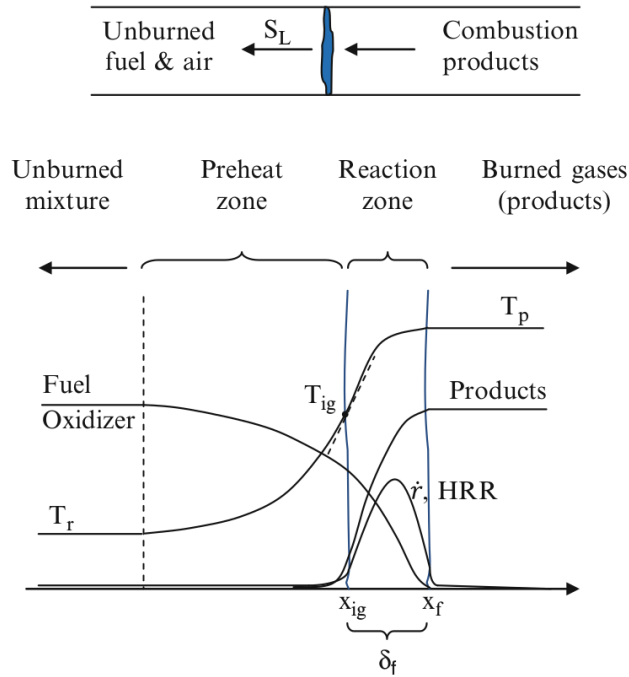


Figure 3.1: Structure of a laminar premixed flame. Figure from McAllister et al. [40]

The flame region can be considered to be comprised of two zones - the preheat zone and the reaction zone (Figure 3.1). Most of the chemical reactions and heat release occur in a thin region called the reaction zone. Heat released in the reaction zone diffuses into the unburnt mixture, thereby raising the temperature of the reactants. This region ahead of the reaction zone is the preheat zone, and the extent of it depends on the flame temperature, the thermal conductivity λ and heat capacity c_p of the unburnt mixture. The preheat zone is much larger than the reaction zone. The intermediate products formed as a result of the reaction diffuse into the preheat zone as a result of concentration gradients.

To simplify the computation of the flame, the reference frame is fixed to the flame front. So the flame itself is stationary, while the fuel and oxidizer mixture enters the inlet with a velocity equal to the flame speed s_L . The burnt gases leave the outlet with a velocity higher than the flame speed. This is due to the energy

released within the flame.

Equations 2.1 through 2.4 describe the physics of reacting flows. In the next section we consider a simplified analysis of a laminar premixed flame - the thermal theory of flame propagation.

3.2 Simplified analysis

3.2.1 Thermal theory of flame propagation

The thermal theory of flame propagation is originally due to Mallard and Le Chatelier [37]. They introduced the notions of the preheat zone and reaction zone, and postulated that the reaction zone begins at the point where the reactant temperature attains a certain value, termed as the ignition temperature. While the ignition temperature is not a measurable flame quantity, it identifies the regions having different opposing effects. Heat released from the reaction zone diffuses into the unburnt mixture, thereby raising the temperature of the reactants to the ignition temperature. Most of the chemical reactions driving the flame occur within the reaction zone, and any reactions in the preheat region are ignored. They only considered the problem of heat transport by conduction, and ignored any mass diffusion.

Assuming the flame has reached steady-state, the rate of change of enthalpy in the pre-heat zone is matched by the heat flux diffusing from the flame region into the pre-heat region

$$\int_{x_u}^{x_*} \frac{\partial(\rho u h)}{\partial x} dx = \int_{x_u}^{x_*} \frac{\partial}{\partial x} \left(\lambda \frac{\partial T}{\partial x} \right) dx. \quad (3.1)$$

where T_* is the ignition temperature at x_* in the flame.

We apply the fact that the mass flux is conserved throughout the flame, $\rho u = \rho_u S_L$, and the temperature gradient at the inlet is zero, $dT/dx|_u = 0$, leading to

$$\rho_u S_L (h_* - h_u) = \lambda_* \left. \frac{dT}{dx} \right|_* . \quad (3.2)$$

Approximating $dT/dx|_* \approx (T_b - T_*)/\delta_r$, where δ_r represents the reaction zone thickness, we get

$$\rho_u S_L (h_* - h_u) \approx \lambda_* \frac{T_b - T_*}{\delta_r} . \quad (3.3)$$

The expression for flame speed is

$$S_L \approx \frac{\lambda_* T_b - T_*}{\rho_u h_* - h_u} \frac{1}{\delta_r} . \quad (3.4)$$

The reaction zone thickness δ_r and ignition temperature T_* are not known at this point. To close this, we realize that the steady-state mass flux ρS_L must be matched by the mass rate of consumption, given by the chemical production rate $\dot{\omega}$ times the reaction zone thickness δ

$$\rho_u S_L \approx \dot{\omega} \delta_r . \quad (3.5)$$

Substituting δ_r back in the expression for flame speed, we get:

$$S_L \approx \left[\frac{\lambda_* T_b - T_*}{\rho_u h_* - h_u} \frac{\dot{\omega}}{\rho_u} \right]^{1/2} \quad (3.6)$$

The classical Mallard and Le Chatelier [37] expression for flame speed can be obtained by assuming a constant specific heat c_p and thermal conductivity λ

$$S_L \approx \left[\frac{\lambda}{\rho_u c_p} \frac{T_b - T_*}{T_* - T_u} \frac{\dot{\omega}}{\rho_u} \right]^{1/2} \quad (3.7)$$

While $(T_b - T_*)/(T_* - T_u)$ is still not known, we can see that the flame speed is

proportional to the thermophysical and kinetics properties as

$$S_L \sim \left[\frac{1}{\alpha} \frac{\dot{\omega}}{\rho_u} \right]^{1/2} \quad (3.8)$$

where $\alpha = \lambda/(\rho c_p)$ is the thermal diffusivity.

Linan and Williams' [31] review of Mikhelson's [43] work provided an alternative derivation for the thermal flame theory. Their expression for the total flame thickness is

$$\delta_L = \left(\frac{\lambda}{c_p} \frac{1}{\dot{\omega}} \right)^{1/2}. \quad (3.9)$$

The expression for flame speed is obtained using $\rho_u S_L = \dot{\omega} \delta_L$, to get

$$S_L = \left(\frac{\lambda}{\rho_u c_p} \frac{\dot{\omega}}{\rho_u} \right)^{1/2} \quad (3.10)$$

The flame speed expressions provided by Mallard and Le Chatelier [37] (Eqn. 3.7) and Mikhelson [43] (Eqn. 3.10) differ by the term $\sqrt{(T_b - T_*)/(T_* - T_u)}$, which remains indeterminable due to the unknown value of ignition temperature T_* . This term can also be expressed as the ratio of the total flame thickness δ_L to the reaction zone thickness δ_r . Linan and Williams [31] termed it the Zeldovich number Ze

$$\frac{\delta_L}{\delta_r} = Ze = \left(\frac{T_b - T_*}{T_* - T_u} \right)^{1/2}. \quad (3.11)$$

As Zeldovich number Ze approaches infinity, the reaction zone thickness is negligible for practical applications.

3.2.2 Theory of Zeldovich, Frank-Kamenetskii, and Semenov

Zeldovich and Frank-Kamenetskii [77] and Semenov [58] considered the problem introduced by the Mallard and Le Chatelier [37] theory, namely the

ignition temperature T_* . They used activation energy asymptotics to eliminate T_* from the thermal flame theory. This assumed that the ignition temperature is close to the burnt gas temperature. They found that they could replace

$$\left(\frac{T_b - T_*}{T_* - T_u}\right)^{1/2} = \frac{RT_b^2}{E_a(T_b - T_u)} \quad (3.12)$$

where E_a is the activation energy. This implies

$$Ze = \frac{\delta_L}{\delta_r} = \frac{RT_b^2}{E_a(T_b - T_u)} \quad (3.13)$$

Unlike the Mallard and Le Chatelier [37] theory, who only considered thermal diffusion, Zeldovich, Frank-Kamenetskii, and Semenov also consider the process of species diffusion to be important to the flame propagation. At first, they derive expressions for the case where the thermal diffusivity is matched by the species mass diffusivity

$$\alpha = \frac{\lambda}{\rho c_p} = D \quad (3.14)$$

which leads us to the definition of the non-dimension Lewis number Le , which is defined as the ratio of thermal diffusivity to mass diffusivity

$$Le = \frac{\alpha}{D} = \frac{\lambda}{D\rho c_p}. \quad (3.15)$$

With the Lewis number $Le = 1$ initially, they used the procedure of activation energy asymptotics to derive an expression for flame speed. A full treatment of this derivation can be found in Glassman et al. [12], Williams [74], and Law [29]. The expression for the flame speed of a one-step unimolecular reaction comes to

$$S_L = \left[\frac{2}{a_u} \frac{\lambda}{\rho c_p} (Z' e^{-E_a/RT_b}) \left(\frac{RT_b^2}{E_a(T_b - T_u)} \right) \right]^{1/2} \quad (3.16)$$

where Z' is the pre-exponential term in the Arrhenius expression ($\dot{\omega} = Z' e^{-E_a/RT_b}$) and a_u/p_u is the inlet mass fraction of the reactant.

3.3 Previous numerical studies of premixed flames using real gas EOS

3.3.1 Hydrogen flames

El-Gamal et al. [10] investigated the structure of planar laminar premixed $H_2 - air$ flames at high pressures (up to 100 MPa). This study used high-pressure thermodynamic and transport properties formulated in terms of molecular interaction parameters such as σ and ϵ , originally due to Saur [55]. . El-Gamal et al. [10] used non-ideal equilibrium coefficients K_p to capture the effect of high pressures on chemical equilibrium. The study used the $H_2 - air$ mechanism from Warnatz et al. [73].

All the flames considered in this study were computed with a fresh-gas temperature $T_u = 298K$. This study found that real gas effects start to become significant at ambient pressures exceeding 10 bar (Figure 3.2a). At 100 bar, the real gas flame speed is lower than the ideal gas equivalent by approximately 2%, while at 100 bar, the drop in real gas flame speeds is around 50%. The real gas models also lower the flame thicknesses at higher pressures (Figure 3.2b).

El-Gamal et al. [10] also studied the relative importance of the different real gas modifications. Figure 3.3 plots the relative deviation of flame speeds from the ideal gas flame speeds for each of the modification, and the net effect. They found that the effect of the real gas equation of state (curve A) was the most significant, closely followed by real gas transport properties (curve B). The real

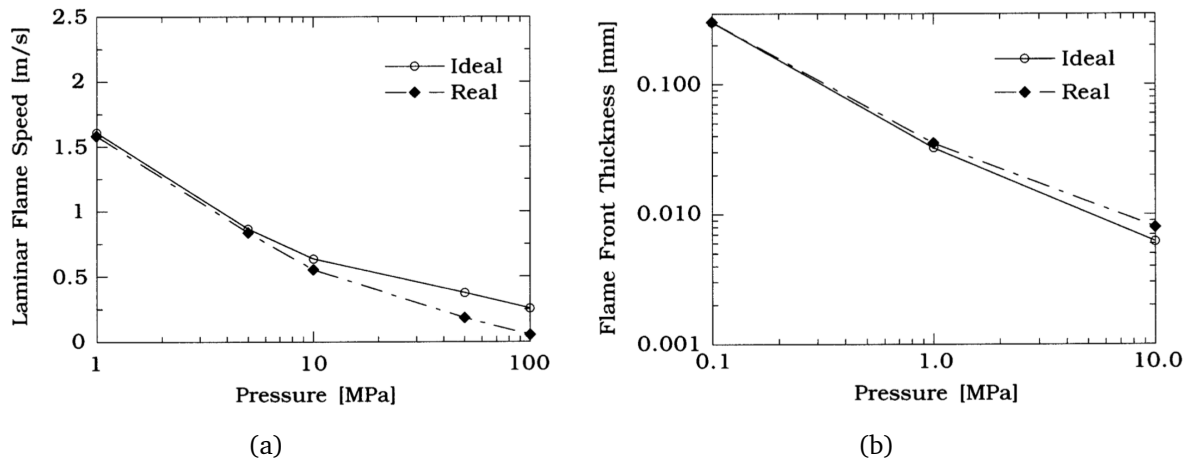


Figure 3.2: a) Flame speeds and b) flame thickness for ideal (—) and real (- - -) stoichiometric laminar premixed $H_2 - air$ flames as functions of pressure at a fresh gas temperature $T_u = 298K$. Figures from El-Gamal et al. [10].

gas modifications to the chemical kinetics (Curve C) was found to be of much less importance on relative terms.

El-Gamal et al. [10] was one of the first studies to explore high-pressure effects on planar laminar premixed flames and provided the relative significance of various real gas property modifications. This study, however, did not explore lower temperature regions where real gas effects are expected to be more significant.

Giovangigli et al. [11] studied the structure of transcritical laminar premixed $H_2 - air$ flames in greater detail. This study used the Soave-Redlich-Kwong (SRK) cubic equation of state to predict the thermodynamics of pure species. For unstable species, it used combination rules based on Lennard-Jones potential. This study used a multi-component mass diffusion model along with thermal diffusion (Soret) effects. They used the Chung et al. [8] correlation to estimate high-pressure transport coefficients. Like [10], this study used non-ideal chemical production rates to ensure non-negative entropy production. This study also used the $H_2 - air$ mechanism of Warnatz et al. [73], while noting the insufficiency of this mechanism

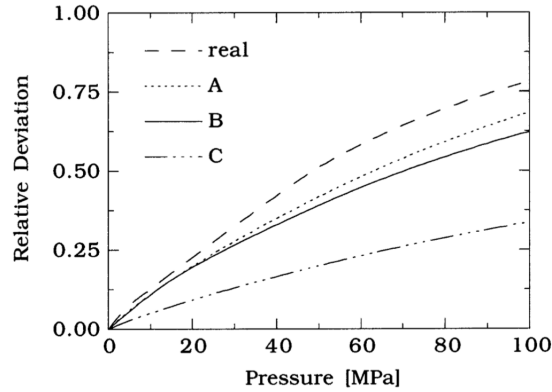


Figure 3.3: Relative deviation from ideal gas flame speeds for flame speeds with each of the individual modifications, Real gas equation of state (Curve A ·····), Real gas transport properties (Curve B —), Real gas chemical kinetics (Curve C - · - ·), and the net effect (- - -). Figure from El-Gamal et al. [10].

at high pressures.

Giovangigli et al. [11] reaffirmed the findings from [10] regarding the relative importance of the different real gas modifications. They too found that the real gas equation of state had the single largest effect on flame structure and propagation, and that non-idealities in the chemical kinetics had the least effect. Giovangigli et al. [11] found the effect of transport properties to be minimal, contrary to the findings from [10]. Giovangigli et al. [11] also found the non-ideal kinetics to be significant only at extremely high pressures (1000 *bar*).

Figure 3.4a shows the effect of the Soave-Redlich-Kwong equation of state on a stoichiometric $H_2 - air$ flame at $T_u = 100K$ and $p = 100bar$. The fresh-gas density shows the most significant effect of the real gas EOS. It can also be observed that the real gas post-flame temperature is reduced. This is expected due to the effect of the enhanced fresh-gas enthalpy. This will be further discussed in Chapter 5.

In Figure 3.4b, we see that the primary effect of including the thermal diffusion (Soret) effect is to enhance the diffusion of lighter of species towards the hotter zones, and heavier species towards the colder zones.

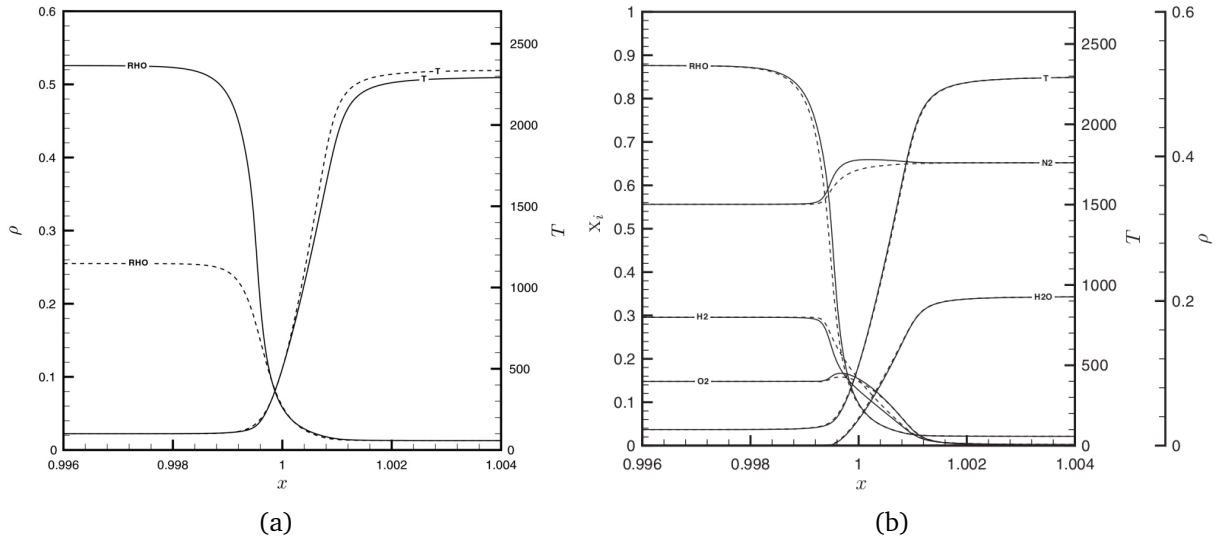


Figure 3.4: a) Effect of EOS and b) Effect of thermal diffusivity (Soret effect) on a stoichiometric laminar premixed $H_2 - air$ flame at for $T_u = 100K$ and $p = 100bar$. Profiles of density ρ (gcm^{-3}), temperature T (K), and species mole fractions X_i with real gas (—) and ideal gas (---) assumption. Figures from Giovangigli et al. [11].

Figure 3.5a shows the effect of the real gas thermal conductivity. The main effect is the enhanced diffusion of heat into the fresh-gas region, leading to smoother gradients in temperature and therefore density profiles. The effect on flame speeds was found to be minimal, nevertheless.

The effect of high-pressure mass diffusivities is shown in Figure 3.5b. The enhanced binary mass diffusivity is marked by the presence of more H_2O , HO_2 and H_2O_2 in the pre-heat region. Giovangigli et al. [11] found that the other species profiles remain largely unaffected, however.

3.3.2 Methane flames

Marchionni et al. [38] used the Redlich-Kwong equation of state to study real gas effects in $CH_4 - O_2$ premixed flames at pressures of up to $150 atm$. This study used low-pressure transport properties and real gas corrections to Arrhenius kinetics. It used the GRI-MECH 3.0 CH_4 oxidation mechanism [60]. All the

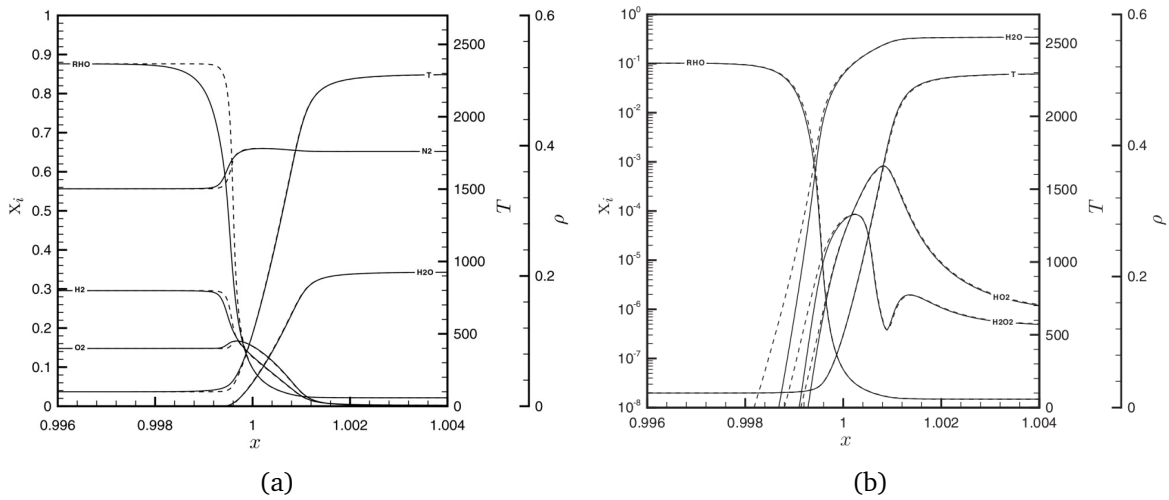


Figure 3.5: Effects of high-pressure a) thermal conductivity and b) binary mass diffusivity on a stoichiometric laminar premixed $H_2 - air$ flame at for $T_u = 100K$ and $p = 100bar$. Profiles of density ρ (gcm^{-3}), temperature T (K), and species mole fractions X_i with high-pressure (—) and low-pressure (- - -) coefficients. Figures from Giovangigli et al. [11].

computations were performed with a fresh-gas temperature of $298 K$.

Marchionni et al. [38] observe that deviations from ideal gas flame speeds increase with pressure. At a pressure of $150 atm$, the deviation in flame speeds is about 13% . They ascribe this difference to the pressure effect on specific heat capacity. They observe the maximum T deviation in the compressibility factor Z to be $\sim 2\%$, and the real gas density shows a correspondingly minimal difference.

Marchionni et al. [38] was the only study in our purview to compare their computational results with experimentally measured unstretched flame speeds for $CH_4 - O_2 - He$ mixture from Rozenchan et al. [54]. Two cases were compared, the first case at $40 atm$ with $17\% O_2 - 83\% He$ and the second case at $60 atm$ with $15\% O_2 - 85\% He$. The computations deviate from the measurements in both the rich and lean regions, but the real gas model captures the trends in flame speed better than the ideal gas model. The rest of the discrepancy is probably due to the low-pressure kinetics being used.

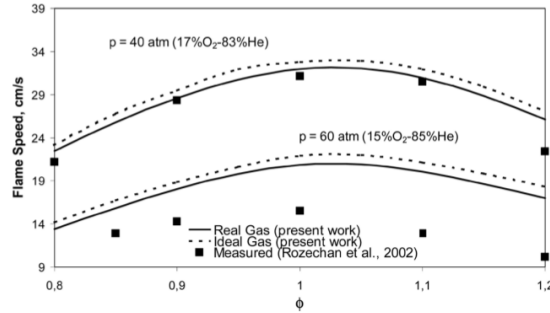


Figure 3.6: Flame speeds from computation via Marchionni et al. [38] (IG (- - -), RG (—)) and experimental results [54] (Symbols) for premixed $CH_4 - O_2 - He$ flames at 40 atm and 60 atm. Figure from [38].

While this study explored real gas effects on flames with varying equivalence ratios and pressures up to 150 atm, it used a fixed fresh-gas temperature of 298 K, and hence did not explore the thermodynamic state space where non-ideal effects are more significant. They found the real gas heat capacity to have the largest effect on flame speeds. We will show that this conclusion cannot be generalized for a real gas flame operating under significantly non-ideal conditions.

Ribert [53] computed flamelets for a laminar premixed $CH_4 - O_2$ flame using the Soave-Redlich-Kwong cubic equation of state. It used the Chung correlation [8] for high-pressure viscosities and thermal conductivities, and the high-pressure binary mass diffusivities were estimated using the Takahashi correlation [69]. Mixture-averaged transport model is used for mass diffusion. The study explored the parameter space in more detail compared to Marchionni et al. [38]. The focus of this study, however, was towards computing flamelets for use in turbulent combustion simulations.

Figure 3.7 shows the temperature variation in real gas flame speeds compared to the ideal gas equivalent at 75 bar. The difference in flame speeds is minimal at higher temperatures and exhibits the largest difference at lower temperatures. In addition, the variation of the real gas flame speed near the critical point is not

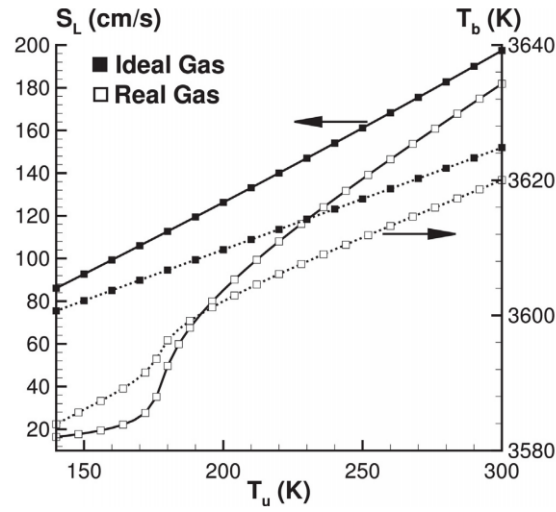


Figure 3.7: Computed laminar flame speeds S_L and flame temperatures T_b for premixed $CH_4 - O_2$ flames at 67 bar. Ribert et al. [53] assumes $Le_k = 1$ and low-pressure transport. Figure from [53].

linear, reflecting the non-linearity of the real gas thermodynamics. The effect of real gas enthalpy is also reflected in the adiabatic flame temperatures.

Chapter 4: Cantera-RealGas: steady-state solver

4.1 Shortcomings of the transient reacting flow solver

The simplest procedure for the computation of planar laminar premixed flames at steady-state involves time-evolving the set of unsteady, fully-compressible Navier-Stokes equations using explicit time-integration until the flame front and the flow field have reached steady state [52]. This also requires that flow controllers be employed to ensure that the inlet velocity matches the flame speed at steady-state. An alternative method is to assume that flow has reached steady-state, and solve the boundary value problem described by the steady-state, low-Mach formulation of the Navier-Stokes equations [62]. The Newton root-finding algorithm is typically used to solve such type of problems. Transient solvers have a much larger domain of convergence compared to Newton solvers, and the process of convergence in a transient solver is much less affected by the choice of initial conditions for the flow field. A Newton solver, however, is typically very sensitive to the choice of initial guesses, and is not expected to converge if the initial guess is not sufficiently close to the actual solution. Since combustion is a "stiff" problem, involving a wide range of length and time scales, an explicit time-integration scheme would need extremely small time steps to avoid numerical instability. On the other hand, Newton solvers are expected to converge quadratically when the provided guess is close to the solution.

At the beginning of this study, we opted for the development of the time-unsteady solver, as providing good initial guess with the real gas EOS was expected to be a bigger challenge than the longer solver runtime. The development and validation of this solver are detailed in the Appendix A. The transient solver was able to achieve reliable convergence over hundreds of premixed flames tested. However, the total time for computing a premixed flame, including the grid refinement process, turned out to be computationally prohibitive. While premixed flame solutions for simple chemical systems like $H_2 - O_2$ can converge within minutes of CPU time, even simpler hydrocarbons like CH_4 can take anywhere from several hours up to a few days depending upon the choice of equation of state and the transport properties in use. Despite MPI parallelization of the domain, and additional measures to accelerate the code, including local time stepping, the total solution time was larger than acceptable.

As fundamental studies of laminar premixed flames require parametric sweeps involving hundreds of flame computations, we made the decision to move away from the transient solver and port the previously implemented property estimation routines into the steady-state solver implemented in Cantera [14]. Cantera follows the hybrid approach where the Newton solver is coupled with an implicit time integration scheme to nudge the intermediate state into the domain of convergence of the Newton solver. The algorithm tries to solve the Newton solver with the given state, and upon failure solves the pseudo-transient problem for a fixed number of several steps, and this process is repeated until a converged solution is found. This is illustrated in the schematic in Figure 4.1.

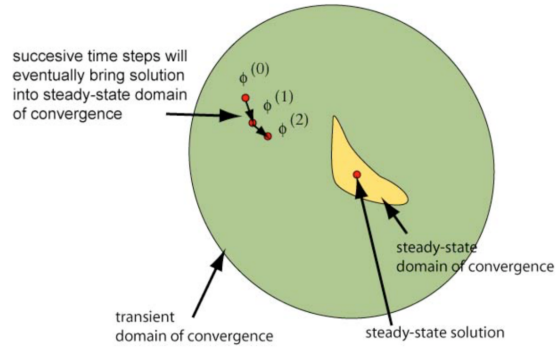


Figure 4.1: Illustration of the hybrid approach to computing laminar premixed flames. Figure by Goodwin [13].

4.2 Solver architecture

The overall architecture of the integration follows the schematic in Figure 4.2. The real gas property estimation routines originally developed for use with the transient solver is packaged interfaced with the hybrid steady-state/transient solver available in Cantera.

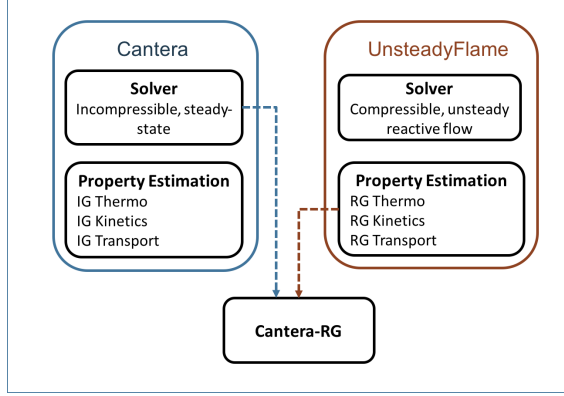


Figure 4.2: Schematic of Cantera integration.

4.3 Governing equations

We consider an unstretched, planar, freely-propagating flame in one dimension at steady-state. The following assumptions are used to simplify the set of governing equations used to compute the one-dimensional premixed flames:

1. At steady-state, the flame front is stationary and fixed to the laboratory frame of reference.
2. The Mach number is assumed to be small, and hence the pressure drop across the flame can be neglected. The viscous diffusion of momentum is assumed negligible due to the relatively small kinetic energy (cf. Williams [74]), and thus the momentum conservation equation is not solved.

The expressions are written out in terms of axial coordinate z in Eqn. 4.1.

$$\begin{aligned}
 \frac{\partial(\rho u)}{\partial z} &= 0, \\
 \rho u \frac{\partial Y_k}{\partial z} &= -\frac{\partial j_k}{\partial z} + \dot{\omega}_k, \quad k = 1 \dots N_s, \\
 \rho u c_p \frac{\partial T}{\partial z} &= \frac{\partial}{\partial z} \left(\lambda \frac{\partial T}{\partial z} \right) - \left(\sum_k c_{pk} j_k \right) \frac{\partial T}{\partial z} - \sum_k h_k W_k \dot{\omega}_k.
 \end{aligned} \tag{4.1}$$

The species diffusive mass flux j_k is estimated according to the mixture-averaged formulation and is given by

$$j_k = \rho D_k \frac{W_k}{W} \frac{\partial X_k}{\partial z} \quad (4.2)$$

where D_k is the mixture-averaged mass diffusivity of species k given by equation Eqn. 2.49

It is to be noted that enthalpy is a function of both temperature and pressure for a real gas, and hence the commonly used substitution $dh = c_p dT$ in the energy equation is valid only for an ideal gas in the context of the thermally-perfect gas assumption [23]. The assumption of constant pressure in the present study, however, means that $\partial h / \partial z = c_p \partial T / \partial z$, and hence the form of the convection and species diffusion terms in the energy equation in Eqn. 4.1 are valid under the assumptions made here.

4.4 Numerical method

As described earlier, the hybrid solver in Cantera is a combination of a steady-state Newton solver and implicit time-advancement.

4.4.1 Damped Newton method

Let us express the system of governing equations (Eqn. 4.1) by $\mathbf{F}(\Phi) = 0$, where the current state of the dynamical system at time i is given by Φ_i . If the subsequent state Φ^{i+1} is close enough to Φ^i , we can expand $\mathbf{F}(\Phi^{i+1})$ in Taylor series

around Φ^i , and neglect the higher order terms

$$\mathbf{F}(\Phi^{i+1}) \simeq \mathbf{F}(\Phi^i) + \sum_{j=1}^N \left. \frac{\partial \mathbf{F}(\Phi)}{\partial \Phi_j} \right|_{\Phi=\Phi^i} (\Phi_j^{i+1} - \Phi_j^i). \quad (4.3)$$

This can be rewritten as

$$\mathbf{F}(\Phi^{i+1}) = \mathbf{F}(\Phi^i) + \mathbf{J}_j^i (\Phi_j^{i+1} - \Phi_j^i) \quad (4.4)$$

where \mathbf{J} is the Jacobian. Knowing the current state, and the ability to estimate the Jacobian at the current state, the next state can be approximated by

$$\Phi_j^{i+1} = \Phi_j^i - [\mathbf{J}_j^i]^{-1} \mathbf{F}(\Phi^i) \quad (4.5)$$

This resembles the standard Newton root-finding formula and the solution to $\mathbf{F}(\Phi^{i+1}) = 0$ is found by iterating the above expression until a predefined convergence criterion is met. Cantera's implementation of the Newton solver uses the step-norm criterion

$$\|\Phi_j^{i+1} - \Phi_j^i\| \leq \epsilon_{rel} \|\Phi_j^{i+1}\| + \epsilon_{abs}, \quad (4.6)$$

where ϵ_{rel} and ϵ_{abs} are the relative and absolute error tolerances respectively. The Newton-Raphson method converges quadratically when close to the root, however, convergence is not guaranteed if the initial guess is located far from the root.

The chief computational complexity of this method is due to the need to estimate and invert the Jacobian during every iteration. An analytical estimation of the Jacobian is not possible, and it is instead computed by the method of finite differences. This will be explained in the next subsection. To estimate the inverse of the Jacobian, the method of LU factorization is used.

If the magnitude of the current Newton step $[\mathbf{J}_j^i]^{-1} \mathbf{F}(\Phi^i)$ is too large, it can

lead to

$$\|F(\Phi_j^{i+1})\| > \|F(\Phi_j^i)\|, \quad (4.7)$$

which implies the iteration has overshoot the root. To prevent overshooting, a damping coefficient λ can be used to find the maximum step length that also avoids overshoots. This is known as the damped Newton method and is expressed as

$$\Phi_j^{i+1} = \Phi_j^i - \lambda[\mathbf{J}_j^i]^{-1}\mathbf{F}(\Phi_j^i). \quad (4.8)$$

The damping coefficient λ is an unknown quantity and needs to be determined as part of the method. At the start, a damping coefficient of unity is used, resembling the conventional Newton algorithm. After the first step, if $\|F(\Phi_j^{i+1})\| \leq \|F(\Phi_j^i)\|$, then the new iterate Φ_j^{i+1} is accepted and the algorithm continues. If $\|F(\Phi_j^{i+1})\| > \|F(\Phi_j^i)\|$, then the value of the damping coefficient is reduced by a factor of $\sqrt{2}$ and the process is repeated again. The damped Newton method enhances the domain of convergence of the original Newton algorithm.

4.4.2 Pseudo time-stepping

If the damped Newton algorithm fails, then the hybrid solver attempts an implicit time-evolution for a fixed number of iterations. This implicit time-stepping scheme is constructed by adding time-dependent terms to the conservation equations solved by the steady-state solver.

$$\begin{aligned} \frac{\partial \Phi}{\partial t} &= \mathbf{F}(\Phi) \\ \mathbf{F}(\Phi^{i+1}) - \frac{\Phi_j^{i+1} - \Phi_j^i}{\Delta t} &= 0 \end{aligned} \quad (4.9)$$

The above implicit expression can be re-expressed as

$$\mathbf{F}(\Phi^i) + \mathbf{J}_j^i (\Phi_j^{i+1} - \Phi_j^i) - \frac{\Phi_j^{i+1} - \Phi_j^i}{\Delta t} = 0, \quad (4.10)$$

which simplifies to

$$\left(\mathbf{J}_j^i - \mathbf{I}/\Delta t\right) (\Phi_j^{i+1} - \Phi_j^i) = -\mathbf{F}(\Phi^i), \quad (4.11)$$

where \mathbf{I} is the identity matrix. The effective Jacobian in the time-evolution case, $\mathbf{J}_j^i - \mathbf{I}/\Delta t$, is the same as the steady-state case except for the diagonal entries. Due to the addition of the time-dependent terms, the convergence is less sensitive to the choice of initial conditions.

4.5 Spatial discretization

Cantera uses a simple first-order upwind scheme for convective terms. The spatial derivative of any arbitrary convective term f at the j th index is expressed as:

$$\begin{aligned} \left(\frac{\partial f}{\partial z}\right)_j &= \frac{f_j - f_{j-1}}{z_j - z_{j-1}} & u_j > 0 \\ \left(\frac{\partial f}{\partial z}\right)_j &= \frac{f_{j+1} - f_j}{z_{j+1} - z_j} & u_j \leq 0 \end{aligned} \quad (4.12)$$

Cantera treats diffusive terms with a second-order central difference scheme. The heat flux term in the energy equation is discretized as:

$$\left[\frac{d}{dz} \left(\lambda \frac{dT}{dz}\right)\right]_j = \frac{2}{z_{j+1} - z_{j-1}} \left(\frac{\lambda_{j-1}(T_j - T_{j-1})}{z_j - z_{j-1}} - \frac{\lambda_j(T_{j+1} - T_j)}{z_{j+1} - z_j} \right) \quad (4.13)$$

The Jacobians necessary for the Newton solver are approximated with a finite

difference formula. For example, the Jacobian \mathbf{J}_j^i is

$$\mathbf{J}_j^i = \frac{\partial \mathbf{F}(\Phi)}{\partial \Phi_j} \simeq \frac{\mathbf{F}(\Phi_j + \Delta \Phi_j) - \mathbf{F}(\Phi_j)}{\Delta \Phi_j} \quad (4.14)$$

4.6 Boundary and initial conditions

The governing equations represented by Eqn. 4.1 constitutes a boundary value problem. At the inlet boundary, the temperature T_u , species mass fractions $Y_{k,u}$, and mass flow rate $\dot{m}_u = \rho_u u_u$ are required to be specified. To account for the upstream diffusion of some species into the inlet, the inlet composition cannot be fixed but should account for the mass diffusion at the inlet [27]. This results in the expressions

$$\begin{aligned} T(z_0) &= T_u \\ \dot{m}_u Y_{k,u} - j_k(z_0) &= \rho(z_0) u(z_0) Y_k(z_0) \\ \rho(z_0) u(z_0) &= \dot{m}_u \end{aligned} \quad (4.15)$$

At the outlet boundary, Neumann boundary conditions on axial velocity, temperature and species mass fraction are applied.

$$\left. \frac{\partial u}{\partial z} \right|_{z_N} = 0, \quad \left. \frac{\partial T}{\partial z} \right|_{z_N} = 0, \quad \left. \frac{\partial Y_k}{\partial z} \right|_{z_N} = 0 \quad (4.16)$$

We also need an estimated value for the outlet temperature (T_b), density (ρ_b) and axial velocity (u_b) in order to set the initial flame profile. The outlet temperature is determined by equilibrating a constant enthalpy-pressure reactor in Cantera, and picking the value of the equilibrated temperature. With this value

of the final temperature (T_b), an estimated outlet density (ρ_b) can be obtained. Applying the mass conservation at inlet and outlets, the outlet velocity can be obtained as

$$u_b = \rho_u u_u / \rho_b \quad (4.17)$$

To obtain axial profiles of the initial conditions from the boundary conditions, a hyperbolic tangent blending function is used to smoothly interpolate from the inlet values of density, temperature, velocity, species compositions to the respective outlet values. The blending function requires the position and an initial flame width, both of which are specified in the input file.

4.7 Computational grids

Discretization errors affect the flame speeds computed. Discretization errors behave like numerical dissipation enhancing the physical diffusion process and artificially causing a higher flame speed than is physical. To obtain flame computations independent of the resolution of the grid, the computational grid must be sufficiently resolved.

4.7.1 Adaptive refinement

The classic approach to grid refinement is to have sufficiently small grid-spacing everywhere in the grid. However, this approach is not computationally efficient as computational time scales super-linearly with the number of grid points. To minimize computational complexity while ensuring grid-independent solutions, we need only refine the grid in the region of strongly varying physical quantities around the flame front.

The second problem is that starting computations with a sufficiently resolved grid would take the high-frequency errors a long time to leave the domain. Instead, it is efficient to start with a highly-dissipative coarse grid by which the highest frequency errors will quickly dissipate. After this more grid points are successively added to the regions requiring refinement until grid independence is achieved.

Cantera uses an adaptive grid refinement process to refine the grid near the flame front. The refinement algorithm employs the following user-defined parameters;

- Ratio: Specifies the maximum ratio of consecutive grid spacings.
- Slope: Maximum fractional change in the value of each solution component between adjacent grid points
- Curve: Maximum fractional change in the derivative of each solution component between adjacent grid points
- Prune: Threshold for removing unnecessary grid points.

A sample grid refinement for the case with ratio=2.0, slope=0.01, and curve=0.01 is shown in Figure 4.3.

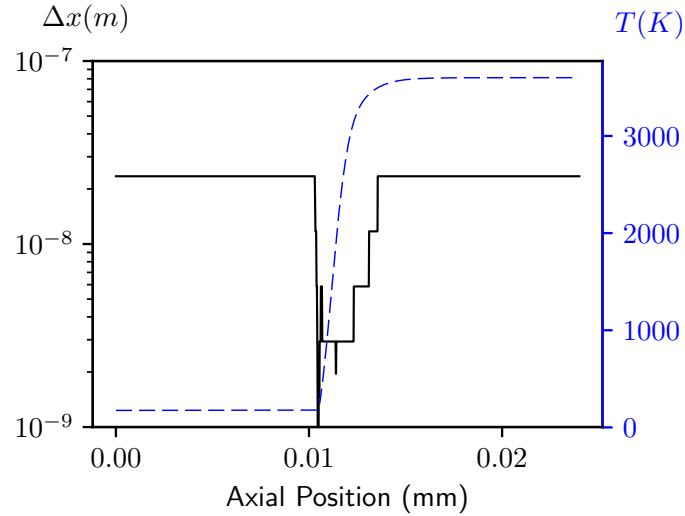


Figure 4.3: Sample stretched grid with ratio=2.0, slope=0.01, curve=0.01, prune=-0.1.

4.8 Data input and pre-processing

The solver accepts data for an arbitrary number of species. To perform all the necessary property estimation, the solver requires the following input data:

- Critical thermodynamic data (T_c , p_c , V_c) and acentric factors (ω) for every species
- Lennard-Jones or Stockmeyer potential well parameters (σ , ϵ).
- NASA polynomial coefficients ($a_0..a_6$ in Eqn. 2.34)
- Arrhenius rate coefficients for each elementary reaction.
- Miscellaneous species data (Molecular weights, Dipole moments)

To enhance the computational efficiency of the property estimation routines, certain intensive properties like the collision integral Ω_v (Eqn. 2.43) are computed for an interval of temperatures during the pre-processing step, and made available

to the time-advancement section of the code through a curve fit that is cost-effective to compute at runtime.

4.9 Validation of premixed flames at low pressures

To validate the implementation of the integrated steady-solver, laminar premixed $H_2 - O_2 - Ar$ flames are computed at a range of fresh-gas temperatures, ambient pressures, and equivalence ratios. The Burke high-pressure hydrogen oxidation mechanism [4] is used as the chemistry set. Figure 4.4 shows the laminar flame speeds from the ideal gas EOS and Peng-Robinson simulations, alongside results from CHEMKIN [26]. The low-pressure flame speeds using ideal gas and Peng-Robinson agree well with the CHEMKIN reference values for the parametric variations in T_u and ϕ . For variable pressure case, the ideal gas flame speeds match favorably with CHEMKIN. However, the real gas flame speeds are lower than the ideal gas values with increasing ambient pressures. In the next chapter, we will discuss why this makes physical sense.

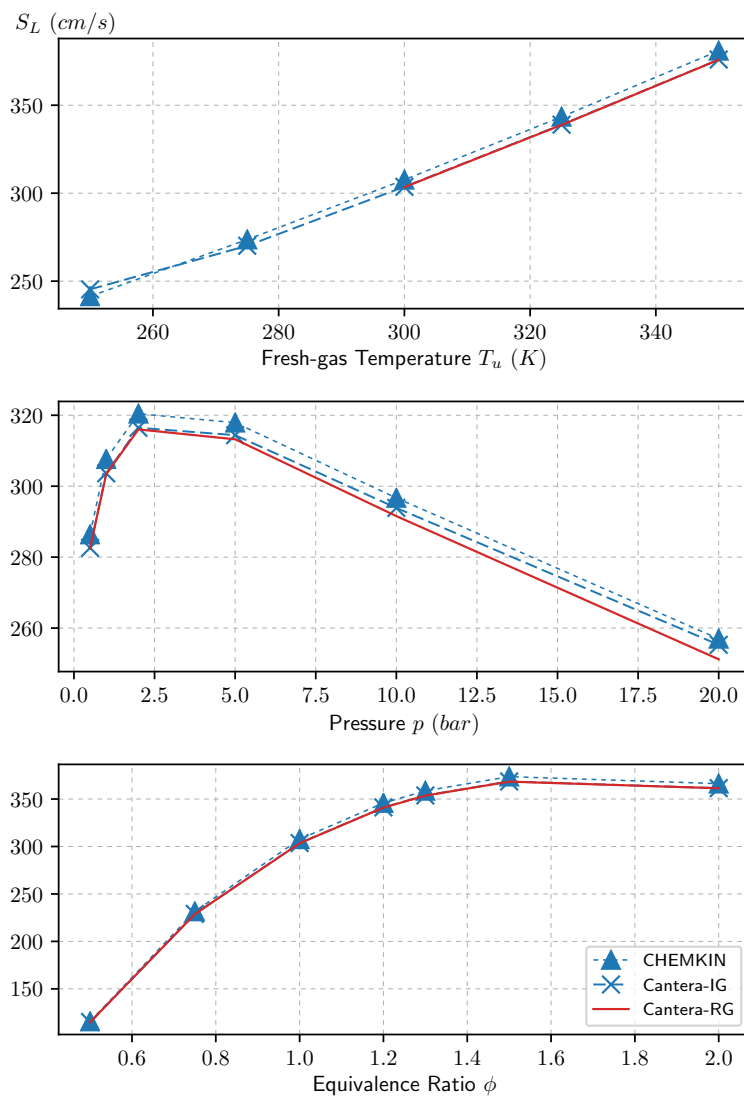


Figure 4.4: Laminar flame speeds for $H_2 - O_2 - Ar$ mixtures at a range of a) Fresh-gas temperatures b) Ambient pressures and c) Equivalence ratios using ideal gas (Blue Crosses), Peng-Robinson (Red solid line), and CHEMKIN ideal gas reference (Triangles). Computations default to $p = 1 \text{ bar}$, $T_u = 300K$ and $\phi = 1.0$, unless otherwise specified.

4.10 Verification of grid convergence

An important step in the process of verification is to ensure the computed flame is independent of the choice of grids used. Numerical dissipation errors artificially enhance the computed values of flame speed over the true flame speed, and it is important that the grids be sufficiently refined. Since a first-order upwind scheme has been used to discretize the convective terms, the errors in flame speed and other flame quantities are also expected to go down linearly as the grid spacing Δx is reduced, or as inverse function of the number of grid points N .

$$\begin{aligned} S_{L,observed} &\approx S_{L,true} + C_1 \Delta x \\ S_{L,observed} &\approx S_{L,true} + C_2/N \end{aligned} \tag{4.18}$$

In Figure 4.5, we plot the computed flame speeds for stoichiometric premixed $CH_4 - O_2$ flames, at 75 bar, 170 K using the Peng-Robinson EOS, for a series of successively refined grids with uniform spacing. We also fit Eqn. 4.18 to the observed flame speeds and see that it follows the first-order trends well. In addition, we are able to estimate the asymptotic value of the observed flame speed as $N \rightarrow \infty$, which is essentially the true flame speed. The stretched grid used in the results presented in the later sections is also plotted. The absolute error between the flame speed with the stretched grid and the estimated true flame speed is less than 0.06%.

For a more rigorous estimation of errors in the grid-refinement process, we need a measure for the axial profile of the quantities and not just the flame speeds. We define an error norm for an arbitrary discrete function f on a grid with variable

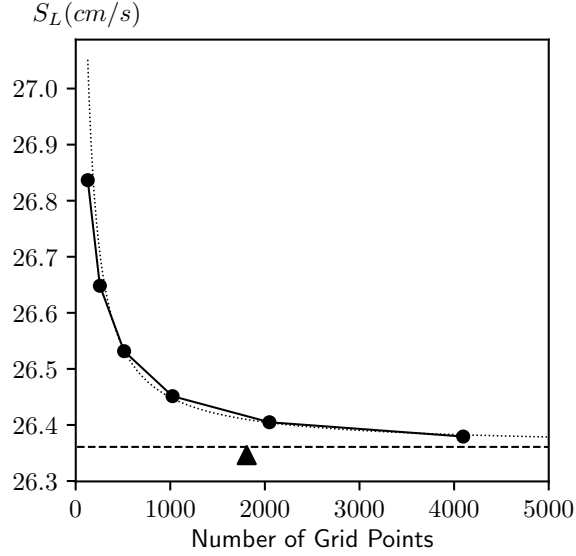


Figure 4.5: Computed laminar flame speeds with uniform grids (—●—) and stretched grid (▲), non-linear least squares fit of Eqn. 4.18 (·····), and the estimated true flame speed (---) for a premixed $CH_4 - O_2$ flame at 75 bar, $T_u = 170K$, $Le_k = 1$ using Peng-Robinson EOS.

grid spacing Δx_i as

$$\|f^c - f^{ref}\|_2 = \sqrt{\frac{1}{L} \sum_{i=1}^{N_c} (f^c(x_i^c) - f^{ref}(x_i^c))^2 \Delta x_i^c}, \quad (4.19)$$

where L is the length of the domain, expressed as

$$L = \sum_{i=1}^{N_c} \Delta x_i^c,$$

and superscripts c and ref denote that the quantities are from the coarse grid and reference grid respectively.

Since the flame position differs between different computations, we normalize the flame coordinates using the axial coordinate at which the flame temperature crosses 1000 K. The L_2 norm of the absolute error in the quantities of interest (u, T, Y_{CO}) is plotted as a function of average grid spacing (Figure 4.6). The absolute error is measured with respect to the reference solution from a 4096-point uniform grid. First-order convergence behavior is realized for the quantities of

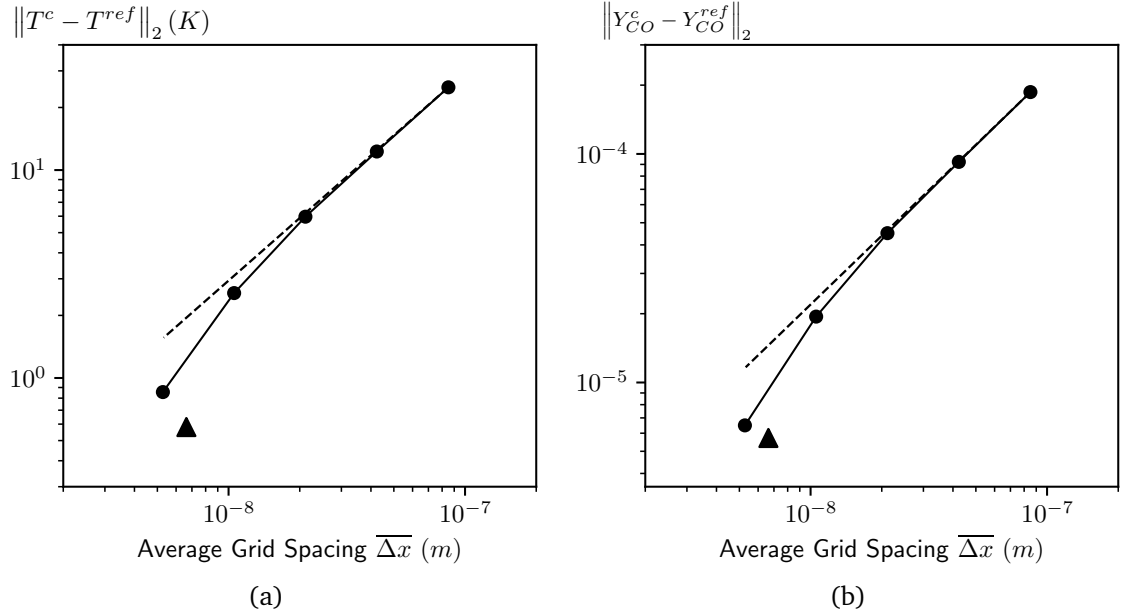


Figure 4.6: Estimated error norms for temperature T , and CO mass fraction with uniform grids (—●—) and stretched grid (▲) for a premixed $CH_4 - O_2$ flame at 75 bar , $T_u = 170K$, $Le_k = 1$ using Peng-Robinson EOS. Dashed line (- - -) represents first-order convergence.

interest. In addition, the error in stretched-grid flame computations also converge at the same rate. The stretched grid computation incurs an absolute error of $\sim 0.6K$ in a temperature profile that reaches beyond $3000K$. Similarly, the absolute error in Y_{CO} is 6×10^{-6} , which is negligible compared to peak CO mass fractions of ~ 0.2 . We find this margin of error acceptable for the purposes of this study and use similar levels of grid refinement for the computations presented in this work.

4.11 Validation of premixed flames at elevated pressures

4.11.1 $CH_4 - O_2 - He$ flames - validation with experiment and computation

Experimental data on unstretched laminar premixed flames at high pressures is scarce. There have been methods developed to extract laminar flame speeds from experimental data by systematically correcting for the effects of flame stretch. This method, however, fails at high pressures due to the presence of other modes

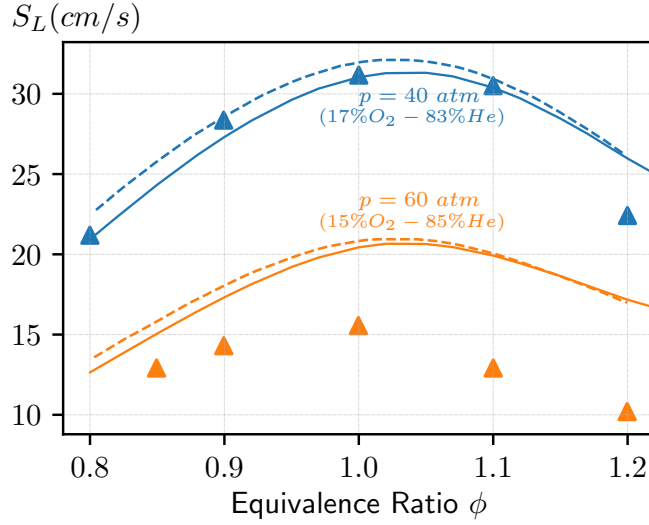


Figure 4.7: Experimentally observed (\blacktriangle - Rozenchan et al. [54]) and computed (—- Present Study, - - - [38]) laminar flame speeds for $CH_4 - O_2 - He$ mixtures at a) (17% $O_2 - 83\%He$) at 40 atm and b) (15% $O_2 - 85\%He$) at 60 atm for a range of equivalence ratios.

of instabilities which cannot be corrected for. Rozenchan et al. [54] developed a windowed, dual-chambered bomb apparatus to study high-pressure combustion phenomena $CH_4 - air$ mixtures up to 60 atm. Helium is used as diluent instead of Nitrogen so as to delay the onset of instabilities. Beyond this maximum pressure, however, flame instabilities mark their onset with the formation of flame cells.

Rozenchan et al. [54] published the corrected laminar flame speeds of $CH_4 - O_2 - He$ premixed flames at pressures of 40 and 60 atm. Figure 4.7 compares the results from the present study with experimental results from Rozenchan et al. [54]. In addition, we also compare with the numerical results from [38]. Both sets of computations used the GRI-MECH 3.0 CH_4 oxidation mechanism [60]. The computational results from the present study compare favorably with the numerical reference [38], and even the experimental results at lower values of pressure. However, both the present study and Marchionni et al. [38] show a wide discrepancy with the observed flame speeds at high equivalence ratios, especially for the 60 bar case. This is likely a consequence of using the GRI-MECH 3.0 mechanism, which does not model the reactions at high pressures accurately.

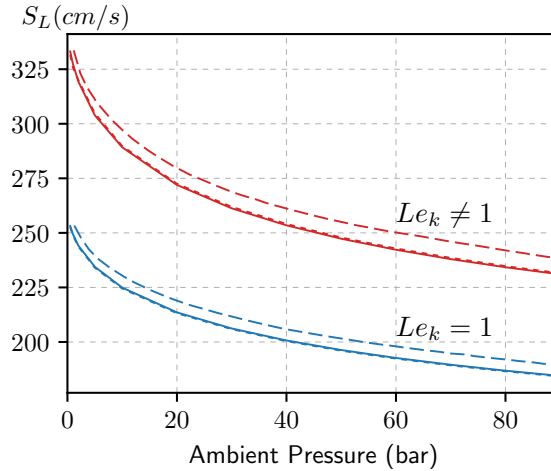


Figure 4.8: Laminar flame speeds of stoichiometric premixed $CH_4 - O_2$ mixtures using the ideal gas law with the present work (—), Ribert [53] (---) and Chemkin reference [26] (.....) at unity-Lewis number (Blue) and variable-Lewis numbers (Red). Fresh-gas temperature is 300K, and the mechanism used is due to Lindstedt [32].

4.11.2 $CH_4 - O_2$ flames - validation with computations

We compare the results from our real gas implementation with the computed laminar premixed $CH_4 - O_2$ flame speeds from Ribert et al. [53]. We check the implementations of both the Peng-Robinson and Soave-Redlich-Kwong EOS with the reference flame speeds which used SRK EOS. For high-pressure transport property estimation, both studies use the Chung correlation for thermal conductivities, and Takahashi correlation for mixture-averaged mass diffusivities. Both studies use the CH_4 oxidation mechanism from Lindstedt [32] [24], containing 29 species, 141 reactions.

First, we check the results of ideal gas flame computations with Ribert et al. [53] and CHEMKIN [26] in Figure 4.8. Our solver shows good agreement with CHEMKIN for both variable and unity Lewis number cases, while having slightly lower flame speeds compared to Ribert et al. [53].

In Figure 4.9, we validate our implementation of the real gas equation of states, at a pressure of 67 bar, assuming unity Lewis number and low-pressure

transport. The results from our Peng-Robinson and Soave-Redlich-Kwong implementation show good agreement with the SRK EOS implementation in Ribert et al. [53]. The real gas laminar flame speeds have a stronger dependence on temperature compared to the ideal gas, and vary non-linearly around the reactant mixture's critical point. At 140 K, the real gas S_L is smaller than the ideal gas S_L by a factor of about 5. The variations in the real gas flame temperatures T_b are much less pronounced, but also exhibit non-linearity near the critical point due to the non-linear variation of caloric properties (c_p , h , e) in the vicinity of the critical point.

The flame temperature T_b , which shows the best agreement with the reference, largely depends on the thermodynamic properties estimated in the pre-flame and post-flame regions. Hence, the better agreement of flame temperatures implies that the real gas thermodynamics are correct. The flame speeds, however, depend also on the transport properties and to a larger extent on the computational grid. The computational results presented in this study are adaptively refined near the flame region, and use 1600 – 2300 grid points across the flame front. The extremely fine grids used in this study ensure that the effects of numerical errors are limited. The results from the present study's Peng-Robinson implementation also show good agreement with the other real gas EOS implementations.

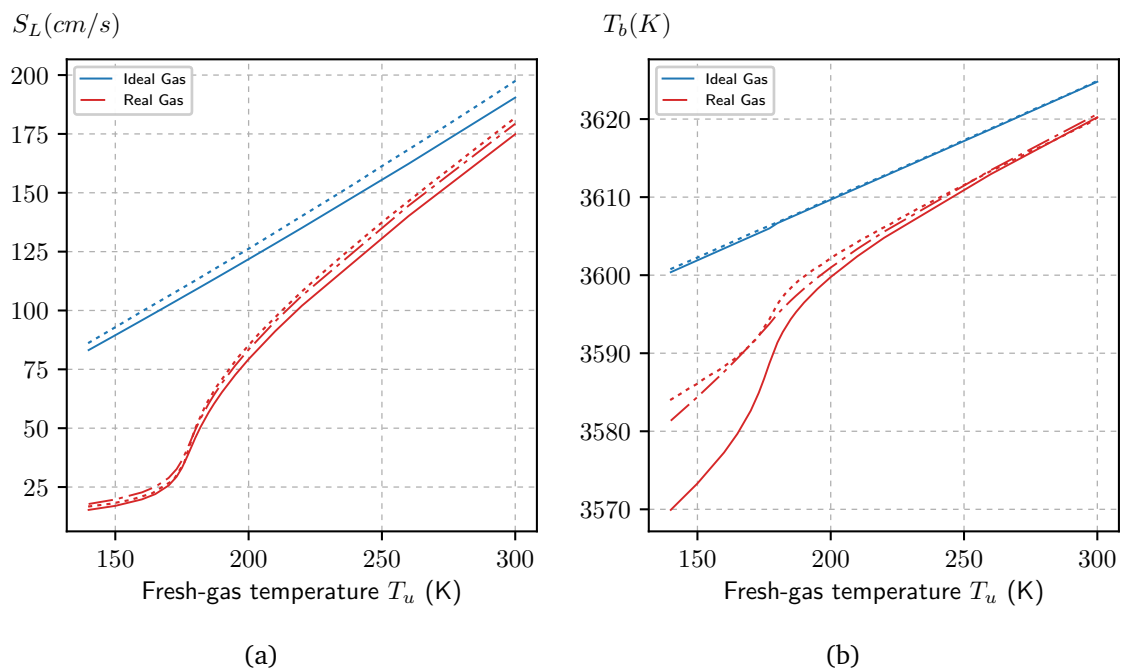


Figure 4.9: Comparison of a) laminar flame speeds b) flame temperatures of stoichiometric premixed $CH_4 - O_2$ mixtures at 67 bar using the ideal gas (Blue) and real gas (Red) equations of state with the present work (IG,PR —, SRK - · - ·), Ribert [53] (- - -). Assumes low-pressure transport and $Le_k = 1$. Mechanism from Lindstedt [32].

Chapter 5: Real gas effects in high-pressure laminar $CH_4 - O_2$ premixed flames

We present the results from numerical studies of transcritical laminar $CH_4 - O_2$ premixed flames. The first section explores the effects of the real gas equation of state with the assumption of low-pressure transport, followed by the contributions of high-pressure transport properties, and lastly, the effects of several high-pressure methane oxidation mechanisms are studied.

5.1 Effect of real gas thermodynamic models

We first assess the effects of the Peng-Robinson equation of state on a $CH_4 - O_2$ flame at unity Lewis number with low-pressure transport. The CH_4 oxidation mechanism used in this study is from Lindstedt [32], containing 29 species and 141 reactions. This is consistent with the mechanism used in [53].

5.1.1 Structure of a transcritical laminar $CH_4 - O_2$ premixed flame at $Le = 1$

Figure 5.1 plots the structure of a laminar premixed $CH_4 - O_2$ flame at a pressure of 75 bar and unburnt temperature of 170 K. Under such conditions, the reactant mixture exhibits a significant level of non-ideality. The most apparent effect of the real gas equation of state is the significantly enhanced mixture density

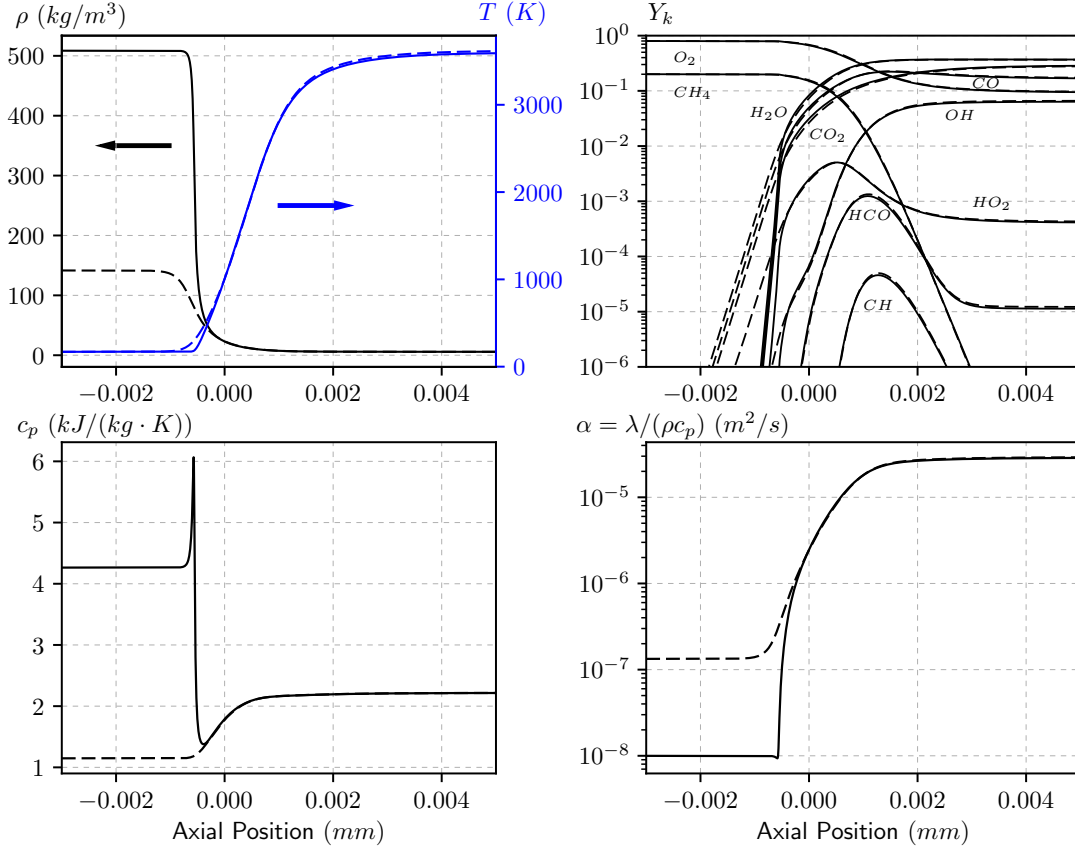


Figure 5.1: Profiles of mixture density ρ , temperature T , species mass fractions Y_k , specific heat capacity c_p , and thermal diffusivity α_{th} for a transcritical premixed $CH_4 - O_2$ flame at 75 bar, $T_u = 170K$, $Le_k = 1$ with Peng-Robinson (—) and ideal gas (---) EOS.

ρ and heat capacity c_p compared to their corresponding ideal gas profiles in the unburnt and pre-heat zones. This is to be expected since the inflow condition of the reactants was chosen to be near the critical points of CH_4 ($T_c = 190 K$, $p_c = 46 bar$) and O_2 ($T_c = 155 K$, $p_c = 50 bar$). It is also clear that flame quantities exhibit real gas effects in the fresh-gas and pre-flame regions only until a certain temperature threshold ($\simeq 500 K$), after which the real gas mixture density, thermal diffusivity, heat capacity, and species mole fractions regain their ideal gas behavior. This is consistent with the theory of corresponding states, as the compressibility factor Z tends to unity at high temperatures regardless of pressure levels. The real gas post-flame temperature is lower than the corresponding ideal gas value due to the lowered real gas reactant enthalpy and consequently smaller conversion of

chemical energy into thermal energy.

The real gas flame exhibits a less diffuse temperature profile, with a smaller pre-heat region compared to the ideal gas flame. This is due to the drastically reduced thermal diffusivity ($\alpha = \lambda / (\rho c_p)$) in the pre-flame region. In this section, we only modify the EOS leaving the transport properties at their low-pressure values. Hence the thermal conductivity can be considered to be approximately the same in both cases. The enhanced reactant density and heat capacity lower the thermal diffusivity by an order of magnitude, leading to a sharper transition in the temperature profile. With the assumption of unity Lewis number, the mass diffusion coefficients are also correspondingly reduced leading to a sharper rise in the composition of reaction intermediates and products in the pre-heat region. Figure 5.1 shows the delayed rise in the production of major products H_2O and CO_2 , and also minor products such as CO , OH and HO_2 . Despite the reduction in the thermal and mass diffusion layer thickness, it is important to note that the thickness of the real gas flame's inner layer does not show much of a deviation from its ideal gas value.

5.1.2 Energy production and transport

To better understand the underlying flame physics, we revisit the energy equation as the balance between the convective transport of heat \dot{Q}_{conv} , the diffusion of heat due to the prevailing temperature gradient \dot{Q}_{cond} , the transport of chemical energy due to species mass diffusion \dot{Q}_{diff} and most importantly, the conversion of chemical energy to thermal energy \dot{Q}_{src} .

$$\underbrace{\rho u c_p \frac{\partial T}{\partial z}}_{\dot{Q}_{conv}} = \underbrace{\frac{\partial}{\partial z} \left(\lambda \frac{\partial T}{\partial z} \right)}_{\dot{Q}_{cond}} - \underbrace{\left(\sum_k C_{pk} j_k \right) \frac{\partial T}{\partial z}}_{\dot{Q}_{diff}} - \underbrace{\sum_k h_k W_k \dot{\omega}_k}_{\dot{Q}_{src}} \quad (5.1)$$

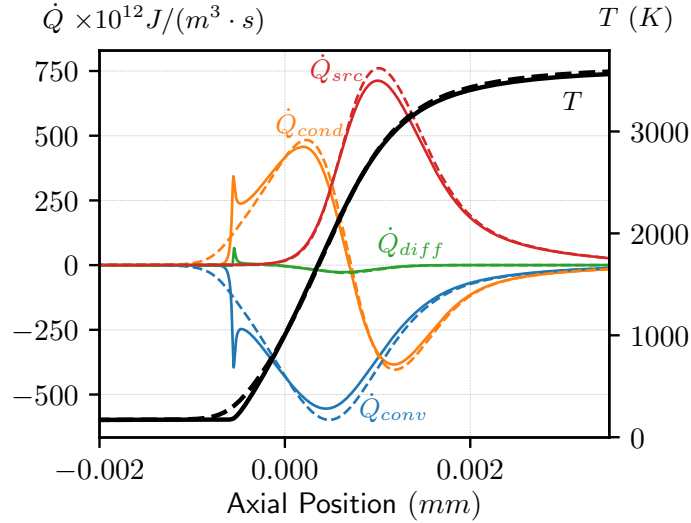


Figure 5.2: Fluxes of heat release rates through convection \dot{Q}_{conv} , the conduction \dot{Q}_{cond} , species mass diffusion \dot{Q}_{diff} , and chemical reaction \dot{Q}_{src} for a transcritical premixed $CH_4 - O_2$ flame at 75 bar, $T_u = 170K$, $Le_k = 1$ with Peng-Robinson (—) and ideal gas (- - -) EOS.

Figure 5.2 plots the energy budgets of the transcritical flame from the previous section (75 bar, $T_u = 170K$). Firstly, we observe that the real gas flame exhibits lowered peak heat release and consequently diminished heat transfer rates. Since the peak of chemical heat release \dot{Q}_{src} lies at a temperature $\sim 3000K$, the flame region itself is close to ideal. The real-gas effects from the fresh-gas and pre-heat region, however, affect the heat release in the flame region. As discussed in the previous section, the lowered reactant enthalpy leads to a lowering of the adiabatic flame temperatures. This consequently lowers not only the species production rate $\dot{\omega}_k$, but also the values of the product enthalpies. The combined effect leads to lower chemical heat release rates in the flame region for the real gas case.

The ideal gas flux profiles of heat conduction \dot{Q}_{cond} , and convection \dot{Q}_{conv} are smooth and monotonic in the pre-heat region. In contrast, we see that the corresponding profiles for real gas are marked by a sharp jump in heat transfer rates, corresponding to the point in the flame where the real gas heat capacity peaks. In the pre-heat region, the values of the profiles are determined by the balance between \dot{Q}_{cond} , \dot{Q}_{conv} , and to a much lesser extent, \dot{Q}_{diff} . By definition,

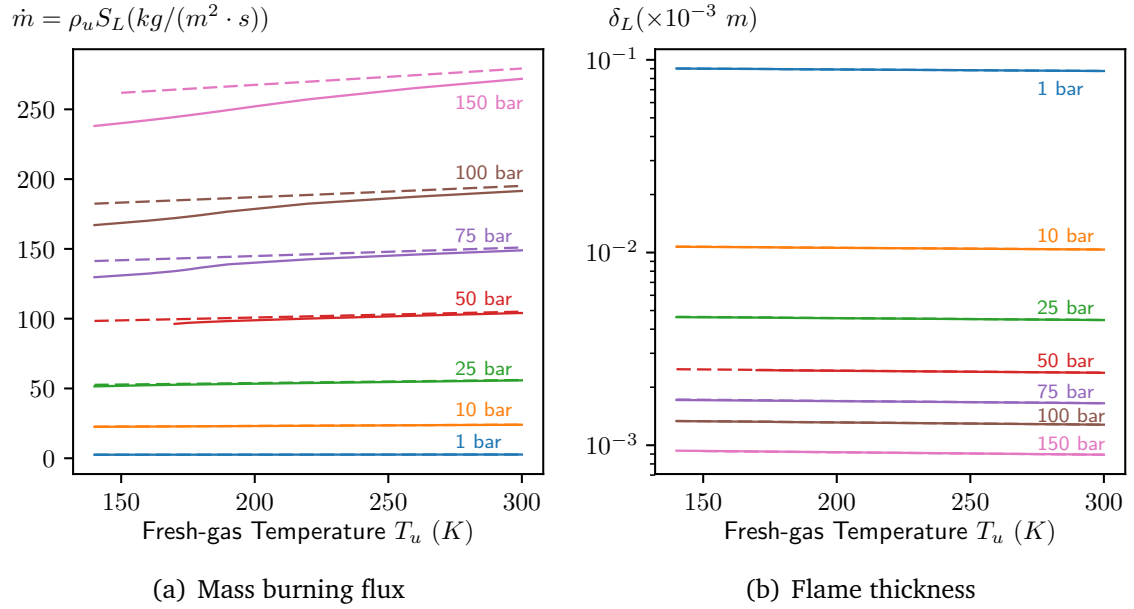


Figure 5.3: Variation of a) laminar mass burning rates and b) reaction zone thickness for stoichiometric premixed $CH_4 - O_2$ flames at a range of temperatures and pressures using Peng-Robinson EOS (—) and ideal gas law (- - -). Assumes low-pressure transport and $Le_k = 1$.

the specific heat capacity c_p is the amount of energy (J) required to raise the temperature of 1 kg of the fluid by 1 K . Due to the sharp rise in real gas c_p near the critical point, a larger heat transfer rate is required to sustain a fixed amount of thermal diffusion. Hence, the fluxes of conductive heat transfer jump sharply, followed by the convective fluxes to maintain the energy balance. In addition, flux of chemical energy transport due to species mass diffusion \dot{Q}_{diff} also shows a spike due to the unity Lewis number assumption.

5.1.3 Effect on mass burning rate and flame thickness

The mass burning rate \dot{m} and the reaction zone thickness δ_L are two parameters governing the dynamics of laminar premixed flames. The mass burning rate is the eigenvalue of the flame propagation, and is indicative of the balance between mass consumed by the flame as a response to kinetics, transport, and thermodynamic factors. The real gas mass burning rate is close to its ideal gas value

at low pressures. At increasing pressures, the real gas m drops substantially below the ideal gas value. And this effect is especially prominent at low temperatures.

Considering the thermal flame theory expression for the mass burning rate (Eqn. 3.6),

$$\rho_u S_L \approx \left[\lambda_* \frac{T_b - T_*}{h_* - h_u} \dot{\omega} \right]^{1/2} \quad (5.2)$$

The ignition temperature is expected to remain approximately the same in both cases. And since the real gas flame computations in this section assume low-pressure transport, and the real gas thermal conductivity is a function only of temperature like in the ideal gas case, and so we can expect that the axial profiles of thermal conductivity λ are approximately the same in both real gas and ideal gas cases, which also fix the real gas h_* and λ_* to approximately their ideal gas values. The real gas flame temperature T_b remains virtually unmodified. Therefore, the lowered real gas reactant enthalpy h_u alone lowers the rate of mass burning.

In Figure 5.3b, we see that the flame thickness δ_L remains largely unchanged with the real gas equation of state. The Peng-Robinson and ideal gas flame thickness collapse on top of each other. The flame thickness δ_L is estimated from the flame computation using the formula

$$\delta_L = \frac{T_b - T_u}{\max(dT/dx)}. \quad (5.3)$$

Since T_b and $\max(dT/dx)$ are obtained from the region in the flame where the temperature is too large to have any considerable non-ideal effects, we do not expect significant real gas effects on the flame thickness either.

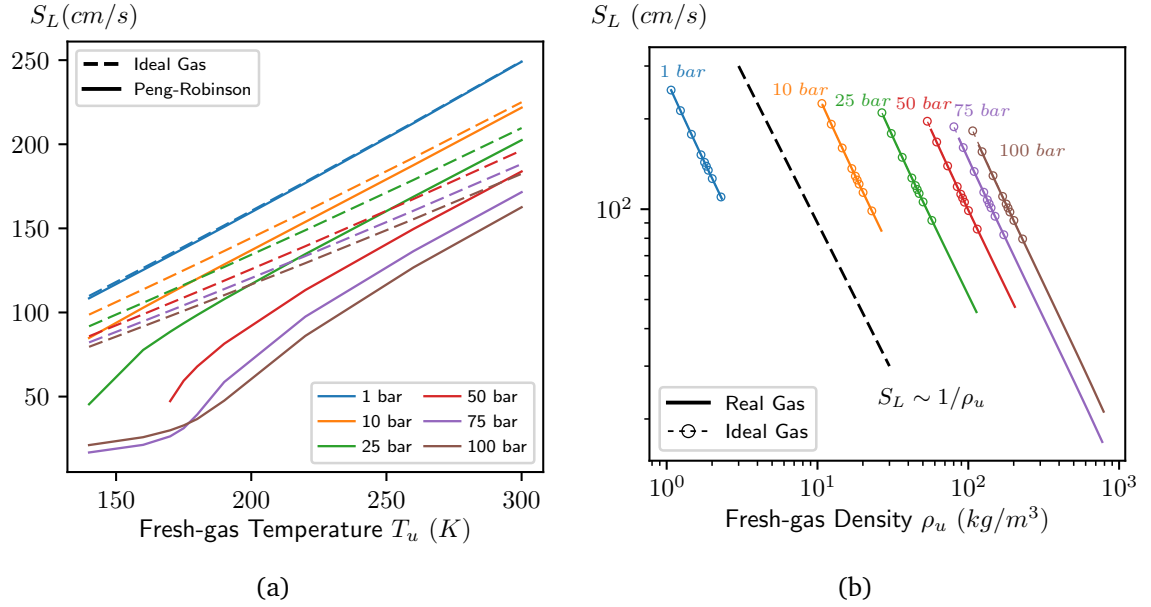


Figure 5.4: Variation of a) laminar flame speeds and b) flame temperatures for stoichiometric premixed $CH_4 - O_2$ flames at a range of temperatures and pressures using Peng-Robinson EOS (—) and ideal gas law (- - -, \circ). Assumes low-pressure transport and $Le_k = 1$. Mechanism from Lindstedt [32].

5.1.4 Effect on laminar flame speeds

We investigate the effect of fresh-gas temperatures and pressures on the laminar flame speeds S_L and flame temperatures T_b . In Figure 5.4a, the ideal gas flame speeds decrease consistently with lowered reactant temperatures, regardless of the operating pressure. In the case of a real gas, we first observe that the flame speeds decrease much more drastically with pressure, and have a stronger, non-linear dependence on fresh-gas temperature T_u . At 75 bar and 140 K, the real gas S_L is a factor of ~ 5 smaller than the ideal gas S_L . Secondly, the decrease with pressures at low temperatures is not monotonic. It is apparent that the 75 bar and 100 bar flame speed isobars crossover at a sufficiently low temperature.

Figure 5.4b shows that the flame speeds collapse when plotted against reactant density, implying that the effect of real gas density is the most important

factor in determining laminar flame speeds. The non-linear variation of real gas flame speeds with temperature, and the crossover behavior of the flame speed isobars, are also due to the non-linearity in the reactant densities. Since Figure 5.4b is expressed in a log-log scale, we can check the flame speeds for a power-law behavior. We observe that the slopes of flame speeds (vs ρ_u) of both the ideal gas and real gas cases in the log-log scale are approximately -1 , implying an inverse proportionality to ρ_u . This is consistent with the fundamental thermal flame theory due to Mallard and Le Chatelier [37]. The thermal flame theory connects the laminar flame speed to the flame's thermodynamic, transport and kinetic quantities as

$$S_L \approx \left[\frac{\lambda_* T_b - T_* \dot{\omega}}{\rho_u h_* - h_u \rho_u} \right]^{1/2}. \quad (5.4)$$

Since the flame speeds approximately follow the ρ^{-1} dependence, it suggests that the pressure dependence of the real gas h_u , and consequently T_b and $\dot{\omega}$, have a smaller effect on the flame speed compared to reactant density. This will be further clarified in the coming sections.

5.1.5 Effect on flame temperatures

Figure 5.5a plots the post-flame temperatures as a function of fresh-gas temperatures at various pressures. As we observed in the previous sections, the real gas flame temperatures are consistently lower than their ideal gas equivalents, with the margin of reduction appearing to increase with pressure. Secondly, there is a non-linear variation in flame temperatures near the critical region.

Just like in the case of the flame speeds, we can hope to determine the largest causal factor by scaling the flame temperatures with an appropriate quantity. Since we expect this variation in flame temperatures to be largely a consequence of the enhanced reactant enthalpies h_u at non-ideal conditions, we plot flame

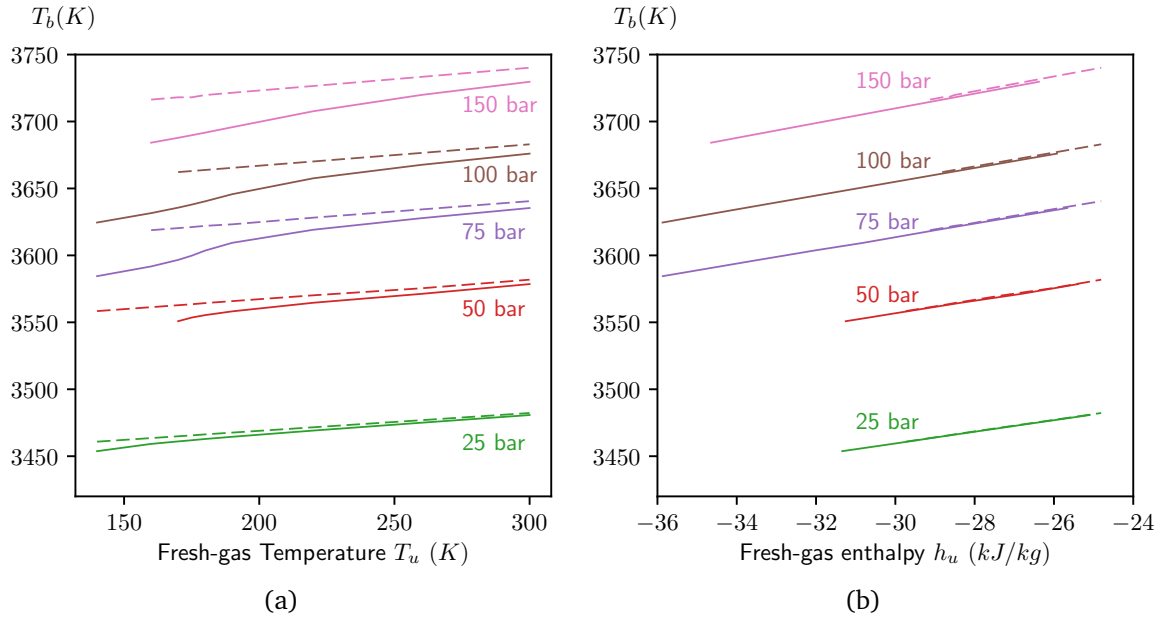


Figure 5.5: Scaling of a) laminar flame speeds with reactant density and b) flame temperatures with reactant enthalpy for stoichiometric premixed $CH_4 - O_2$ flames at a range of temperatures and pressures using Peng-Robinson EOS (—) and ideal gas law (- - -). Assumes low-pressure transport and $Le_k = 1$. Mechanism from Lindstedt [32].

temperatures as functions of h_u in Figure 5.5b. We find that the isobars for both cases are coincident, and vary linearly with reactant enthalpies. The reactant enthalpy is thus the largest factor in affecting post-flame temperatures in an ideal gas or real gas flame alike.

5.1.6 Effect of thermodynamic departure functions

In Section 5.1.4, we showed that the real gas reactant density has the largest influence on the laminar flame speeds, and in Section 5.1.5 we saw that it was the reactant enthalpy that had the most influence on flame temperatures. Our next step is to assess the influence of real gas enthalpy and heat capacities on flame dynamics. Since the physics of laminar flame propagation is governed by a coupled set of PDEs, it is not straightforward to isolate just the effect of departure functions. However, we can leverage the power of a computational study in turning models on or off. We perform another set of simulations with the departure functions set

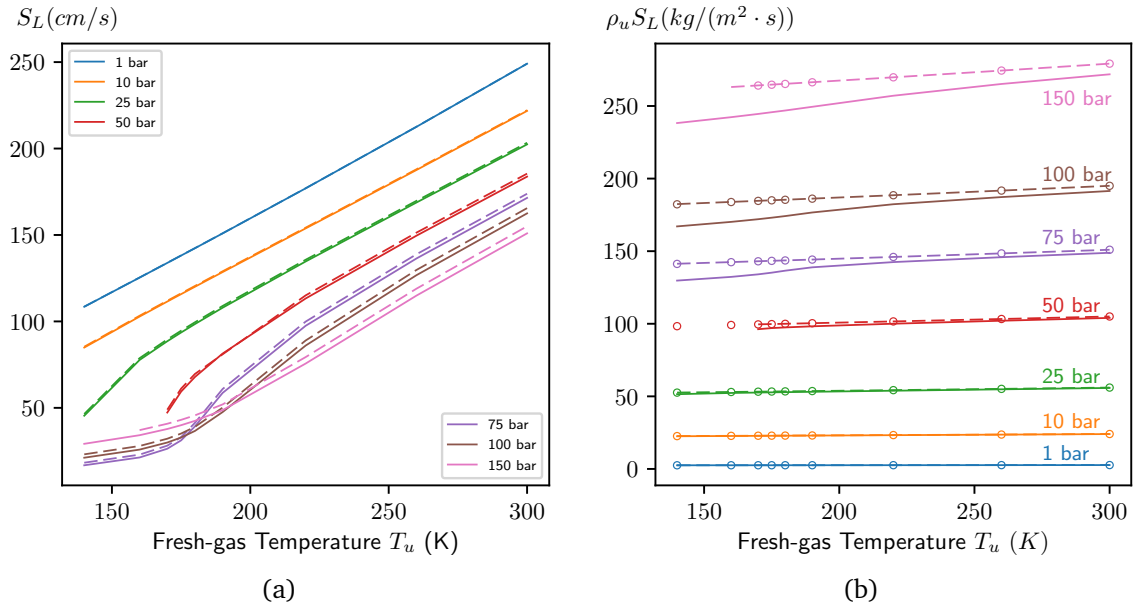


Figure 5.6: a) Laminar flame speeds and b) mass burning rates for stoichiometric premixed CH_4-O_2 flames using Peng-Robinson EOS for ρ and departure functions (—), Peng-Robinson EOS only for ρ without departure functions (- - -) and ideal gas (\circ). Assumes low-pressure transport and $Le_k = 1$.

to zero, while using the real gas density. The results are shown in Figure 5.6.

The mixture heat capacities and enthalpies, species enthalpies are only a function of temperature, like in the case of ideal gas computations. The results are shown in Figure 5.6 a).

In Figure 5.6a, it is seen that the overall effect of real gas enthalpies and heat capacities is to lower the flame speeds by a few percent, while not affecting the larger non-linear effects driven by the reactant density. This drop in flame speeds is higher at elevated pressures and low temperatures. The departure functions lower the flame speeds by two mechanism; Firstly, reactant enthalpies for a real gas are lower than the ideal gas equivalent, which decreases the adiabatic flame temperature and the associated chemical heat release and production rates and hence lowered flame speeds. Secondly, the enhanced reactant heat capacity lowers the thermal diffusivity, which slows the heat diffusion into pre-flame region

lowering flame speeds.

Figure 5.6b shows that without the departure functions, the mass burning rates recover their ideal gas values. As explained previously, the mass burning rates, in the presence of departure functions, are affected by both the lowered thermal diffusivity and lowered flame temperatures. It will be shown in later sections that the departure functions have the largest effect on real gas mass burning rates.

5.1.7 Equivalence ratio ϕ effects

Next, we investigate real gas effects with varying reactant composition. Figure 5.7 plots the flame speeds for this parametric study at low (175 K) and moderate (300 K) reactant temperatures, and a high pressure of 75 bar using the Peng-Robinson EOS. It is clear that the low and moderate temperature cases exhibit flame speeds that are qualitatively quite different. As first seen in Section 5.1.4, there is a sharper drop in flame speeds with increasing pressures in the low-temperature case. We also observe the crossover of flame speed isobars after a pressure > 70 bar, which was explained in Section 5.1.4 to be a consequence of non-linearities in real gas densities.

In the 300 K case, we can see the point of maximum flame speeds is shifted consistently to the right. In the low-temperature case, however, we observe that this behavior is only true until a pressure of 25 bar, after which the point of maximum flame speeds are shifted leftward (towards leaner mixtures) with increasing pressures. This trend continues until around 80 bar, beyond which the maximum flame speeds seem to have regained their high-temperature behavior. When the mass burning rate is plotted (Figure 5.8), we observe that the low and moderate temperature cases exhibit similar behavior, with the peaks shifting slightly towards richer mixtures with increasing pressures. The fact that the mass burning rates

have equivalent behavior is indicative of the dominant effect of reactant density in determining the laminar flame speeds.

Figure 5.9 plots density and heat capacities of pure methane and oxygen and several intermediate mixture compositions at 175 K. It is simpler now to see that the density of methane experiences drastic jumps as it undergoes a phase transition just after 25 bar. At low values of ϕ , the reactant mixture is fuel-lean and is dominated by the thermodynamic properties of the oxidizer O_2 , and at large values of ϕ it's the fuel species CH_4 which is dominant.

5.1.8 Differential diffusion effects ($Le_k \neq 1$)

With the real gas EOS and low-pressure transport, the thermal diffusivity α is dramatically reduced due to the combined effects of real gas density and heat capacity. This value of thermal diffusivity is not entirely physical due to the low-pressure thermal conductivity in use. Until this far, the species Lewis number was assumed to be unity, which constrained the real gas mass diffusivity to the artificially low value of mixture thermal diffusivity.

In this subsection, we relax the unity Lewis number constraint and explore differential diffusion effects with real gas EOS and low-pressure transport. Figure 5.10 shows the significantly enhanced mass diffusivity in the differential diffusion case. The mass-diffusion layer thickness is correspondingly enhanced in many of the reaction intermediates and products, but the diffusion layer thicknesses of H_2O , CO and CO_2 are especially enhanced in the pre-flame and fresh-gas region. This enhancement of mass diffusivity very visibly affects the profile of mixture density. Unlike the $Le_k = 1$ case, the density profile with differential diffusion does not decrease monotonically across the flame. The density in the pre-flame region first experiences a steady reduction followed by a prominent bump just before the

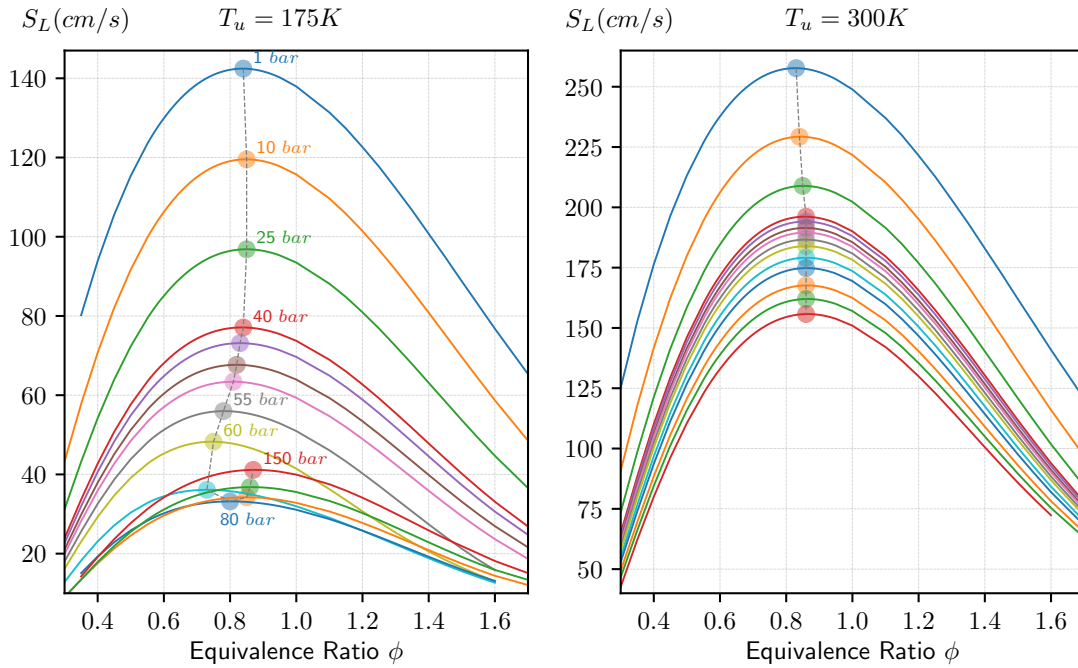


Figure 5.7: Variation of laminar flame speeds with equivalence ratio ϕ for stoichiometric premixed $CH_4 - O_2$ flames at fresh-gas temperatures of a) 175 K and b) 300 K. Both computations use Peng-Robinson EOS with $Le_k = 1$ and low-pressure transport.

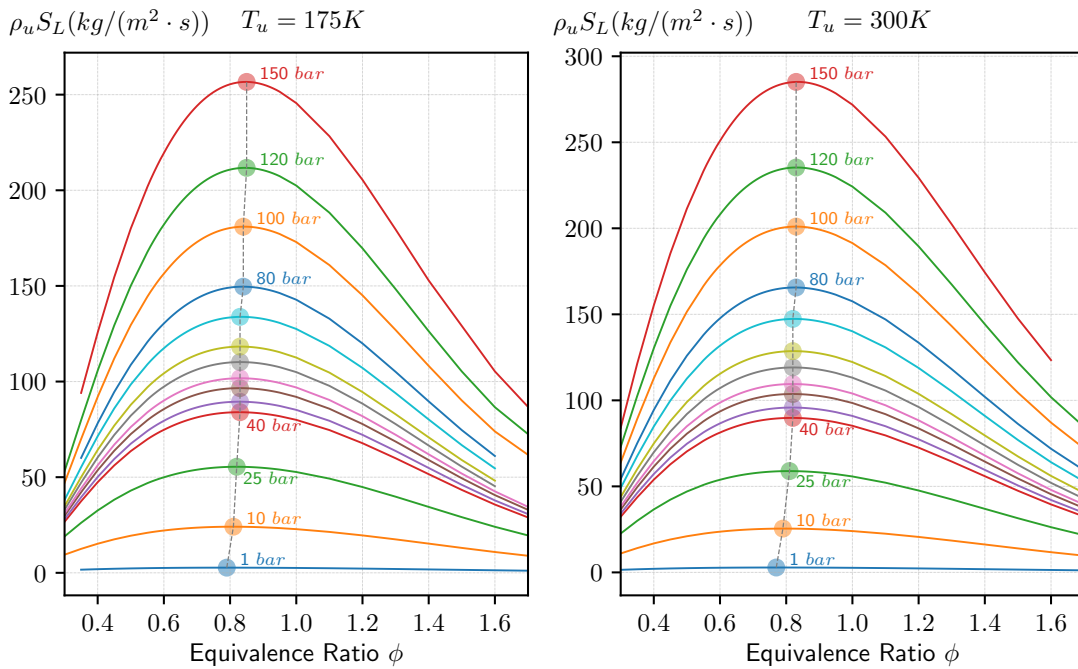


Figure 5.8: Variation of laminar mass burning rates with equivalence ratio ϕ for stoichiometric premixed $CH_4 - O_2$ flames at fresh-gas temperatures of a) 175 K and b) 300 K. Both computations use Peng-Robinson EOS with $Le_k = 1$ and low-pressure transport.

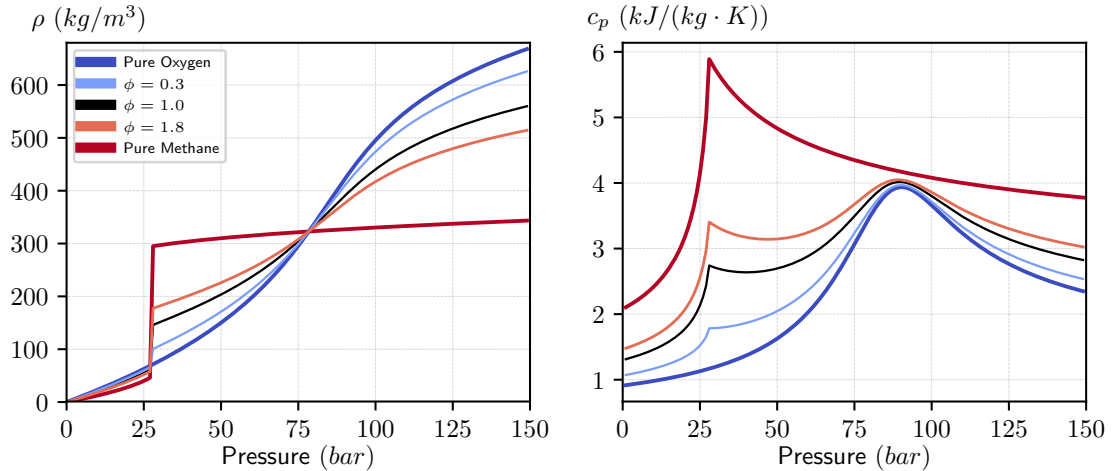


Figure 5.9: Densities and heat capacities of pure methane and oxygen and several intermediate mixture compositions at 175 K

flame front. The temperature profile across the flame also changes more steeply in response to these changes.

As this bump in density occurs only in real gas flames (with $Le_k \neq 1$), it is important to check if it's a consequence of non-linearity in thermodynamic property variation near the critical point of the reactants. However, since the thermal diffusivity is significantly reduced in the pre-flame region, the temperature profile is remarkably flat until very close to the flame front. With pressure and temperature fixed in the pre-flame region, the only other reason for abnormal behavior in density is likely to be the changes in mixture composition.

In the unburnt and preheat region, the changes in composition arise primarily due to the enhanced diffusion of H_2O , CO and CO_2 into the fresh-gas and pre-heat regions and the diffusion of O_2 and CH_4 into the flame region. The depletion of very-dense O_2 and CH_4 in the pre-heat region leads to the drop in mixture density that is observed before the start of density bump. Closer to the flame region, the enhancement of density (the density "bump") is primarily due to the enhanced diffusion of extremely-dense H_2O into the pre-flame region. At the conditions

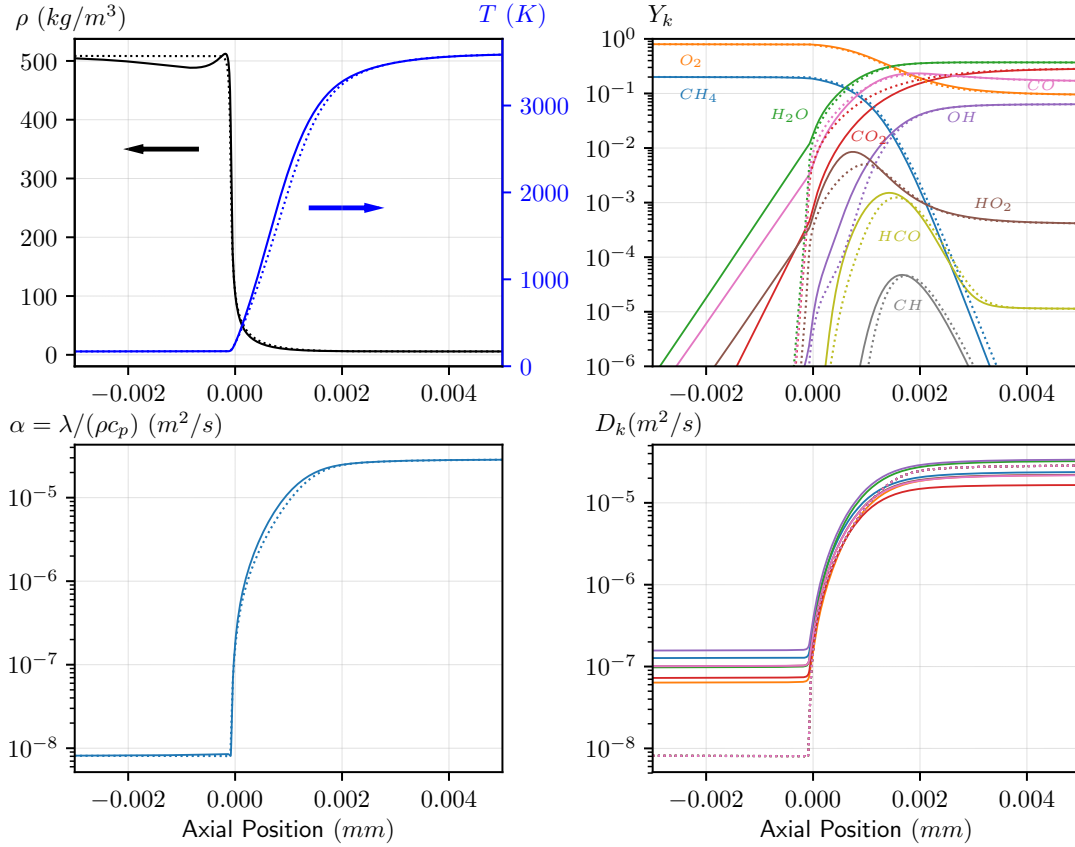


Figure 5.10: Profiles of mixture density ρ , temperature T , species mass fractions Y_k , thermal diffusivity α , and species mass diffusivity D_k for a transcritical premixed $CH_4 - O_2$ flame at 75 bar, $T_u = 170K$, with $Le_k \neq 1$ Peng-Robinson (—) and $Le_k = 1$ (- - -). Low-pressure transport assumed.

of low temperatures and high pressures prescribed by the pre-flame region, the density of H_2O is extremely high. Figure 5.11 shows the axial profiles of partial molar volumes for some major species in this region. The partial molar volume of each species is a measure of the change in mixture molar volume upon the addition of unit mole of the species. Out of all the species, H_2O has the most negative partial molar volume in the pre-flame region indicating that the mixture molar volume is bound to reduce, and the mixture density to go up, if the fraction of H_2O in the mixture were to go up. Looking at the plot of mass fraction in Figure 5.10, we see that this is indeed the case.

To investigate this further, we compute another flame with the exact similar

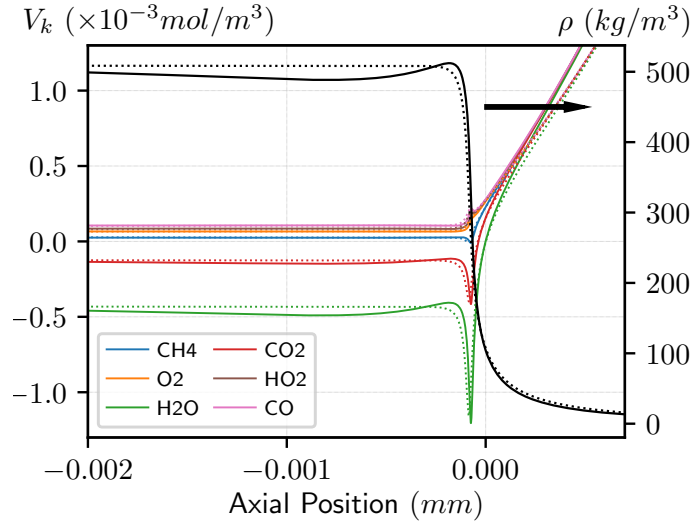


Figure 5.11: Profiles of species partial molar volumes V_k and mixture density ρ for a transcritical premixed $CH_4 - O_2$ flame at 75 bar, $T_u = 170K$, with $Le_k \neq 1$ (—) and $Le_k = 1$ (- - -). Peng-Robinson EOS is used with low-pressure transport is used.

conditions with the exception of Le of H_2O set to unity. If the bump in density largely depends on the enhanced diffusion of H_2O , then the new computation would yield a flame similar in all aspects to the previous case, with the exception of the density bump. In Figure 5.12, we see that this is the case. The density profile of the new computation matches the decreasing trends in the unburnt region and does not exhibit the bump as in the case the variable H_2O Lewis number. This confirms that the enhanced diffusion of H_2O is the reason for the bump in density. This effect is not completely physical, and is a deficiency of using differential diffusion effects with low-pressure transport in the context of the real-gas equation of state. We will show in the next section that enabling high-pressure transport causes this density bump to vanish.

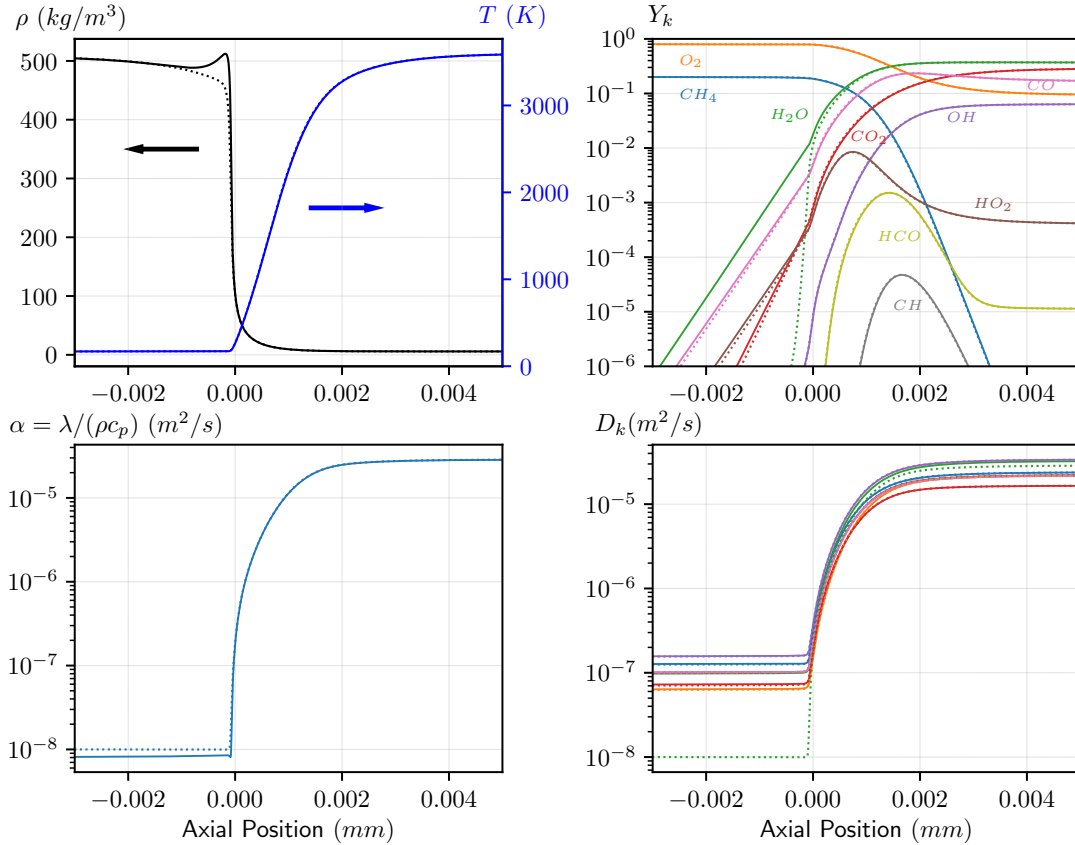


Figure 5.12: Profiles of mixture density ρ , temperature T , species mass fractions Y_k , thermal diffusivity α , and species mass diffusivity D_k for a transcritical premixed $CH_4 - O_2$ flame at 75 bar, $T_u = 170K$, with $Le_k \neq 1$ Peng-Robinson (—) and $Le_k \neq 1, Le_{H_2O} = 1$ (- - -). Low-pressure transport assumed .

5.2 Effect of real gas transport models

5.2.1 Flame structure

Now we look at the effect of high-pressure transport models with differential diffusion (Figure 5.13). Noticeably, the density bump vanishes from the pre-flame region. To understand why, it is useful to look at the the axial profiles of species Lewis number Le_k . The Lewis number in the fresh-gas region is much higher for the high-pressure transport compared to the low-pressure transport, indicative of the significantly reduced real gas mass diffusion. The mass diffusivity of H_2O in

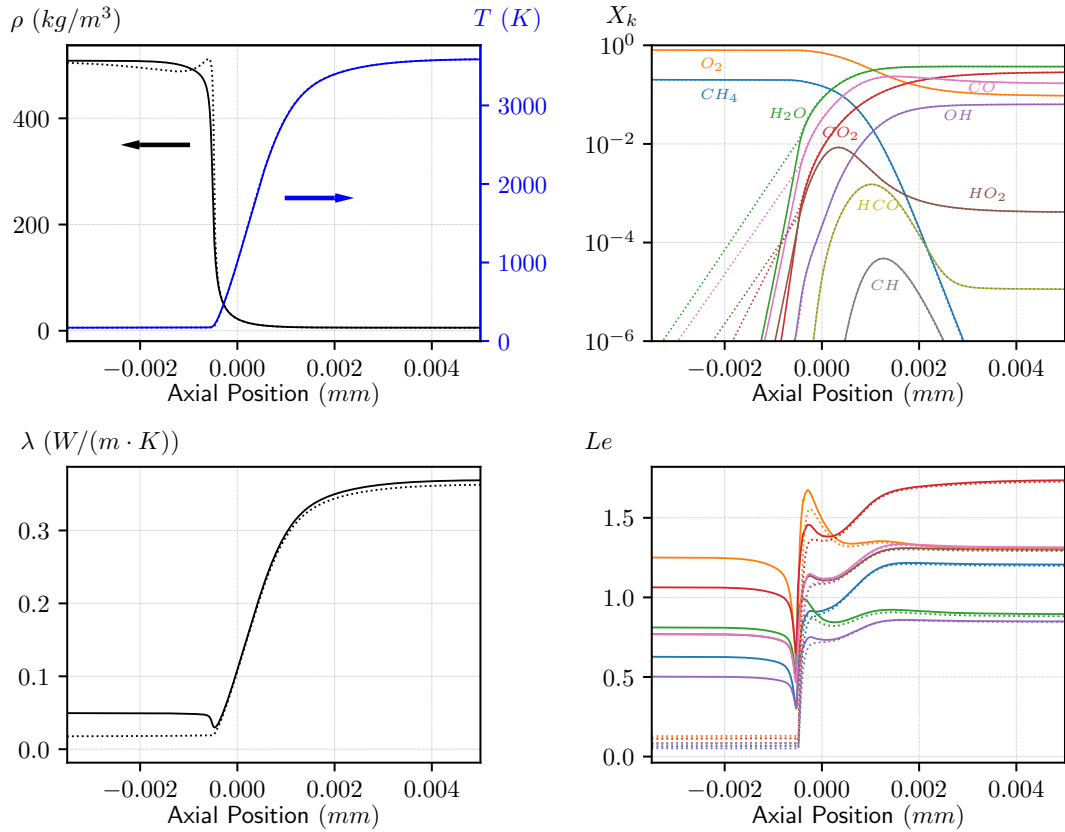


Figure 5.13: Profiles of mixture density ρ , temperature T , species mass fractions Y_k , thermal diffusivity α , and species Lewis number Le_k for a transcritical premixed $CH_4 - O_2$ flame at 75 bar, $T_u = 170K$, with high-pressure transport (—) and low-pressure transport (- - -). The Peng-Robinson EOS is used with differential diffusion effects.

the fresh-gas region is restored to a physically correct value, preventing excessive diffusion into the pre-flame region, and consequently a bump in density. The lowering of mixture density in the fresh-gas and the pre-flame region is also absent due to lower mass diffusion of CH_4 and O_2 .

The thermal conductivity in the high-pressure transport case is more enhanced in the pre-flame region, and marginally larger than than the corresponding low-pressure value in the flame and post-flame regions. The enhanced real gas thermal conductivity is noticeable in the pre-flame region, however, since the flame thermal conductivities are about the same, the effect on flame velocities is minimal.

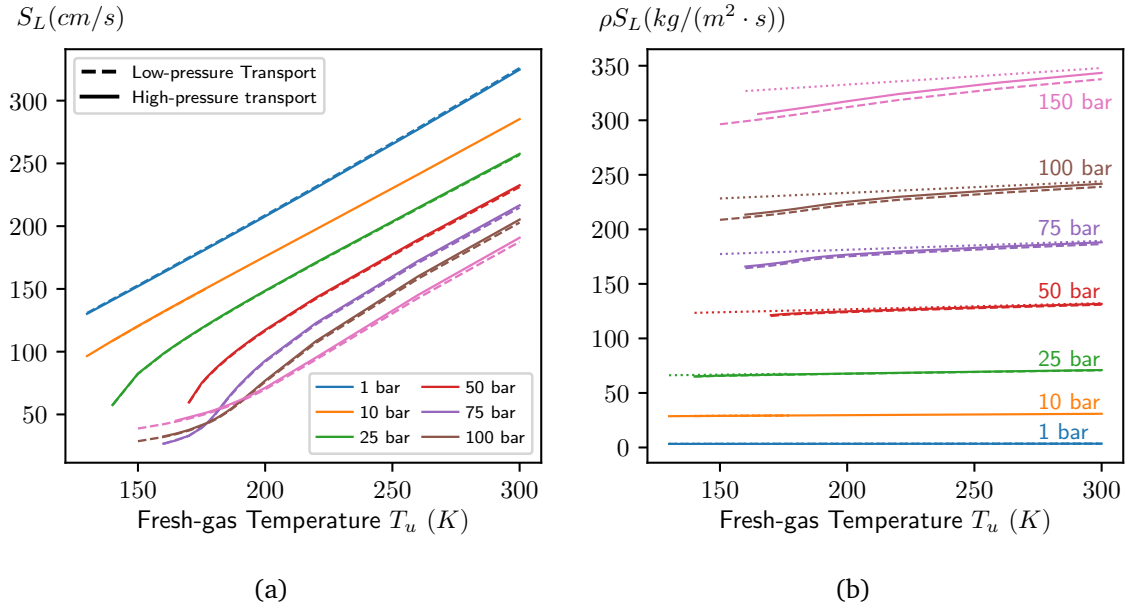


Figure 5.14: a) Laminar flame speeds and b) Mass burning rates of stoichiometric premixed $CH_4 - O_2$ mixtures with high-pressure transport (—), low-pressure transport (---) and ideal gas (.....).

5.2.2 Flame speed trends

Figure 5.14 plots the flame speeds and mass burning rates with the influence of high-pressure transport. It is evident that the high-pressure transport models make minimal difference to these two quantities. Our hypothesis is that laminar flame speeds and mass burning rates are a function of the thermal conductivity and mass diffusivity around the flame center. And since the temperature at the flame is sufficiently high, the low-pressure transport behavior tends to dominate. And any effect of the flame propagation velocities is marginal.

5.3 Effect of high-pressure chemical mechanisms

Experimental data and reaction mechanisms on CH_4 oxidation at high-pressures and low-temperatures are not available. However, several high-pressure CH_4 oxidation mechanism sets have been published. In Section 2.5.2, we per-

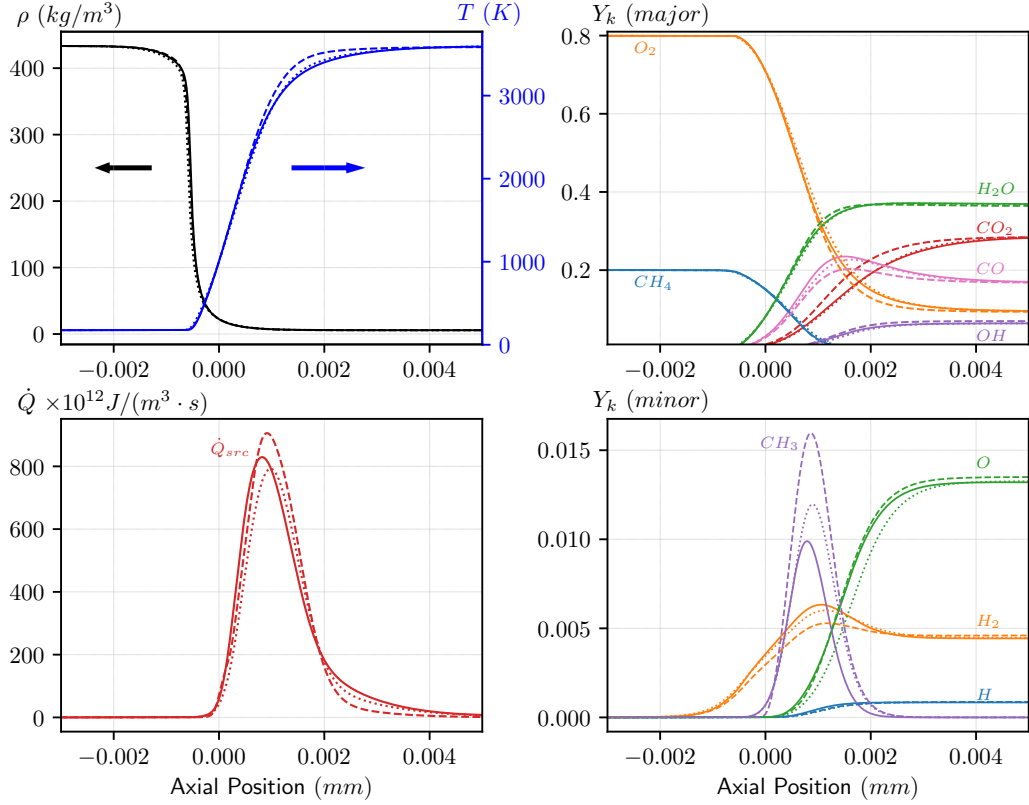


Figure 5.15: Profiles of mixture density ρ , temperature T , mass fractions Y_k of major and minor species, and chemical heat release rates \dot{Q}_{src} for a transcritical premixed $CH_4 - O_2$ flame at 75 bar, $T_u = 170K$, using the mechanisms from Lindstedt [32] (—), Huang et al. [21] (⋯) and [48] (- - -). Assumes Peng-Robinson EOS with high-pressure transport and $Le_k \neq 1$.

formed tests of kinetics implementation using the high-pressure mechanism from Huang et al. [21] and Petersen et al. [48]. In this section, we investigate the effects of the two mechanisms on transcritical flames.

Figure 5.15 shows the effect of the Huang et al. [21] and Petersen et al. [48] mechanisms on the flame structure. The Petersen et al. [48] mechanism has a less diffuse temperature profile, and higher peak heat release rates compared to Lindstedt [32] and Huang et al. [21]. The enhanced rate of oxidation of CO to CO_2 , which is an exothermic reaction, is responsible for the heat release rates in Petersen et al. [48].

The difference in heat release rates has consequences for the laminar flame

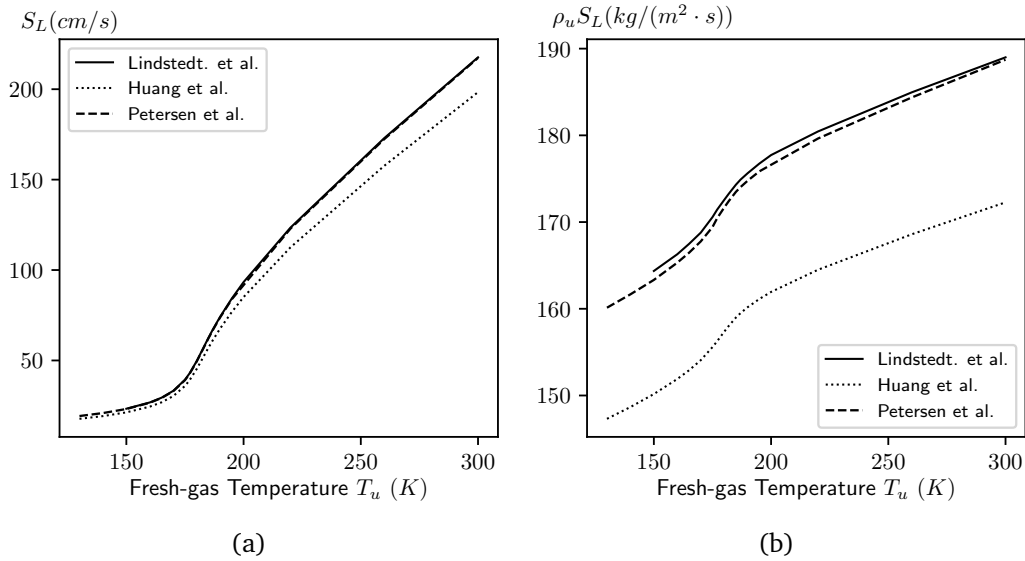


Figure 5.16: a) laminar flame speeds and b) mass burning rates for stoichiometric premixed CH_4-O_2 flames at 75 bar using the kinetic mechanisms from Lindstedt [32] (—), Huang et al. [21] (⋯⋯) and [48] (- - -). Assumes Peng-Robinson EOS with high-pressure transport and $Le_k \neq 1$.

speeds and mass burning rates. In Figure 5.16a, we see that Huang et al. [21] predicts the lowest flame speeds, whereas Lindstedt [32] and Petersen et al. [48] yield largely similar flame speeds. Lindstedt [32] and Petersen et al. [48] exhibit consistently larger chemical production rates compared to Huang et al. [21].

Chapter 6: Conclusions and future directions

This dissertation describes the development of a computational methodology to investigate real gas effects in laminar premixed flames and then systematically investigates premixed $CH_4 - O_2$ flames with reactant thermodynamic states near the critical point. The Peng-Robinson equation of state has a strong non-linear effect on the laminar flame speeds, especially at lower temperatures and high pressures. The real gas laminar flame speeds S_L are lowered by a factor of 5 for reactant thermodynamic states near the critical point. However, real gas laminar mass burning rates $\rho_u S_L$ are lowered by just around 10%, implying that the enhanced real gas reactant densities have the largest effect on flame speeds. The burnt-gas temperatures are lowered by 1% at the most, even near the critical point. We find the effect on laminar flame thickness to be negligible.

We find that real gas effects are largely important in the fresh-gas and pre-flame regions. At the point in the flame where the temperature reaches $\sim 500K$, the thermodynamic non-idealities have largely subsided. We are also able to identify specifically which modifications to the equation of state have the largest effect on flame parameters. The enhanced real gas reactant density has the single largest effect on flame speeds, whereas deviations in real gas mass burning rates and flame temperatures depend mostly on the effect of real gas departure functions.

We illustrate the importance of using high-pressure transport in flame com-

putations with differential diffusion effects. When differential diffusion effects are used in conjunction with the real gas EOS and low-pressure transport, the artificially enhanced mass diffusivity of H_2O causes highly-dense H_2O to diffuse into the pre-heat region, thereby causing a non-physical bump in density. This non-physical effect is reversed when high-pressure transport properties are used, and mass diffusivities are reverted back to physically-correct low values. High-pressure transport properties, however, have only minimal effects on laminar flame speeds and mass burning rates. The mass burning rates are enhanced by $\sim 5\%$ as a consequence of high-pressure thermal conductivities and mass diffusivities.

We find that the qualitative trends in the real gas laminar flame speeds and mass burning rates remain unaffected between different chemistries. The low-pressure Lindstedt [32] and high-pressure Petersen et al. [48] mechanisms exhibit enhanced overall reaction and heat release rates compared to the high-pressure Huang et al. [21] mechanism. The effect on the overall laminar flame structure is not substantial.

6.1 Publications and presentations

Peer-reviewed publications

1. (To be submitted) Gopal, A., Volpiani, P.S., Yellapantula, S. and Larsson, J., 2019. Structure and propagation of planar transcritical premixed $CH_4 - O_2$ flames. *Journal of Supercritical Fluids*

Conference publications

1. Gopal, A., Volpiani, P.S., Yellapantula, S. and Larsson, J., 2019, March. Numerical investigation of real gas effects in premixed $CH_4 - O_2$ flames at cryogenic conditions. Proceedings of 11th US National Combustion Meeting, Pasadena, CA.

Conference presentations

1. Gopal, A., Yellapantula, S. and Larsson, J., 2017, November. Investigating the effects of critical phenomena in premixed methane-oxygen flames at cryogenic conditions. APS Division of Fluid Dynamics, Denver, CO.
2. Gopal, A., Yellapantula, S. and Larsson, J., 2015, November. Quantifying real-gas effects on a laminar n-dodecane-air premixed flame. APS Division of Fluid Dynamics, Boston, MA.

6.2 Future directions

Based on the findings that real gas effects are important mainly in the fresh-gas region, and that the enhanced fresh-gas density, enthalpy, and heat capacities have a large effect on flame propagation, it may be worthwhile exploring the possibility of developing a model for real gas flame speeds based on ideal gas flame speeds. In the fresh-gas region, the thermodynamic states are known with certainty, and so the fresh-gas density, enthalpy and heat capacities may be estimated a priori using the equation of state. The real gas flame speeds can be obtained by the knowledge of how ideal gas flame speeds scale with the fresh-gas properties.

This study considered several high-pressure chemical mechanisms to better

understand the role of kinetics at transcritical conditions. However, there is a need for chemical mechanisms that are specifically constructed for low-temperature, high-pressure regimes. This is one possible avenue for further exploration as low-temperature mechanisms become available.

Appendices

Appendix A

UnsteadyFlame: transient solver

The numerical methods used to implement the time-unsteady, compressible, reacting flow solver are described here. This solver uses a second-order finite-volume discretization in space and a fourth-order Runge-Kutta (RK4) time integration scheme. To prevent pressure fluctuations from affecting the domain, we use characteristic boundary conditions at the inlet and outlet, coupled with controllers tasked with keeping the flame stationary.

Transient solvers will converge to the correct values as long as the time step size meets the stability criterion. As we are interested only in the steady-state solution from transient solvers and so instantaneous solutions are not required to be correct. This allows us to accelerate the solution process using local time-stepping. This is the approach used in the present study.

A.1 Governing equations

The conservation equations for fully-compressible, reacting flows in one-dimension (Eqn. 2.1 through Eqn. 2.4) can be rewritten for clarity in terms of the

conserved variable Q , and the convective C , diffusive D and source S terms

$$\frac{\partial Q}{\partial t} = -\frac{\partial C}{\partial x} + \frac{\partial D}{\partial x} + S, \quad (\text{A.1})$$

where Q

$$Q = \left[\rho \quad \rho u \quad \rho Y_1 \quad \dots \quad \rho Y_k \quad \rho e_t \right]^T,$$

C and D are the vectors containing the convective and diffusive terms, respectively,

$$C = \left[\rho u \quad \rho u^2 + p \quad \rho(u + V_c)Y_1 \quad \dots \quad \rho(u + V_c)Y_k \quad \rho u e_t + p u \right]^T,$$

$$D = \left[0 \quad \frac{4}{3}\mu \frac{\partial u}{\partial x} \quad \rho D_1 \frac{W_1}{W} \frac{\partial X_1}{\partial x} \quad \dots \quad \rho D_k \frac{W_k}{W} \frac{\partial X_k}{\partial x} \quad -\lambda \frac{\partial T}{\partial x} + \rho \sum_k h_k Y_k V_k + \frac{4}{3}\mu u \frac{\partial u}{\partial x} \right]^T,$$

and S is the vector representing the source terms

$$S = \left[0 \quad 0 \quad \dot{\omega}_1 \quad \dots \quad \dot{\omega}_k \quad 0 \right]^T.$$

A.2 Finite volume formulation

Integrating Eqn. A.1 over a grid cell with volume V , and area A , we get

$$\iiint_V \frac{\partial Q}{\partial t} dV = \iiint_V \left[-\frac{\partial C}{\partial x} + \frac{\partial D}{\partial x} + S \right] dV.$$

Using Gauss's divergence theorem, the volume integral is transformed into a surface integral as

$$\frac{\partial Q}{\partial t} V = \iint_A [-C + D] n \cdot dA + SV,$$

where n represents the normal vector to the cell face. The above expression can be simplified for a one-dimensional computational cell as

$$\frac{\partial Q}{\partial t} = \frac{1}{\Delta x} [(C)_w - (C)_e] + \frac{1}{\Delta x} [(D)_e - (D)_w] + S.$$

Subscripts e and w indicate that the flux vectors C and D are evaluated at the east and west faces, respectively. This spatial discretization used is second-order accurate.

In the present approach, the cell-centered values of the state vector Q and all the associated variables are stored in memory. To obtain face-centered quantities from their cell-centered equivalents, a linear interpolation is used

$$\phi_i^f = (1 - r_i)\phi_{i-1}^c + r_i\phi_i^c \quad i \in 0, 1, \dots, N_{faces},$$

where ϕ^f and ϕ^c are the face-centered and cell-centered quantities, respectively, and r_i is the linear interpolation coefficient

$$r_i = \frac{x_i^f - x_{i-1}^c}{x_i^c - x_{i-1}^c},$$

and has a value of 1/2 for a uniform grid.

A.3 Computational grids

While a uniform grid is simple to implement, there are several advantages to using a grid with non-uniform grid spacing that uses finer resolution around the stronger physical features. Firstly, fewer grid points are required to achieve the same level of accuracy, relative to a uniform grid, thus saving computational time. Secondly, the controllers achieve convergence much faster in the case of a stretched

Parameter	Description
N	Total number of grid points
β_{fine}	Fraction of the total domain length to be refined
N_{fine}	Fraction of the total grid points to be allocated towards the finer mesh
X_{fine}	Axial position of the midpoint of the finer mesh

Table A.1: Grid stretching parameters

mesh. Thirdly, the computational time is accelerated with local time stepping.

The grid refinement process is fairly trivial as the flame front represents the region needing refinement. The grid is generated prior to the solver initialization, as a pre-processing step. Due to the presence of the flame controllers, adaptive meshing is not necessary. An extremely-fine uniform mesh is used around the flame region, flanked by variably-spaced grids extending to the inlet and exit plane. The algorithm to generate the stretched grid accepts four parameters as listed in Table A.1.

After the initial stretched grid is generated, a filtering function is run ~ 200 times to smoothen the abrupt variation in grid spacing from the finer central mesh to the flanks.

$$x_{face}[i] = \frac{1}{4}x_{face}[i-1] + \frac{1}{2}x_{face}[i] + \frac{1}{4}x_{face}[i+1]$$

Figure A.1 represents a sample stretched grid with parameters, $N = 256$, $\beta_{fine} = 0.2$, $N_{fine} = 0.67$.

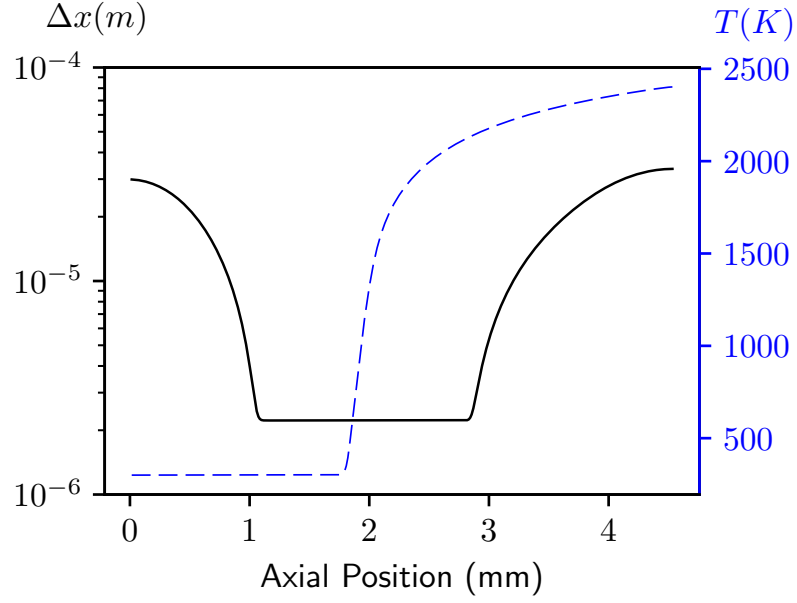


Figure A.1: Sample stretched grid with $N = 1024$, $\beta_{fine} = 0.4$, $N_{fine} = 0.8$ and $X_{fine} = 0.45$

A.4 Time advancement

This code uses the fourth-order Runge-Kutta scheme to advance the solution in time. The upper bound on the time-step size for the solver to be stable is determined by the CFL criterion. We need to estimate the maximum spectral radius from each physical process present in the simulation. In order, the terms are convection, viscous diffusion, thermal diffusion, species diffusion, and species production. However, estimating the species production spectral radius is computationally intensive, and is skipped from the definition of the maximum spectral radius.

$$S_{max} = \max(S_{conv}, S_{\nu}, S_{\lambda}, S_D, S_{\omega}),$$

where S_x represents the spectral radius of the x^{th} term. Knowing the maximum spectral radius, the largest allowed time-step size can be estimated as

$$\Delta t = \frac{C}{S_{max}}$$

where C is the Courant number, and typically $C \leq 2$ for the RK4 scheme.

A.5 Boundary conditions

With the choice of a compressible solver, acoustic waves are present in the domain throughout the process of attaining steady state. Because the solver uses unphysical guesses for the initial conditions, there are especially pronounced pressure transients right after the initial few time steps. These pressure fluctuations, if not properly allowed to leave the domain, affect the flame front and in turn produce more pressure fluctuations. Further, a coupling between the heat release term and the pressure fluctuation can result in combustion instabilities. To get a solution without the interference of acoustic waves, the inlet and outlet boundaries must allow acoustic waves to leave the domain.

Compressible codes often use a sponge layer at the boundaries, with artificially-high dissipation to remove the high-frequency pressure oscillations. However, this involves extending the computational domain by a considerable amount and can be computationally inefficient. Further, this method does not allow us to control the flame drift velocity. Instead, we use the method of characteristics to decompose the information traveling into and out of the domain.

A.5.1 Characteristic non-reflecting boundary conditions

In the present work, we use a set of characteristic non-reflecting boundary conditions similar to the work by Poinot and Lele [50]. The method of characteristics allows a solution for a set of hyperbolic PDEs by converting them to a set of ODEs, which lend themselves to an easier solution process. Neglecting the effects of diffusion and chemistry at the boundaries, we can convert the governing

equations at the boundaries from the Navier-Stokes relations to the inviscid Euler equations. Further, the small perturbation assumption allows us to linearize the set of equations around a local flow condition. Diagonalizing the resulting matrix yields, we can construct a Local One-Dimensional Inviscid (LODI) set of ODEs in which the eigenvectors of the matrix (Riemann invariants) are advected by the corresponding eigenvalues (characteristic speeds). Our implementation differs from [50] in its application to a finite volume formulation.

The characteristic variables traveling with speeds u , $u+c$, $u-c$ are respectively w_1 , w_2 , and w_3 . In terms of the fluid properties, these variables can be expressed as

$$\begin{aligned}
 w_1 &= \rho - \frac{p_1}{c^2} \\
 w_2 &= 1/2(p + (\rho_{av}c_{av})u) \\
 w_3 &= 1/2(p - (\rho_{av}c_{av})u)
 \end{aligned}
 \tag{A.2}$$

With knowledge of the characteristic variables at the interior grid cell or at the externally-imposed conditions, it is straightforward to determine the fluid properties at the boundary (inlet or outlet) planes. Assuming the flow of reactants from the inlet to the outlet, we can decide whether the characteristic variables at the boundaries need to be taken from the interior points or from the imposed values. At the inlet, the characteristics are taken from the imposed values for positive characteristic velocities, and from the interior for the negative characteristic velocities,

$$\begin{aligned}
 w_1|_{inlet} &= w_1|_{imposed} & u_{inlet} > 0 \\
 &= w_1|_{x_1} & u_{inlet} \leq 0 \\
 w_2|_{inlet} &= w_2|_{imposed} \\
 w_3|_{inlet} &= w_3|_{x_1}.
 \end{aligned}
 \tag{A.3}$$

Similarly, at the outlet plane, the characteristics are taken from the interior points

for positive characteristic velocities,

$$\begin{aligned}
 w_1|_{outlet} &= w_1|_{x_N} \\
 w_2|_{outlet} &= w_2|_{x_N} \\
 w_3|_{outlet} &= w_3|_{imposed}.
 \end{aligned}
 \tag{A.4}$$

Once the characteristic variables at the boundary planes are known, we can get the state variables using the expressions

$$\begin{aligned}
 \rho_{bnd} &= w_1|_{bnd} + \frac{w_2|_{bnd} + w_3|_{bnd}}{c_{av}^2} \\
 u_{bnd} &= \frac{w_2|_{bnd} - w_3|_{bnd}}{c_{av}\rho_{av}} \\
 p_{bnd} &= w_2|_{bnd} + w_3|_{bnd} \\
 Y_k|_{inlet} &= Y_k|_{imposed} \\
 Y_k|_{outlet} &= Y_k|_{interior}
 \end{aligned}
 \tag{A.5}$$

A.5.2 Boundary controllers

In addition to allowing pressure fluctuations to leave the computational domain, the boundary conditions must allow the laminar premixed flame to attain a zero-drift velocity at steady state. Further, the outlet pressure and the inlet temperature must return to their respective prescribed values before steady-state. This process has to necessarily be smooth so as to not affect the stability of the convergence process.

This is accomplished by adding a correction term to the incoming characteristics at the inlet and exit planes and making sure that the correction terms tend to zero at steady-state. The correction terms essentially act as proportional controllers.

Three controllers are used in the present study, an inflow velocity controller and temperature controller at the inlet and pressure controller at the outlet plane. For each controller, a constant parameter known as the tuning constant needs to be set. The tuning constant is found by trial and error so as to achieve the fastest convergence with the most stable flame movements.

The inflow boundary condition is a non-reflecting boundary condition coupled with inlet controllers to ensure that the inlet temperature and velocity do not drift away from the target. To do this, we add correction terms to the characteristics coming from outside the domain to the inlet like

$$\begin{aligned}
w_1|_{imposed} &= \rho_{imposed} - \frac{p_{imposed}}{c^2} + \Delta w_1|_{imposed} \\
w_2|_{imposed} &= 1/2(p_{imposed} + (\rho_{av}c_{av})u_{imposed}) + \Delta w_2|_{imposed} \\
w_3|_{imposed} &= 1/2(p_{imposed} - (\rho_{av}c_{av})u_{imposed}).
\end{aligned} \tag{A.6}$$

The correction terms are of the form

$$\begin{aligned}
\Delta w_1|_{imposed} &= k_T \Delta t (T_{inlet} - T_{imposed}) \left(\frac{p_{av} W_{av}}{Z_{imposed} R T_{av}^2} \right) \\
\Delta w_2|_{imposed} &= k_u \Delta t (0 - u_{fc}) \left(\frac{\rho_{av} c_{av}}{2} \right),
\end{aligned} \tag{A.7}$$

where k_T and k_u are the tuning constants for the temperature and velocity controllers, respectively.

Similarly, at the outlet, we have

$$\begin{aligned}
w_1|_{imposed} &= \rho_{imposed} - \frac{p_{imposed}}{c^2} \\
w_2|_{imposed} &= 1/2(p_{imposed} + (\rho_{av}c_{av})u_{imposed}) \\
w_3|_{imposed} &= 1/2(p_{imposed} - (\rho_{av}c_{av})u_{imposed}) + \Delta w_3|_{imposed},
\end{aligned} \tag{A.8}$$

with the pressure correction term

$$\Delta w_3|_{imposed} = k_P \Delta t \frac{(p_{inf} - p_{outlet})}{2}$$

Here k_P is the tuning constant for the pressure controller.

Appendix B

Real-gas thermodynamics – partial molar properties

To close the system of governing equations represented by Eqn. 2.1 through Eqn. 2.4, we need to estimate the partial molar properties for the molar volume, enthalpy, and specific heat capacities given the respective mixture-averaged quantities. In general, for an arbitrary thermodynamic quantity \mathcal{A} , the partial molar property for the l^{th} species is the change in the quantity as a result of a unit change in the number of moles of the l^{th} species, fixing the temperature, pressure, and all the other species compositions. Mathematically, this results in the expression

$$\mathcal{A}_{,l} = \left(\frac{\partial \mathcal{A}}{\partial N_l} \right)_{T,p,N_{k,k \neq l}} \quad (\text{B.1})$$

For the partial molar volume of the l^{th} species $V_{,l}$, this expression becomes

$$V_{,l} = \left(\frac{\partial \mathcal{V}}{\partial N_l} \right)_{T,p,N_{k,k \neq l}} . \quad (\text{B.2})$$

As many equations of state are explicit in pressure, we convert the above expression

to partial derivatives of pressure using the chain rule as,

$$V_{,l} = \left(\frac{\partial V}{\partial N_l} \right)_{T,p,N_{k,k \neq l}} = \left(\frac{\partial V}{\partial p} \right)_{T,N} \left(\frac{\partial p}{\partial N_l} \right)_{T,V,N_{k,k \neq l}}. \quad (\text{B.3})$$

Expressing the Peng-Robinson EOS (Eqn. 2.37) in terms of the number of moles N , and the specific volume \mathcal{V} ($1/\rho$),

$$p = \frac{NR_u T}{\mathcal{V} - Nb_m} - \frac{N^2 A_m}{\mathcal{V}^2 + 2Nb_m \mathcal{V} - N^2 b_m^2} \quad (\text{B.4})$$

We proceed to estimate the partial derivatives of p required in Eqn. B.3

$$\begin{aligned} \left(\frac{\partial p}{\partial \mathcal{V}} \right)_{T,N} &= \frac{NR_u T}{(\mathcal{V} - Nb_m)^2} - \frac{N^2 A_m (2\mathcal{V} + 2Nb_m)}{(\mathcal{V}^2 + 2Nb_m \mathcal{V} - N^2 b_m^2)^2}, \\ \left(\frac{\partial p}{\partial \mathcal{V}} \right)_{T,N} &= \frac{1}{N} \left(\frac{\partial p}{\partial V} \right)_{T,N}. \end{aligned} \quad (\text{B.5})$$

$$\begin{aligned} \left(\frac{\partial p}{\partial N_l} \right)_{T,\mathcal{V},N_{k,k \neq l}} &= \frac{R_u T}{\mathcal{V} - Nb_m} - \frac{b_l NR_u T}{(\mathcal{V} - Nb_m)^2} \\ &\quad - \frac{2 \sum_{k=1}^{N_s} A_{lk} N_k}{\mathcal{V}^2 + 2Nb_m \mathcal{V} - N^2 b_m^2} \\ &\quad + \frac{(2\mathcal{V} B_l - 2Nb_m b_l) N^2 A_m}{(\mathcal{V}^2 + 2Nb_m \mathcal{V} - N^2 b_m^2)^2} \end{aligned} \quad (\text{B.6})$$

In the derivation of the expression given by Eqn. B.6, we need additional partial derivatives,

$$Nb_m = N \sum_{k=1}^{N_s} \frac{N_k}{N} b_k = \sum_{k=1}^{N_s} N_k b_k = N_l b_l + \sum_{\substack{k=1 \\ k \neq l}}^{N_s} N_k b_k, \quad (\text{B.7})$$

then

$$\begin{aligned} \left(\frac{\partial Nb_m}{\partial N_l} \right)_{T,\mathcal{V},N_{k,k \neq l}} &= \left(\frac{\partial N_l b_l}{\partial N_l} \right)_{T,\mathcal{V},N_{k,k \neq l}} + \left(\frac{\partial \sum_{\substack{k=1 \\ k \neq l}}^{N_s} N_k b_k}{\partial N_l} \right)_{T,\mathcal{V},N_{k,k \neq l}} \\ &= b_l \end{aligned} \quad (\text{B.8})$$

Similarly,

$$\begin{aligned}
 N^2 A_m &= N^2 \sum_{j=1}^{N_s} \sum_{k=1}^{N_s} \frac{N_j}{N} \frac{N_k}{N} A_{jk} = \sum_{j=1}^{N_s} \sum_{k=1}^{N_s} N_j N_k A_{jk} \\
 &= 2 \sum_{j=1}^{N_s} N_j N_l A_{jl} + \sum_{\substack{j=1 \\ j \neq l}}^{N_s} \sum_{\substack{k=1 \\ k \neq l}}^{N_s} N_j N_k A_{jk}
 \end{aligned} \tag{B.9}$$

and

$$\begin{aligned}
 \left(\frac{\partial N^2 A_m}{\partial N_l} \right)_{T, V, N_k, k \neq l} &= \left(\frac{\partial 2 \sum_{j=1}^{N_s} N_j N_l A_{jl}}{\partial N_l} \right)_{T, V, N_k, k \neq l} + \left(\frac{\partial \sum_{\substack{j=1 \\ j \neq l}}^{N_s} \sum_{\substack{k=1 \\ k \neq l}}^{N_s} N_j N_k A_{jk}}{\partial N_l} \right)_{T, V, N_k, k \neq l} \rightarrow 0 \\
 &= 2 \sum_{j=1}^{N_s} N_j A_{jl}
 \end{aligned} \tag{B.10}$$

So the expression for species molar volume becomes

$$V_l = \frac{-1}{\left(\frac{\partial p}{\partial V} \right)_{T, n}} \left(\frac{R_u T}{V - b_m} + \frac{R_u T b_l}{(V - b_m)^2} - \frac{\sum_j N_j A_{jl}}{V^2 + 2V b_m + b_m^2} + \frac{2A_m (V - b_m) b_l}{(V^2 + 2V b_m + b_m^2)^2} \right). \tag{B.11}$$

In terms of mole fractions, the expression is

$$V_l = \frac{-1}{\left(\frac{\partial p}{\partial V} \right)_{T, n}} \left(\frac{R_u T}{V - b_m} + \frac{R T b_l}{(V - b_m)^2} - \frac{\sum_j X_j A_{jl}}{V^2 + 2V b_m + b_m^2} + \frac{2A_m (V - b_m) b_l}{(V^2 + 2V b_m + b_m^2)^2} \right) \tag{B.12}$$

The expression for the partial molar enthalpy for each species can similarly

be obtained to be

$$\begin{aligned}
h_k^{PR} = & \left(\frac{\sum_j X_j A_{jk} - T \sum_j X_j \frac{\partial A_{jk}}{\partial T}}{\sqrt{2}b_m} - \frac{(A_m - T \frac{\partial A_m}{\partial T}) b_k}{2\sqrt{2}b_m^2} \right) \ln \left(\frac{V + (1 - \sqrt{2})b_m}{V + (1 + \sqrt{2})b_m} \right) \\
& + pV_i - R_u T \\
& + \left(\frac{A_m - T \frac{\partial A_m}{\partial T}}{2\sqrt{2}b_m} \right) \left(\frac{2\sqrt{2}(b_m V_k - b_k V)}{(V + (1 + \sqrt{2})b_m)(V + (1 - \sqrt{2})b_m)} \right) + h_k^o
\end{aligned} \tag{B.13}$$

Appendix C

Assessment of Chung correlation for transport property estimation

As discussed in Section 2.4.2.1 - Chung correlation: for μ and λ , high-pressure transport property estimation routines must not only be sufficiently accurate in the dense-gas region, but also fallback to corresponding low-pressure values at high temperatures. In this section, we conduct two types of assessments for several property estimation methods over the low-temperature and high-temperature ranges. The low-temperature range for each species is chosen so that it covers the phase envelope or the region of liquid-gas transition or the region of significant non-ideality. The high-temperature region is the region of relatively low non-ideality. The accuracy in the low-temperature range is important for the reactant species and pre-flame region intermediates which are expected to be fairly non-ideal like O_2 and CH_4 , while the high-temperature range is for the species like CO_2 , H_2O , and H_2 , which are expected to follow only the temperature dependence for the transport properties. For the low-temperature interval, a supercritical pressure is used according to the species in question (Table C.1). For high-temperature ranges, a low-pressure of 1 *bar* is used.

To assess the accuracy, we tabulate the results as an Averaged Absolute

Species	Low-temp range	High-temp range	Pressure
H_2O	(274-1000)K	(1000-3500)K	$p = 250bar$
CH_4	(100-600)K	(600-3000)K	$p = 100bar$
O_2	(100-600)K	(600-3000)K	$p = 100bar$
CO_2	(266-800)K	(800-1100)K	$p = 250bar$
H_2	-	(130-1100)K	$p = 100bar$
$C_{12}H_{26}$	(266-700)K	(500-700)K	$p = 150bar$

Table C.1: Low- and high-temperature intervals for evaluated species

Deviations (AADs), defined as

$$AAD = \frac{1}{N} \sum_{i=1}^N \frac{abs(y_i - y_{i,ref})}{y_{i,ref}}. \quad (C.1)$$

The AADs are estimated with respect to the reference fluid properties available in Coolprop [1].

Firstly, we compare the low-pressure Chapman-Enskog theory correlations given by Eqn. 2.43 and Eqn. 2.52 with the reference values. The high-temperature region is of primary importance for the purposes of this correlation. Water shows the highest deviation from reference values in the high-temperature region, with AADs of $\sim 5\%$ and $\sim 9\%$ for viscosity and thermal conductivity respectively.

Secondly, we compare the original Chung correlation (Eqn. 2.59 and Eqn. 2.61) and the modified form of the Chung correlation (Eqn. 2.66) with the reference values at a supercritical isobar. The two methods perform approximately the same in both temperature intervals for some species, with the modified Chung correlation showing improved accuracy in some cases. The modified Chung correlation improves the high-temperature accuracy of H_2O viscosity, while degrading the accuracy in the case of thermal conductivity. However, the high-temperature values obtained using the modified correlation blend well with Chapman-Enskog values (Figure C.1 through Figure C.6), and is the basis of the adoption in the present study.

Species	Chapman-Enskog		Chung et al. (1988)		Modified Chung	
	Low	High	Low	High	Low	High
H_2O	-	0.045	0.078	0.179	0.076	0.020
CH_4	-	0.029	0.202	0.039	0.212	0.030
O_2	-	0.027	0.085	0.017	0.093	0.032
CO_2	-	0.007	0.056	0.031	0.069	0.048
H_2	-	0.026	-	0.168	-	0.079
$C_{12}H_{26}$	-	0.009	0.174	-	0.134	-

Table C.2: AADs in viscosities computed in the low- and high-temperature intervals with respect to reference properties from Coolprop [1].

Species	Chapman-Enskog		Chung et al. (1988)		Modified Chung	
	Low	High	Low	High	Low	High
H_2O	-	0.088	0.277	0.073	0.299	0.110
CH_4	-	0.020	0.090	0.055	0.060	0.021
O_2	-	0.009	0.055	0.029	0.061	0.005
CO_2	-	0.012	0.077	0.067	0.058	0.017
H_2	-	0.042	-	0.233	-	0.096
$C_{12}H_{26}$	-	0.020	0.159	-	0.186	-

Table C.3: AADs in thermal conductivities computed in the low- and high-temperature intervals with respect to reference properties from Coolprop [1].

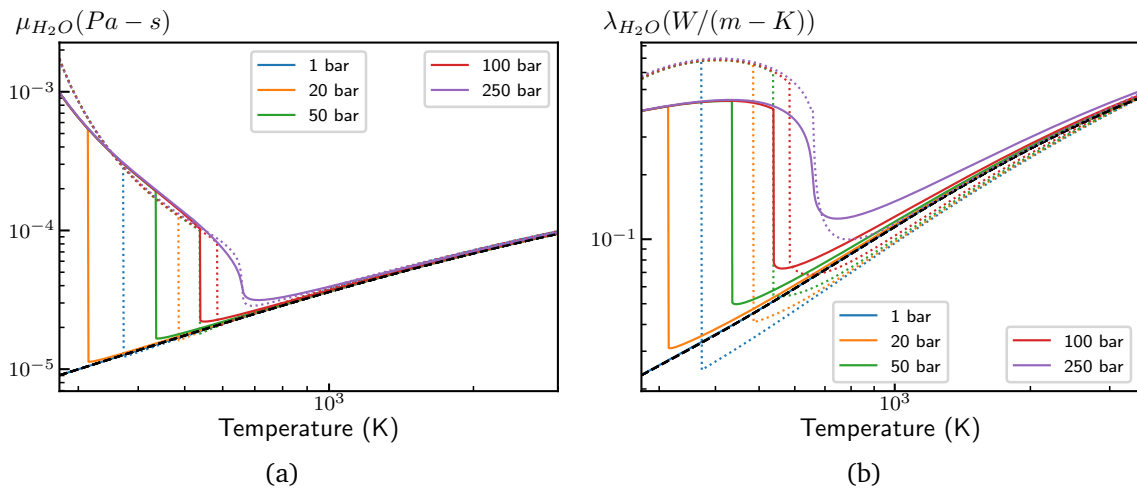


Figure C.1: Pure-fluid a) viscosities and b) thermal conductivities of Water using the low-pressure correlation (---), the original (-.-.-) and modified (—) Chung correlation and the reference values (.....).

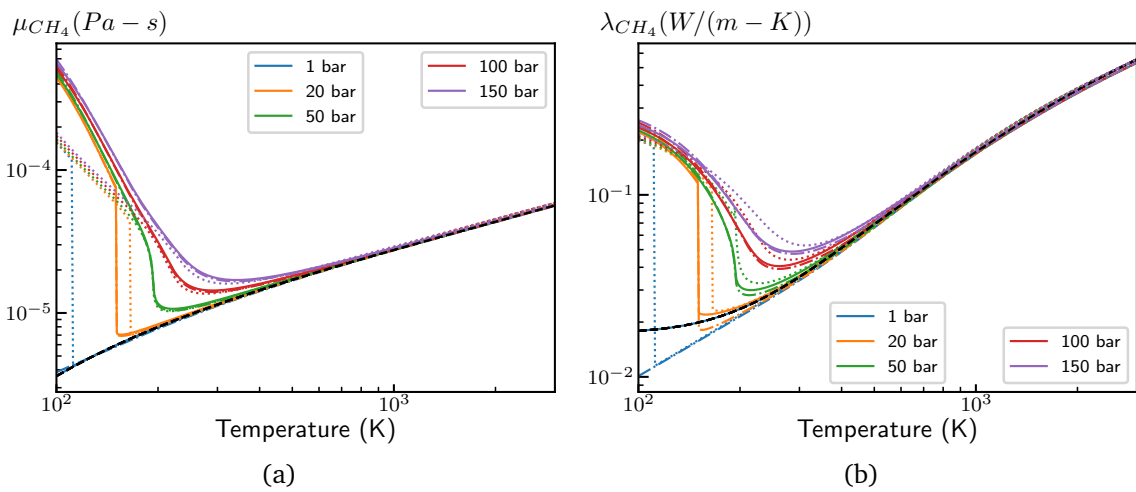


Figure C.2: Pure-fluid a) viscosities and b) thermal conductivities of Methane using the low-pressure correlation (---), the original (.....) and modified (—) Chung correlation and the reference values (.....).

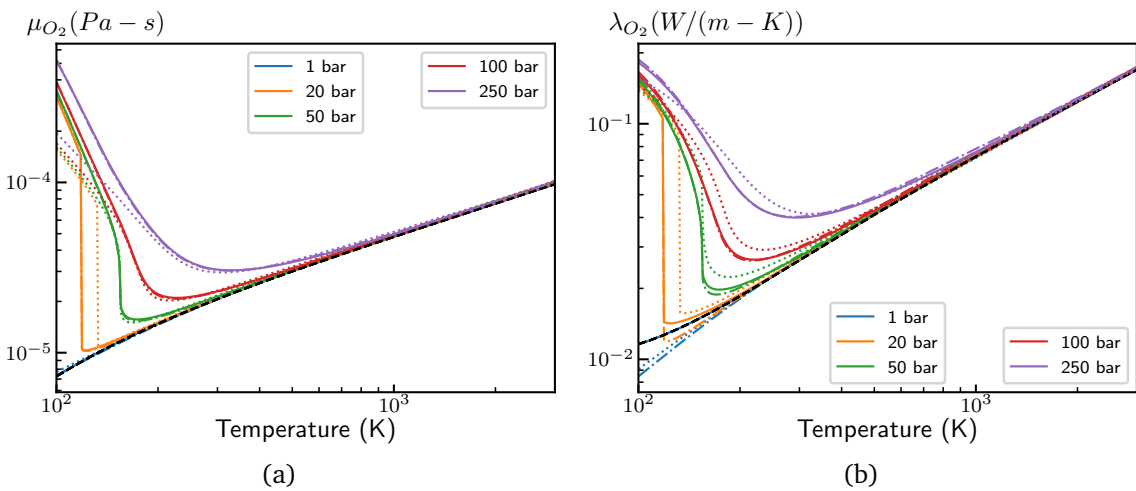


Figure C.3: Pure-fluid a) viscosities and b) thermal conductivities of Oxygen using the low-pressure correlation (---), the original (.....) and modified (—) Chung correlation and the reference values (.....).

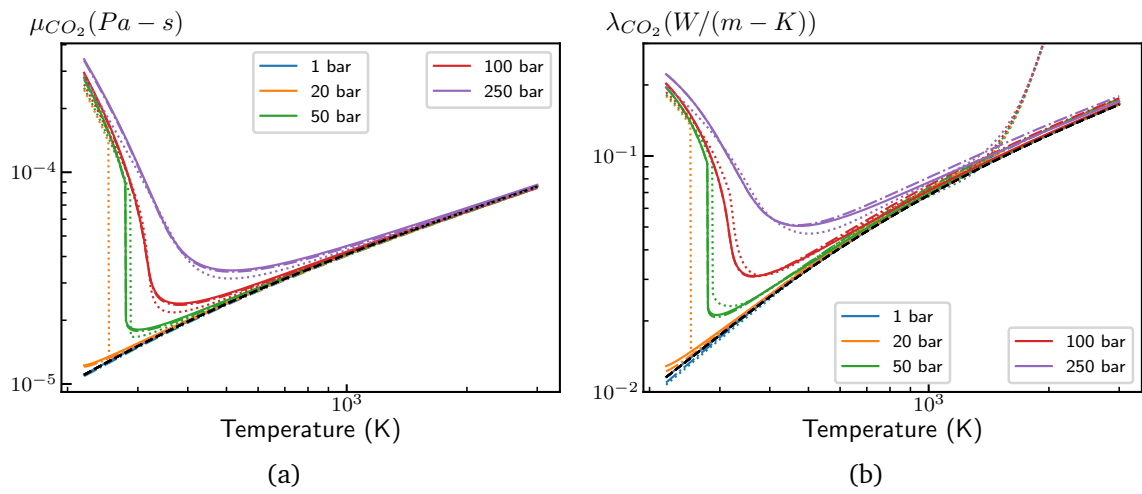


Figure C.4: Pure-fluid a) viscosities and b) thermal conductivities of CO_2 using the low-pressure correlation (---), the original (.....) and modified (—) Chung correlation and the reference values (.....).

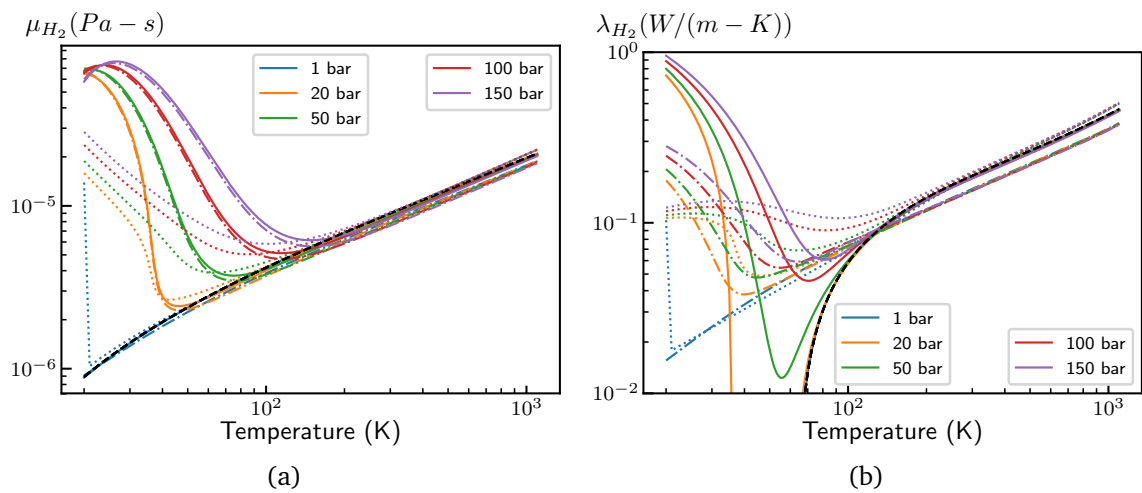


Figure C.5: Pure-fluid a) viscosities and b) thermal conductivities of Hydrogen using the low-pressure correlation (---), the original (.....) and modified (—) Chung correlation and the reference values (.....).

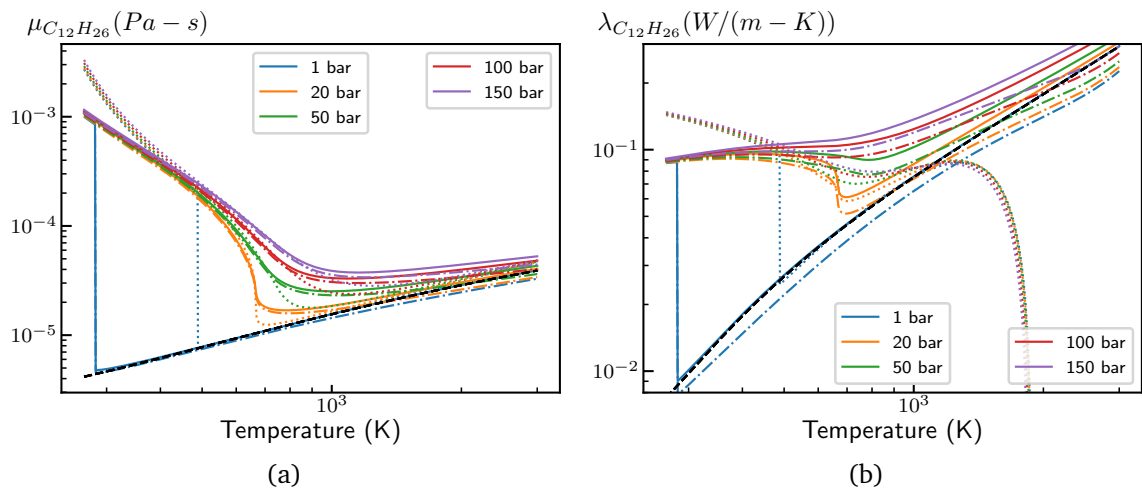


Figure C.6: Pure-fluid a) viscosities and b) thermal conductivities of n-Dodecane using the low-pressure correlation (---), the original (-.-.) and modified (—) Chung correlation and the reference values (.....).

References

- [1] I. H. Bell, J. Wronski, S. Quoilin, and V. Lemort. Pure and Pseudo-pure Fluid Thermophysical Property Evaluation and the Open-Source Thermophysical Property Library CoolProp. *Industrial & Engineering Chemistry Research*, 53(6):2498–2508, 2014. doi: 10.1021/ie4033999. URL <http://pubs.acs.org/doi/abs/10.1021/ie4033999>.
- [2] R. B. Bird, W. E. Stewart, and E. N. Lightfoot. *Transport phenomena*. John Wiley & Sons, 2007.
- [3] M. A. Bullock and D. H. Grinspoon. The recent evolution of climate on Venus. *Icarus*, 150(1):19–37, 2001.
- [4] M. P. Burke, M. Chaos, Y. Ju, F. L. Dryer, and S. J. Klippenstein. Comprehensive H₂/O₂ kinetic model for high-pressure combustion. *International Journal of Chemical Kinetics*, 44(7):444–474, 2012.
- [5] V. Cabral, R. Pinto, F. Tavares, and M. Castier. Phase equilibria of binary mixtures by molecular simulation and cubic equations of state. *Brazilian Journal of Chemical Engineering*, 18(2):149–161, 2001.
- [6] W. A. Cañas-Marín, U. E. Guerrero-Aconcha, and J. D. Ortiz-Arango. Comparison of different cubic equations of state and combination rules for predicting residual chemical potential of binary and ternary Lennard–Jones mixtures: Solid-supercritical fluid phase equilibria. *Fluid phase equilibria*, 234(1):42–50, 2005.
- [7] S. Candel, T. Schmitt, and N. Darabiha. Progress in transcritical combustion: experimentation, modeling and simulation. *23rd ICDERS, Irvine*, 2011.
- [8] T. H. Chung, M. Ajlan, L. L. Lee, and K. E. Starling. Generalized multiparameter correlation for nonpolar and polar fluid transport properties. *Industrial & engineering chemistry research*, 27(4):671–679, 1988.
- [9] D. E. Cristancho, I. D. Mantilla, L. A. Coy, A. Tibaduiza, D. O. Ortiz-Vega, K. R. Hall, and G. A. Iglesias-Silva. Accurate P- ρ - T Data and Phase Boundary Determination for a Synthetic Residual Natural Gas Mixture. *Journal of Chemical & Engineering Data*, 56(4):826–832, 2010.

- [10] M. El-Gamal, E. Gutheil, and J. Warnatz. The structure of laminar premixed H₂-Air flames at elevated pressures. *Zeitschrift für Physikalische Chemie*, 214 (4/2000):419, 2000.
- [11] V. Giovangigli, L. Matuszewski, and F. Dupoirieux. Detailed modeling of planar transcritical H₂-O₂-N₂ flames. *Combustion Theory and Modelling*, 15 (2):141–182, 2011.
- [12] I. Glassman, R. A. Yetter, and N. G. Glumac. *Combustion*. Academic press, 2014.
- [13] D. G. Goodwin. One-dimensional flames. In *30th Symposium on Combustion*, pages 1–40, 2004.
- [14] D. G. Goodwin, H. K. Moffat, and R. L. Speth. Cantera: An object-oriented software toolkit for chemical kinetics, thermodynamics, and transport processes, 2017. Version 2.3.0.
- [15] E. A. Guggenheim. The principle of corresponding states. *The Journal of Chemical Physics*, 13(7):253–261, 1945.
- [16] O. Gurliat, V. Schmidt, O. Haidn, and M. Oschwald. Ignition of cryogenic H₂/LOX sprays. *Aerospace Science and Technology*, 7(7):517–531, 2003.
- [17] U. Guven and G. Ribert. Impact of non-ideal transport modeling on supercritical flow simulation. *Proceedings of the Combustion Institute*, 2018.
- [18] V. I. Harismiadis, A. Z. Panagiotopoulos, and D. P. Tassios. Phase equilibria of binary Lennard-Jones mixtures with cubic equations of state. *Fluid Phase Equilibria*, 94:1–18, 1994.
- [19] K. G. Harstad, R. S. Miller, and J. Bellan. Efficient high-pressure state equations. *AIChE journal*, 43(6):1605–1610, 1997.
- [20] J. Hickey and M. Ihme. Supercritical mixing and combustion in rocket propulsion. *Annual Research Briefs*, pages 21–36, 2013.
- [21] J. Huang, P. Hill, W. Bushe, and S. Munshi. Shock-tube study of methane ignition under engine-relevant conditions: experiments and modeling. *Combustion and flame*, 136(1):25–42, 2004.
- [22] J. E. Jones. On the Determination of Molecular Fields. II. From the Equation of State of a Gas. *Proceedings of the Royal Society of London Series A*, 106 (738):463–477, 1924.
- [23] A. J. Juanós and W. A. Sirignano. Pressure effects on real-gas laminar counterflow. *Combustion and Flame*, 181:54–70, 2017.

- [24] W. Juchmann, H. Latzel, D. Shin, G. Peiter, T. Dreier, H.-R. Volpp, J. Wolfrum, R. Lindstedt, and K. Leung. Absolute radical concentration measurements and modeling of low-pressure CH₄/O₂/NO flames. In *Symposium (International) on Combustion*, volume 27, pages 469–476. Elsevier, 1998.
- [25] R. J. Kee, G. Dixon-Lewis, J. Warnatz, M. E. Coltrin, and J. A. Miller. A Fortran computer code package for the evaluation of gas-phase multicomponent transport properties.
- [26] R. J. Kee, F. M. Rupley, and J. A. Miller. Chemkin-II: A Fortran chemical kinetics package for the analysis of gas-phase chemical kinetics. Technical report, Sandia National Labs., Livermore, CA (USA), 1989.
- [27] R. J. Kee, M. E. Coltrin, and P. Glarborg. *Chemically reacting flow: theory and practice*. John Wiley & Sons, 2005.
- [28] G. Lacaze, B. Cuenot, T. Poinso, and M. Oschwald. Large eddy simulation of laser ignition and compressible reacting flow in a rocket-like configuration. *Combustion and Flame*, 156(6):1166–1180, 2009.
- [29] C. K. Law. *Combustion physics*. Cambridge university press, 2010.
- [30] T. W. Leland and P. S. Chappellear. The corresponding states principle - a review of current theory and practice. *Industrial & Engineering Chemistry*, 60(7):15–43, 1968.
- [31] A. Linan and F. A. Williams. *Fundamental aspects of combustion*. 1993.
- [32] P. Lindstedt. Modeling of the chemical complexities of flames. In *Symposium (International) on Combustion*, volume 27, pages 269–285. Elsevier, 1998.
- [33] Linstrom and W. Mallard. NIST Chemistry WebBook, NIST Standard Reference Database Number 69.
- [34] J. S. Lopez-Echeverry, S. Reif-Acherman, and E. Araujo-Lopez. Peng-robinson equation of state: 40 years through cubics. *Fluid Phase Equilibria*, 447:39 – 71, 2017.
- [35] A. L. Magalhães, F. A. Da Silva, and C. M. Silva. New models for tracer diffusion coefficients of hard sphere and real systems: Application to gases, liquids and supercritical fluids. *The Journal of Supercritical Fluids*, 55(3): 898–923, 2011.
- [36] A. L. Magalhães, F. A. Da Silva, and C. M. Silva. Tracer diffusion coefficients of polar systems. *Chemical engineering science*, 73:151–168, 2012.
- [37] E. Mallard and H. Le Chatelier. Thermal model for flame propagation. In *Annales des Mines*, volume 4, pages 379–568, 1883.

- [38] M. Marchionni, S. K. Aggarwal, I. K. Puri, and D. Lentini. The influence of real-gas thermodynamics on simulations of freely propagating flames in methane/oxygen/inert mixtures. *Combustion Science and Technology*, 179(9): 1777–1795, 2007.
- [39] M. M. Masquelet. *Large-eddy simulations of high-pressure shear coaxial flows relevant for H₂/O₂ rocket engines*. PhD thesis, Georgia Institute of Technology, 2013.
- [40] S. McAllister, J.-Y. Chen, and A. C. Fernandez-Pello. *Fundamentals of combustion processes*. Springer, 2011.
- [41] B. J. McBride, S. Gordon, and M. A. Reno. Coefficients for calculating thermodynamic and transport properties of individual species. 1993.
- [42] I. Medina. Determination of diffusion coefficients for supercritical fluids. *Journal of Chromatography A*, 1250:124–140, 2012.
- [43] V. Mikhelson. On the normal ignition rate of fulminating gas mixtures. *Ph. D. thesis, Moscow University, 1889 (in Russian)*, 1889.
- [44] M. J. Moran, H. N. Shapiro, D. D. Boettner, and M. B. Bailey. *Fundamentals of engineering thermodynamics*. John Wiley & Sons, 2010.
- [45] R. W. Nickalls. A new approach to solving the cubic: Cardan’s solution revealed. *The Mathematical Gazette*, 77(480):354–359, 1993.
- [46] J. C. Oefelein and V. Yang. Modeling high-pressure mixing and combustion processes in liquid rocket engines. *Journal of Propulsion and Power*, 14(5), 1998.
- [47] C. Pauly, J. Sender, and M. Oschwald. Ignition of a gaseous methane/oxygen coaxial jet. In *Progress in Propulsion Physics*, volume 1, pages 155–170. EDP Sciences, 2009.
- [48] E. L. Petersen, D. M. Kalitan, S. Simmons, G. Bourque, H. J. Curran, and J. M. Simmie. Methane/propane oxidation at high pressures: Experimental and detailed chemical kinetic modeling. *Proceedings of the combustion institute*, 31(1):447–454, 2007.
- [49] T. Poinso and D. Veynante. *Theoretical and numerical combustion*. RT Edwards, Inc., 2005.
- [50] T. J. Poinso and S. Lelef. Boundary conditions for direct simulations of compressible viscous flows. *Journal of computational physics*, 101(1):104–129, 1992.
- [51] B. E. Poling, J. M. Prausnitz, J. P. O’connell, et al. *The properties of gases and liquids*, volume 5. McGraw-Hill New York, 2001.

- [52] R. D. Reitz. Computations of laminar flame propagation using an explicit numerical method. In *Symposium (International) on Combustion*, volume 18, pages 433–442. Elsevier, 1981.
- [53] G. Ribert, X. Petit, and P. Domingo. High-pressure methane-oxygen flames. Analysis of sub-grid scale contributions in filtered equations of state. *The Journal of Supercritical Fluids*, 121:78–88, 2017.
- [54] G. Rozenchan, D. Zhu, C. Law, and S. Tse. Outward propagation, burning velocities, and chemical effects of methane flames up to 60 atm. *Proceedings of the Combustion Institute*, 29(2):1461–1470, 2002.
- [55] A. M. Saur. *Calculation of countercurrent diffusion flames up to pressures of 3000 bar*. PhD thesis, Karlsruhe Institute of Technology (KIT), 1992. Karlsruhe, Univ., Diss., 1992.
- [56] R. Schmidt and W. Wagner. A new form of the equation of state for pure substances and its application to oxygen. *Fluid Phase Equilibria*, 19(3):175–200, 1985.
- [57] V. Schmidt, J. Sender, and M. Oschwald. Simultaneous Observation of Liquid Phase Distribution and Flame Front Evolution during the Ignition Transient of a LOX/GH_2 -combustor. *Journal of visualization*, 4(4):365–372, 2001.
- [58] N. N. Semenov. *Thermal Theory of Combustion and Explosion*. 3; Theory of Normal Flame Propagation. 1942.
- [59] U. Setzmann and W. Wagner. A new equation of state and tables of thermodynamic properties for methane covering the range from the melting line to 625 K at pressures up to 100 MPa. *Journal of Physical and Chemical reference data*, 20(6):1061–1155, 1991.
- [60] G. P. Smith, D. M. Golden, M. Frenklach, N. W. Moriarty, B. Eiteneer, M. Goldenberg, C. T. Bowman, R. K. Hanson, S. Song, W. C. Gardiner Jr, et al. GRI 3.0 Mechanism. *Gas Research Institute* (http://www.me.berkeley.edu/gri_mech), 1999.
- [61] J. J. Smith. *High Pressure LOx/H2 rocket engine combustion*. University of Adelaide, School of Mechanical Engineering, 2007.
- [62] M. D. Smooke. Solution of burner-stabilized premixed laminar flames by boundary value methods. *Journal of Computational Physics*, 48(1):72–105, 1982.
- [63] G. Soave. Equilibrium constants from a modified Redlich-Kwong equation of state. *Chemical engineering science*, 27(6):1197–1203, 1972.
- [64] R. Span. Using multiparameter equations of state for pure substances. In *Multiparameter Equations of State*, pages 15–60. Springer, 2000.

- [65] R. Span and W. Wagner. A new Equation of State for Carbon Dioxide covering the fluid region from the Triple Point temperature to 1100 K at pressures up to 800 MPa. *Journal of Physical and Chemical Reference Data*, 25(6):1509–1596, 1996.
- [66] R. B. Stewart, R. T. Jacobsen, and W. Wagner. Thermodynamic properties of Oxygen from the Triple Point to 300 K with pressures to 80 MPa. *Journal of Physical and Chemical Reference Data*, 20(5):917–1021, 1991.
- [67] G.-J. Su. Modified Law of Corresponding States for real gases. *Industrial & Engineering Chemistry*, 38(8):803–806, 1946.
- [68] G. P. Sutton and O. Biblarz. *Rocket propulsion elements*. John Wiley & Sons, 2016.
- [69] S. Takahashi. Preparation of a generalized chart for the diffusion coefficients of gases at high pressures. *Journal of Chemical Engineering of Japan*, 7(6):417–420, 1975.
- [70] J. Trusler. The virial equation of state. In *Experimental Thermodynamics*, volume 5, pages 35–74. Elsevier, 2000.
- [71] J. O. Valderrama. The state of the cubic equations of state. *Industrial & engineering chemistry research*, 42(8):1603–1618, 2003.
- [72] J. Warnatz. Influence of transport models and boundary conditions on flame structure. In *Numerical methods in laminar flame propagation*, pages 87–111. Springer, 1982.
- [73] J. Warnatz, U. Maas, and R. W. Dibble. *Combustion*, volume 26. Springer, 1999.
- [74] F. A. Williams. *Combustion theory*. CRC Press, 2018.
- [75] G. Wilson. Vapor-liquid equilibria, correlation by means of a modified Redlich-Kwong equation of state. In *Advances in Cryogenic Engineering*, pages 168–176. Springer, 1964.
- [76] D. S. H. Wong and S. I. Sandler. A theoretically correct mixing rule for cubic equations of state. *AIChE Journal*, 38(5):671–680, 1992.
- [77] Y. B. Zeldovich and D. Frank-Kamenetskii. The theory of thermal propagation of flames. *Zh. Fiz. Khim*, 12:100–105, 1938.